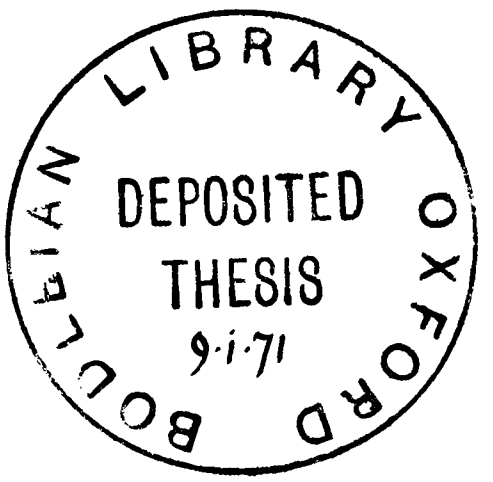
RADIOMETRIC MEASUREMENTS OF ATMOSPHERIC TEMPERATURE

by

F. W. Taylor

Jesus College



A Thesis submitted for the degree of Doctor of Philosophy in the University of Oxford

Clarendon Laboratory

October 1970



FRONTISPIECE. LARKHILL, WILTS.. 4 A.M. ON 7th AUGUST 1970.

Che fai tu, luma in ciel?

dimmi, che fai, silenziosa luna?

G. Leopardi.

ABSTRACT

A review of current problems and phenomena requiring further study in Atmospheric Physics is given, with particular reference to the upper atmosphere, defined as the region above 25 km. The conclusion is that an extended program of observations with very wide coverage and high accuracy is required, and that only satellite-borne instruments can do this economically. The particular difficulties associated with making accurate measurements at high levels are discussed, and the possibility of employing a number of conventional spectroscopic techniques is considered and finally rejected. The method of using a cell of carbon dioxide, the pressure of which is periodically modulated, as the spectroscopic element, as suggested by J. T. Houghton and C. D. Rodgers in 1965, is evaluated theoretically and shown to be capable of a temperature discrimination of 1°K with adequate height resolution at altitudes up to 70 km.

The rest of the thesis is concerned mainly with the design of suitable instrumentation. Three different prototypes using different pressure-modulation techniques and different optical systems were tried until a sufficiently sensitive and reliable design was achieved, suitable for a satellite instrument. This consists of an optical system using a germanium window and one germanium field lens together with a conical light-pipe and a wide band interference filter to isolate the band; an experimental pyroelectric detector developed by Mullard Ltd. is used. Pressure modulation is achieved by the use of a light alloy piston mounted on beryllium-copper spider springs and magnetically driven by cross-connected Helmholtz coils. Special electronics are used to maintain a constant amplitude of the piston. Modulating the pressure of the absorbing gas also modifies its absorption coefficient, chopping the centres of spectral lines in the selected band, and generating an a.c. signal at the detector. The intensity of this signal is related to the temperature of the emitting gas. The distribution of the emitting gas along the line of sight can be computed by the use of spectral

models and data on the band, but it was also measured directly by an experiment based on the Curtis-Godson approximation and using a simulated atmosphere in a large tank. The final design was incorporated into a flight prototype designed to be carried to 40 km. by a large balloon. The balloon radiometer had an in-flight calibration system together with voltage, current and temperature 'housekeeping' measurements all multiplexed for use with single channel eight-bit digital telemetry. The final two chapters deal with the flights of the balloon instruments, and the reduction of the data and its comparison with simultaneous measurements made by conventional radio-sonde. The results confirm the predictions of the theory, and it is concluded that a powerful new technique is available for the study of the Upper Stratosphere and Mesosphere.

Acknowledgements

I would like to express my grateful thanks to my supervisor, Dr. J. T. Houghton, for suggesting the topic for study, and for his sound guidance during the period of the research. I am greatly indebted to Dr. E. J. Williamson for his help, especially with the telemetry system; to Dr. G. D. Peskett for his advice and criticism, and for the design of parts of the electronics; to Dr. C. D. Rodgers, for useful discussion on matters of theory and computing; to Dr. D. R. Pick for assistance with environmental testing and ballooning; and to Mr. G. B. Marshall, whose painstaking skill in the workshop was a major factor in determining the success of the project.

Mr. E. Harris of Met. O.16 at the Meteorological Office provided much help with the numerous and complex administrative aspects of large balloon flying, and I am grateful to him and to Messrs. S. Reavell and R. Burgess of AWRE Aldermaston, Mr. K. Sillet of the Meteorological Research Unit at RAF Cardington, Mr. R. Fretwell of RAF Cardington and Mr. P. Lumley and the staff at Larkhill, all of whom helped in the business of launching the various balloons.

My thanks are also due to Professor Bleaney for the use of the Clarendon Laboratory, and to the various members of the staff of the Laboratory who helped in so many ways, especially the photographic department. My personal maintenance was provided by an Open Post-Graduate Scholarship awarded by the British Aircraft Corporation.

Finally, I would like to thank my wife, Doris, for drawing the diagrams and just generally being wonderful during the difficult times.

F.W.T.

Index

	Page
Chapter 1. Introduction.	1
1.1. Introductory Remarks and Plan of Thesis.	1
1.2. Atmosphere Structure.	3
1.3. Techniques for the Study of the Atmosphere.	6
Chapter 2. The Stratosphere and Mesosphere.	
2.1. Circulation	8
2.2. Stratosphere-Mesosphere Interactions.	9
2.3. Spring and Autumn Reversals.	10
2.4. Ozone Heating.	10
2.5. Temperature Structure.	11
2.6. Sudden and Explosing Warmings	12
2.7. The Ionosphere.	12
2.8. Gravity Waves.	13
2.9. Noctilucent Clouds.	13
2.10. Heat Budget.	14
2.11. Conclusions.	15
Chapter 3. Experimental Techniques for Upper-Atmosphere Temperature Soundings.	15
3.1. Basic Principles.	15
3.2. Theory	16
3.3. Instrumentation.	18
3.4. Choice of Band.	21
Chapter 4. Theoretical Study.	23
4.1. Weighting Functions.	
4.2. Energy Considerations.	26
4.3. Discussion of Assumptions.	27
4.4. Performance of a Real Instrument.	29
Chapter 5. The 4.3μ band Radiometer.	29
5.1. Design.	30.
5.2. Results.	31
5.3. Further Developments.	32
Chapter 6. The Radiative Relaxation Problem.	33

	Page
Chapter 7. The 15μ band Radiometer.	36
7.1. Design of the Pressure Modulator.	36
7.2. Optical Design.	39
7.3. Detector and electronics.	40
7.4. Results	41
7.4.1. Sensitivity	41
7.4.2. The transmission of the light pipe	41
7.4.3. Measurement of Δp_c	43
7.5. Conclusion.	44
Chapter 8. The Balloon Radiometer.	44
8.1. Introduction.	44
8.2. General Layout.	45
8.3. Radiometer Systems.	46
8.3.1. Design of the Pressure Modulator.	46
8.3.2. Chopping Frequency.	48
8.3.3. Cell Emission.	48
8.3.4. Optical Design.	49
8.3.5. Epoxy Resin.	50
8.4. In-Flight Calibration.	51
8.5. Electronics.	52
8.5.1. Piston Drive electronics.	52
8.5.2. Signal Electronics	54
8.5.3. Power Supplies.	55
8.5.4. Multiplexing.	56
8.5.5. Thermistor Bridge.	56
8.6. Telemetry.	57
8.7. Environmental Tests.	58
Chapter 9. The Pyroelectric Detector.	60
Chapter 10. Experimental Weighting Functions.	61
10.1. Method.	61
10.2. Results.	63
10.3. Effect of temperature structure.	63
Chapter 11. Balloon Ascents.	65
11.1. Introduction.	65
11.2. Flight of 7.8.70.	66
11.3. Reduction of Flight Data.	68
Chapter 12. Conclusion.	71
12.1. Further work.	72

Chapter 1. Introduction.

1.1. Introductory remarks and plan of thesis.

Atmospheric Physics divides into two fairly distinct sections: the experimental, and the theoretical. The experimentalist is concerned with exploration and the measurement of parameters within the atmosphere, and the design of instruments and development of techniques as ways to that end. The theoretician depends on him for data, and uses it to derive, and to expand and improve, theories and models which must eventually form a coherent picture of the atmosphere. From such an informed picture we will be able to understand, and even predict, the behaviour of the system and its many facets, and appreciate phenomena which at the present time we can only glimpse. Many obstacles lie in the road leading to this ideal. For the experimentalist, there is firstly the sheer scope of his task - bearing in mind that extensive and frequent measurements are required, for the atmosphere is a dynamic and co-ordinated system - and secondly, the difficulties of obtaining access to the remoter regions. For the theoretician, the main trouble is that good theories and models cannot be formed when only scanty data is available, as at present. Added to this is the potential difficulty of handling the amount of data which he needs, when this does become available, for the amount of information which represents any important atmospheric system is enormous, and must be constantly renewed as the system evolves. The answers to these problems, it has become clear, lie in the use of the most modern techniques - orbiting instruments on satellites to gather the data, rapid, efficient and economical telemetry links to relay it, and large computers to store and process it.

The part of Atmospheric Physics which deals with the collection of useful data from an orbiting satellite is a relatively new and certainly an important one; the subject of this thesis falls under this heading. In particular, it describes the laboratory and field work associated with the development of a new kind of instrument, from its conception in 1966 as an idea by J. T. Houghton and C. D. Rodgers to a balloon-borne

satellite prototype flown in 1970. The satellite instrument itself is expected to follow in 1973, on the experimental weather satellite Nimbus F. The device itself has been called the pressure-modulated selective chopper radiometer (PMSCR); its purpose is to measure temperature remotely at selected levels in the atmosphere from a satellite in polar orbit perhaps 1000 km. higher. It also has potential as a rocketsonde instrument, to replace thermistors and the like, or grenades, but this application is not pursued in depth here. The device is in some ways descended from the selective chopper radiometer (SCR) which has operated succesafully on board Nimbus 4, although the construction and theory behind the two kinds of instrument have little in common. It is, moreover, more advanced in that the PMSCR has the capacity for making measurements high in the atmospheric mesosphere, up to 70 km. or more, whereas the SCR and other existing instruments are limited to the denser regions below 45 km. It is this unique feature which makes the PMSCR of interest, since it may offer the first opportunity for the large-scale exploration of the temperature structure of the upper atmosphere in the 45-70 km. region, a part of the atmosphere about which just enough is known to make it of absorbing interest, in spite of the low densities which prevail. Chapter 2 is intended to justify this assertion, by brief discussions of some of the most interesting features of the region, and those about which we would like to learn more. Chapter 3 is a review of experimental techniques for temperature sounding; here the particular advantages of the PMSCR over any other approach are discussed. Then the principles of the new device are described, and some preliminary calculations of the expected performance set out. Chapter 5 describes the design and performance of a bench prototype radiometer. On the basis of this and in the light of newly published results (Chapter 6) an improved prototype is derived (Chapter 7) and in its final form is prepared as a package to be flown on a high-altitude balloon. The flight model radiometer and associated systems are described in Chapter 8, while Chapter 10 describes the laboratory calibrations. Chapter 11 deals with the actual flights, with the reduction of the data and an evaluation of the results obtained.

1.2. Atmospheric Structure.

The Earth's atmosphere is a vast and massive thermodynamic system of great complexity, consisting of more than fifty thousand billion tons of mixed gases, thinly spread on a rotating spheroid and unevenly heated by incoming radiation. The radiation within the atmosphere, while basically due to the superposition of the incoming flux from the sun on the outgoing flux from the surface, is modified extensively by the atmospheric constituents which absorb, scatter and re-emit radiation at a variety of wavelengths, each gas having different properties in this respect, and trace constituents playing an important part. The situation is further complicated by the presence of water vapour, which forms into opaque or semi-opaque clouds of highly irregular shape and distribution which greatly influence the radiation field and hence the behaviour of the whole system. There are other factors such as chemical reactions within the atmosphere and the influence of the surface geography to be taken into account.

In the lower atmosphere, the principal direct source of energy is the ground, and not the sun. Almost 35% of the solar energy invident on the earth is reflected by clouds and gases, while 15% is absorbed in the atmosphere and 50% reaches the ground. The latter is mostly in the visible region, while the fraction absorbed is in the near infra-red, where the vibration-rotation bands of ozone, water vapour and carbon dioxide lie.

The average solar flux at the mean distance of the earth from the sun is 1.36×10^6 ergs $cm^{-2}sec^{-1}$, so that the average solar flux directly reaching the ground is

$$0.5 \times \frac{1}{4} \times 1.36 \times 10^6 = 1.7 \times 10^5 \text{ erg } cm^{-2}sec^{-1},$$

where $\frac{1}{4}$ is the ratio of the area presented to the sun to the actual surface area. This flux is absorbed by the ground and heats it to a temperature in the neighbourhood of $235^{\circ}K$. The ground then radiates as a black body at this temperature, with a Planck spectrum having a peak in the far infra-red, at a wavelength of 15×10^{-6} cm. or 15 microns (μ), fig. 1.1.

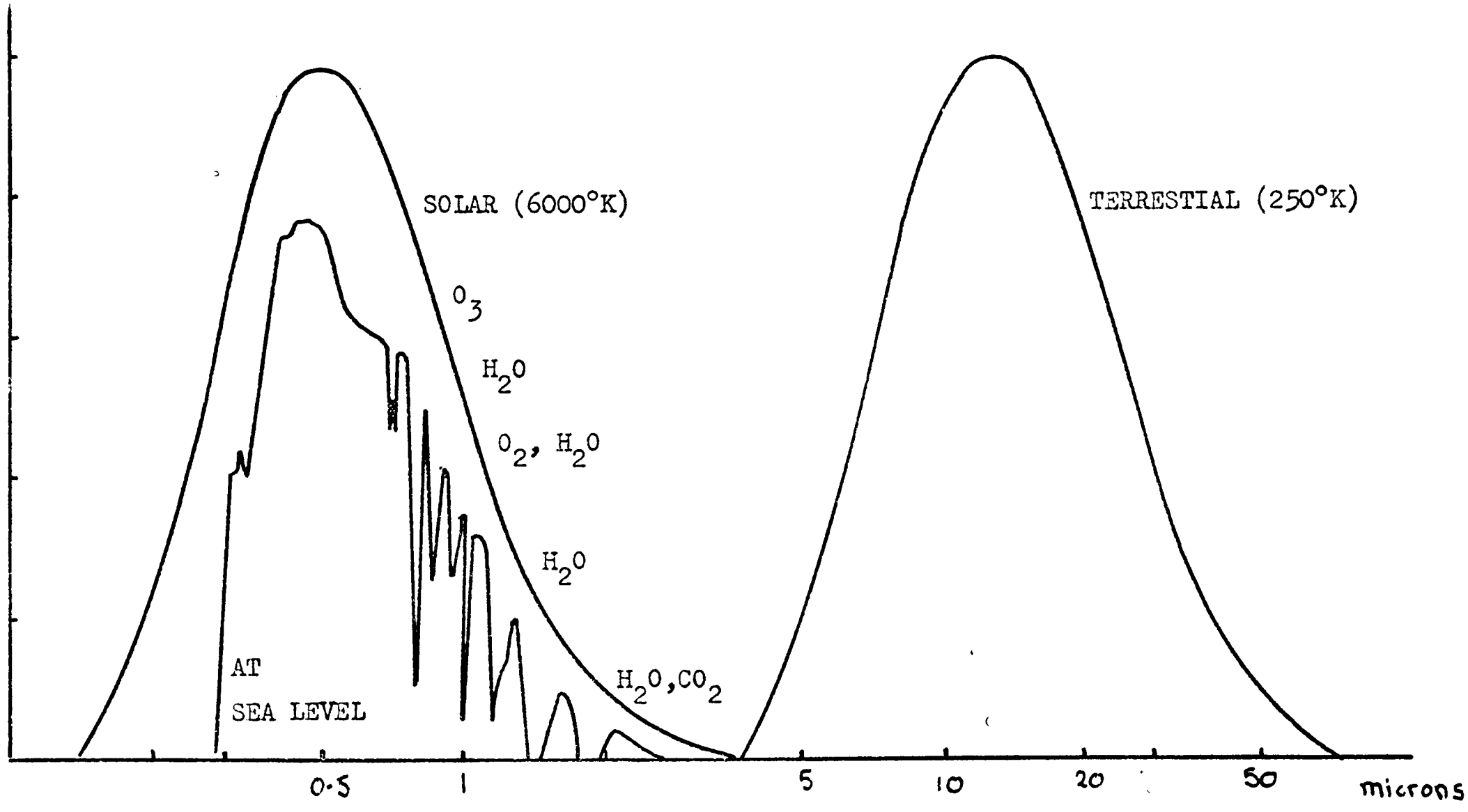


Fig.1.1. Solar and Terrestial Black Body Curves, and Solar Irradiation at Sea Level.

(After Kondratiev,1969).

Radiation in this region of the spectrum is strongly absorbed by several atmospheric components, in particular ozone, water vapour, and carbon dioxide, so emission from the ground heats the atmosphere which re-rates the absorbed energy. Part of this escapes to space, part is absorbed again elsewhere in the atmosphere and part travels downwards to provide additional heating of the surface. This so-called greenhouse effect raises the temperature of the surface by a further 55°K, so that the ground enjoys a mean temperature of about 290°K.

Local variations in the process of absorption and radiation transfer over various land and sea masses provide the temperature and pressure differences which constitute the sources of weather activity. These are superimposed on broad circulation patterns produced by the combined effects of differential heating due to the shape of the earth, and Coriolis forces due to its rotation. Friction between the atmosphere and the surface also plays an important part, and the net effect is the familiar system of trade winds, prevailing westerlies and polar easterlies which exists in each hemisphere.

Although long-wave radiation in the infra-red plays a dominant role in the lower atmosphere, there is little or no interaction with these wavelengths at great heights because the constituents at these levels (above about 120 km.) are simple atomic or diatomic particles without spectra in the infra-red region. There the principal role is played by the short-wave components of the solar spectrum - the near and far ultraviolet, and occasionally the X-ray region. Less than 1% of the total solar energy flux is in these regions, but it is the principal source of heating of the thin upper air and the major determining factor in its structure. The absorption cross-sections of O_2, O, N_2 and N in the far ultraviolet are so large that all of the incident flux in this part of the spectrum is effectively removed before it penetrates to a height of 100 km., in spite of the very thin air at those altitudes. The density at 100 km. is only 10^{-7} of the surface value.

Temperature, density and composition are the basic atmospheric data. Of these, temperature is in some ways the most important because it

directly reflects the processes of energy absorption which determine the structure of the atmosphere. The temperature of the atmosphere as a function of height is shown schematically in fig.1.2. This figure shows how the atmosphere may be conveniently divided into regions according to the temperature structure, and the different names given to the regions are shown.

In the troposphere the temperature falls steadily with increasing distance from the source of heat, at a rate of about 6.5°K per km. At the tropopause the decrease is halted and the temperature rises again to a maximum of about 300°K at 50 km. This rise is due to the heating produced by the absorption of solar u.v. in the ozone layer, the band of absorbed wavelengths extending from 2000 Å to 3000 Å. The ozone concentration is a maximum at about 25 km., and above 50 km. the temperature begins to fall again, reaching a minimum of about 200°K at 90 km. This minimum is associated with an energy sink due to the absorption and re-emission in the ν_3 band of CO_2, and a fine structure transition $O(^3P_1) \rightleftharpoons O(^3P_0)$ in the ground state of atomic oxygen. Above 90 km. the temperature rises, reaching a roughly isothermal level of around 1200°K above 300 km. This increase results from heating produced by the photo-dissociation and photo-ionization of oxygen and nitrogen by solar ultraviolet radiation in the wavelength region 2000 Å down to 100 Å.

In the lower atmosphere the transport of energy by radiation alone requires temperature gradients so steep as to be unstable, and the energy transfer is augmented by convective transport, which leads to a thorough mixing of all atmospheric constituents. The atmosphere is stable against vertical convection above 10 km., but is turbulent and therefore mixed up to about 120 km. The reasons for this are not very clear as yet. Above 120 km. the gases settle into layers determined by their separate molecular weights, being mainly atomic oxygen to 1000 km., helium to 2500 km., and hydrogen thereafter.

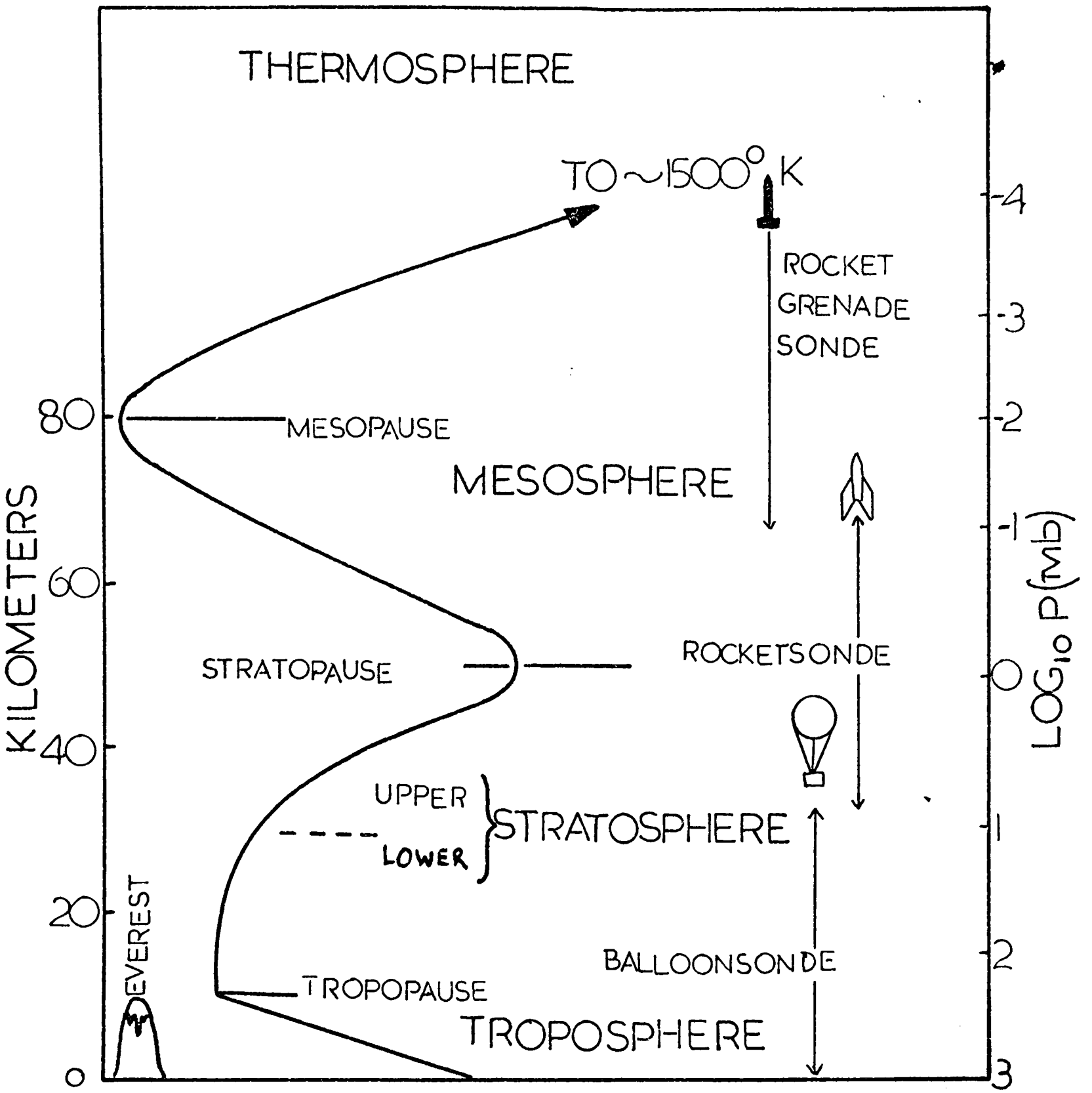


FIG. 1.2 ATMOSPHERIC TEMPERATURE STRUCTURE

1.3. Techniques for the study of the atmosphere.

Temperature, density and composition are the most basic atmospheric parameters. Other essential data are those on the incident solar flux and the topography of the earth. In theory a complete knowledge of these together with a perfect understanding of the physical and chemical properties of the atoms and molecules involved constitutes a complete picture of the atmosphere from which all observed phenomena may be derived. In practice we wish also to make observations of related quantities such as pressure, and wind direction and speed. Ideally measurements are required closely spaced over a whole hemisphere, in the vertical direction as well as horizontally, and at regular short intervals in time. From such data the evolution and eventual fate of systems and phenomena may be followed. It is abundantly clear from observations made to date that the atmosphere shows large scale patterns, that temperature and pressure anomalies travel very large distances horizontally during their lifetimes, and that smaller but important vertical interactions occur. Isolated or infrequent measurements are therefore of strictly limited usefulness, since they only reveal the gross properties of the atmosphere.

Meteorological balloon flights have been made for the last 150 years. The balloon is a cheap, reliable and versatile platform, requiring minimal ground facilities and imposing few strict restraints on the instrumentation carried. Relatively heavy loads are feasible. Most of our present knowledge of the troposphere and the lower stratosphere results from the many thousands of balloon flights which have been made, and which continue to be made routinely. The balloon has only limited access to the upper atmosphere, however. The latest types can ascend to over 40 km., but these have to be very big.

Our knowledge of the upper stratosphere and mesosphere results mainly from sounding rocket flights, which started shortly after the second war using captured German V-2s. Modern rockets can carry a wide range of payloads to great heights, but all suffer from the serious

disadvantage that they spend only a few minutes at most in the region of interest before plummeting rapidly downwards, since parachutes are virtually ineffective above about 60 km. The two main techniques used for the measurement of temperature profiles are the rocket sonde, in which the sensitive element is a bead thermistor or fine wire, and the grenade method, which relies on the temperature dependence of the velocity of sound. Measurements by the former require correction for the effects of radiation, electrical and compressional heating, and conduction through the leads, and offer an accuracy of only $\pm$ 9°K at 65 km. (Wagner, 1964). The grenade technique is tedious, but the measurements are good to within $\pm$ 3°K at 75 km. (Stroud, 1960).

Both balloons and rockets suffer from the drawback that only a single profile of atmospheric parameters is obtained from each shot. To obtain adequate detail, and impracticably large number of launchings would be required, even if there were launching sites everywhere.

The only economically practical way of collecting data on a sufficiently large scale is by the use of artificial satellites. These must eventually replace balloons and rockets as our main platform for the routine observation of the atmosphere. The present network of weather stations, even with rapid communications, highly developed instruments and world-wide organisation through the WMO, still leaves vast areas of the globe without routine weather observations. Even in areas with dense observational networks like the United States and Europe, the average distance between surface stations is more than 90 miles, and between upper air observing stations it is more than 200 miles. These distances are too large to give a good picture of the detailed structure of interesting atmospheric phenomena, and the grouping of stations does not permit the study of the evolution of a system which may travel half way around the globe in its lifetime. Also, only a fragmented picture of the gross circulation on a global scale is obtained. The upper atmosphere suffers most heavily in all these respects.

Routine measurements of temperature, pressure and humidity will continue to be made by conventional sondes until such time as satellite measurements can offer the same accuracy and spacial resolution. Balloon and rocket payloads measure these properties at the point actually occupied by the instrument, whilst a satellite-borne device has to make a measurement of say temperature from a distance of perhaps 1000 km. This is a much more difficult task. Furthermore, instruments which observe any but the loftiest regions from satellites must also view other levels simultaneously. Since it is usually desirable to look more or less vertically down from orbit (to avoid excessive foreshortening of the field of view), often every level in the atmosphere is contributing to the radiation received at the satellite. Obtaining adequate vertical resolution is therefore a major problem.

Observations of the atmosphere have been made from satellites for the last ten years, and these are immensely important and interesting because of the timely global coverage obtained. There is, however, scope for improved instrumentation to increase the accuracy and versatility of the measurements; temperature sounding in particular is only possible below about 45 km. at present. Since this is also the ceiling for balloons, the regions above remain poorly explored although the little that is known suggests that they have many interesting and important features. Some of these are dealt with in the next chapter.

Chapter 2. The Stratosphere and the Mesosphere.

This chapter deals with the most interesting features of the region from 30 to 80 km., particularly those which could be studied using data from a satellite radiometer making temperature soundings at these levels.

2.1. Circulation

The atmosphere may be considered as having two principal circulation systems, the tropospheric and the stratospheric (which actually includes most of the mesosphere too) separated at about 24 km. by a relatively stagnant surface called the stratonull. The lower system is

characterized by a strong meridional component in addition to the zonal flow associated with the uneven solar heating, but the stratospheric system consists principally of zonal winds except in the highest parts of the mesosphere where a striking increase in the meridional wind components occurs (fig. 2.1).

The stratospheric circulation is driven principally by the horizontal temperature gradients produced as a result of the absorption of solar u.v. by ozone. Heating produced in this manner is naturally greatest at the sub-solar point than at higher incidence angles, where the solar energy is absorbed by a larger volume, especially since the ozone distribution would be expected to be higher where the flux density is largest. It is also reasonable to expect that the level of maximum heat input will be higher, as well as less intense, at the sunrise and sunset lines than at the normal incidence point. Such data as is available supports this general result. It also, however, indicates complicated departures from such simple predictions. There are, for example, curious phase lags in the diurnal distributions of wind speeds at different altitudes (fig. 2.2) and there is the dramatic change in wind speed and direction in the upper mesosphere. The reason for this seemingly excessive circulation activity is probably connected with frictional effects which remove energy from the long wavelengths of the general circulation and convert it into heat, but these effects await detailed study.

2.2. Stratosphere-Mesosphere interactions.

It is interesting to consider the nature of the exchange, if any, which takes place in a vertical direction to connect the relatively well understood lower atmosphere with the more obscure upper regions. Shapley (1966) reports a definite correlation between the ionospheric absorption index and the temperature at the 30 km. level (fig. 2.3). There is also some evidence that large temperature deviations at as low as 30 km. carry upwards into higher levels so that the pressure levels at mesospheric heights are markedly changed in the space of a few days.

Experiments with radioactive tracers have been described by

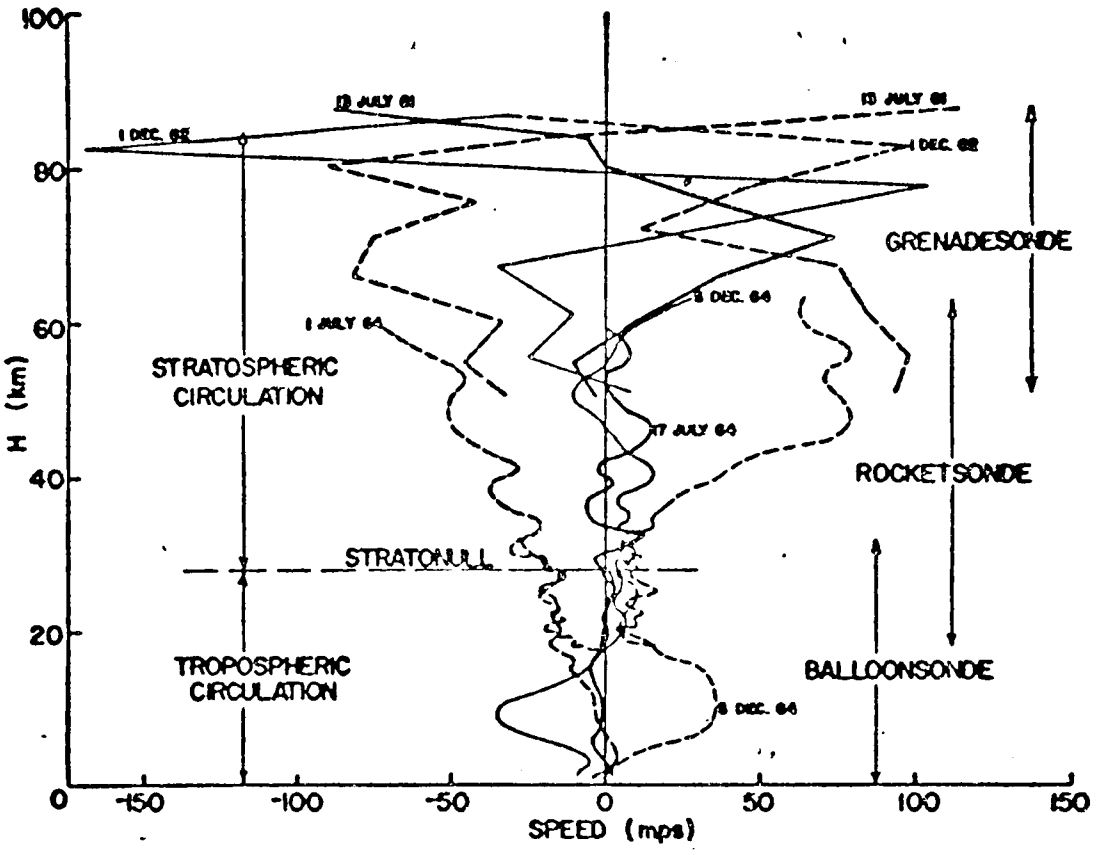


Fig. 2.1. Some soundings of wind speed as a function of height for the meridional (solid) and zonal (dashed) components, with south and west positive (Webb,1966).

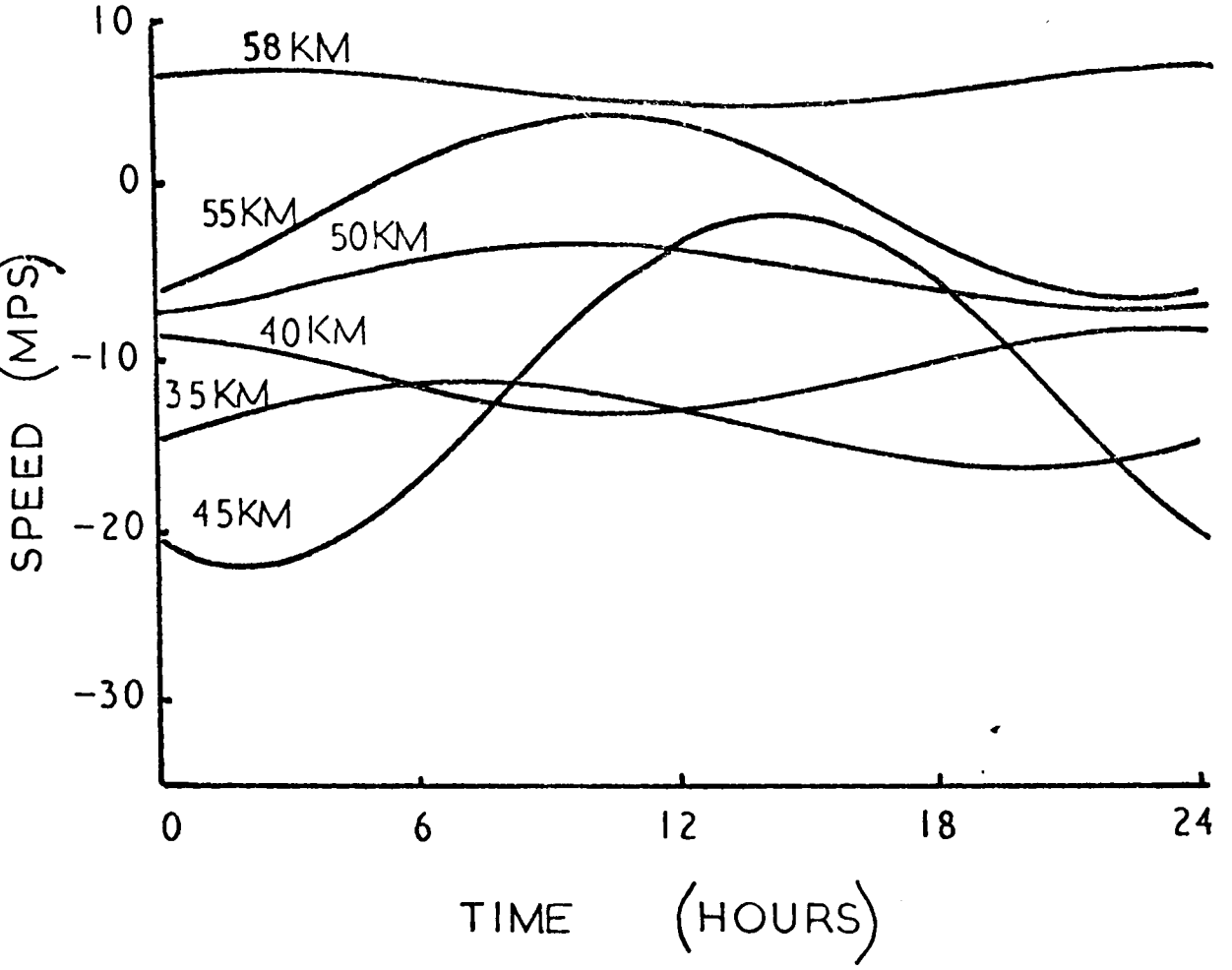


Fig.2.2. The diurnal variation of meridional wind speeds over White Sands, N.M., on 7-9 February 1964 (Webb 1966a).

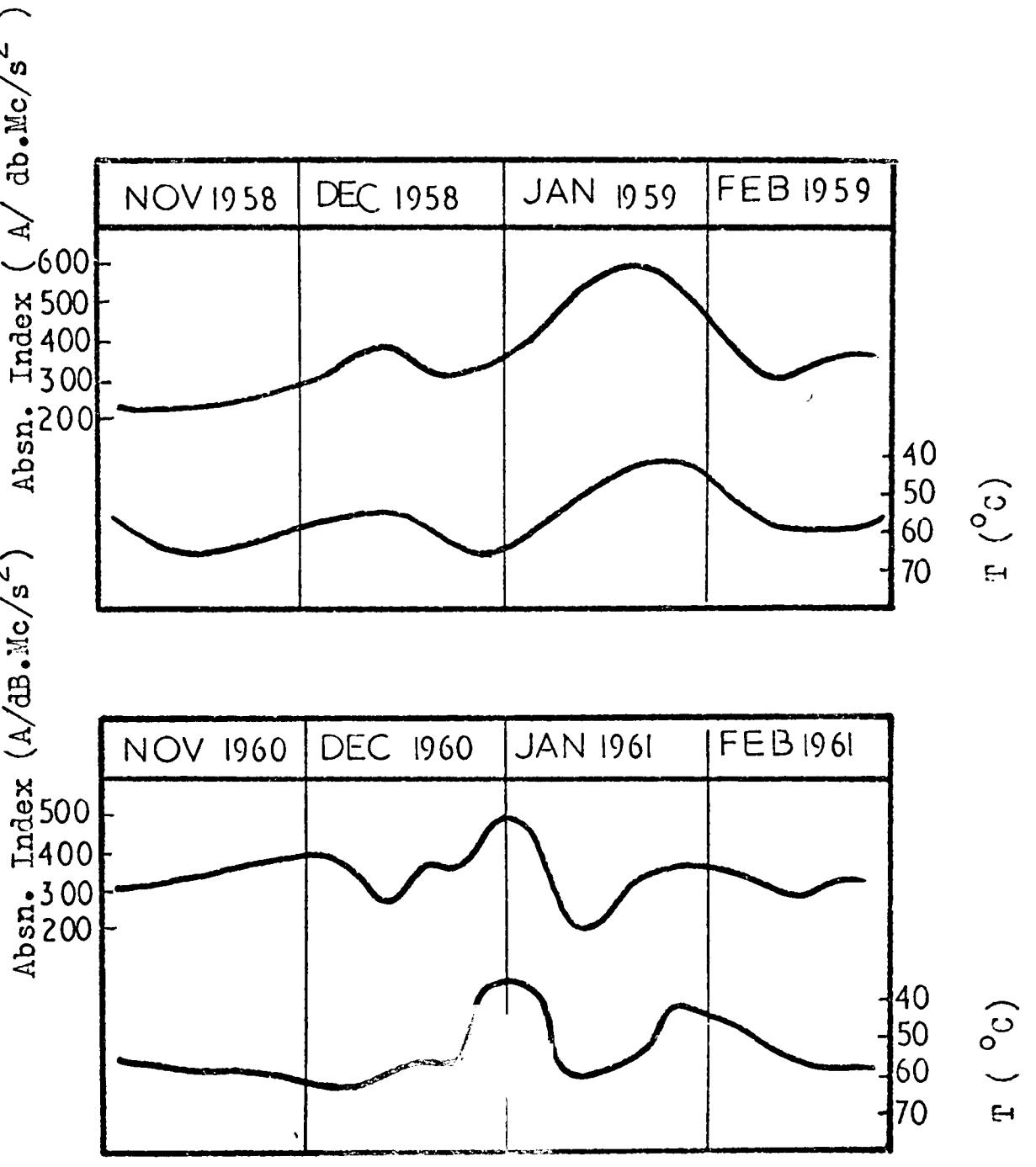


Fig. 2.3. Showing the correlation between the temperature at 30 km. and the ionospheric absorption index, corresponding to electrical activity near 70 km. (after Bossolasco and Elena, 1963).

Kalkstein (1962, 1963) in which a quantity of Rhodium 102 was released into the atmosphere at 43 km. The material was detected at an altitude of 100 km. shortly after the burst, but it was over a year before an appreciable quantity appeared below the 20 km. level. Kalkstein deduced that downward transport to the lower stratosphere appears to occur preferentially at high latitudes in the winter.

Bhandari (1970) has studied the phenomenon or downward transport across the stratopause, using both natural (cosmogenic) and artificial radioactive tracers. He suggests that mesosphere to stratosphere exchanges are strongly seasonal, taking place mainly around spring; this conclusion is contrary to that of List et al. (1966) who claim that the histories of materials injected into the mesosphere are identical and independent of season of injection.

2.3. Spring and Autumn Reversals.

Fig. 2.4. illustrates the very large changes of wind direction, from easterlies in summer to westerlies in winter, which occur in the upper stratosphere. These must involve large changes in relative angular momentum. Momentum can be transported vertically or meridionally by mean circulations, large scale disturbances or eddy processes. Observations in the upper stratosphere are quite inadequate to compute the magnitude of any of these processes at the present time.

2.4. Ozone heating.

Because of its very strong absorption in the ultraviolet, ozone plays a very important part in the radiative balance of the atmosphere. As well as being the principal source of thermal energy in the stratosphere it makes a significant contribution to infra-red energy transfer within the region. Since ozone has such a crucial role in the atmosphere, the many unexplained irregularities which occur in its distribution are of great interest. There is evidently a correlation between ozone distribution and various stratospheric phenomena such as sudden warmings (Craig, 1965), and there are large seasonal variations. There is also

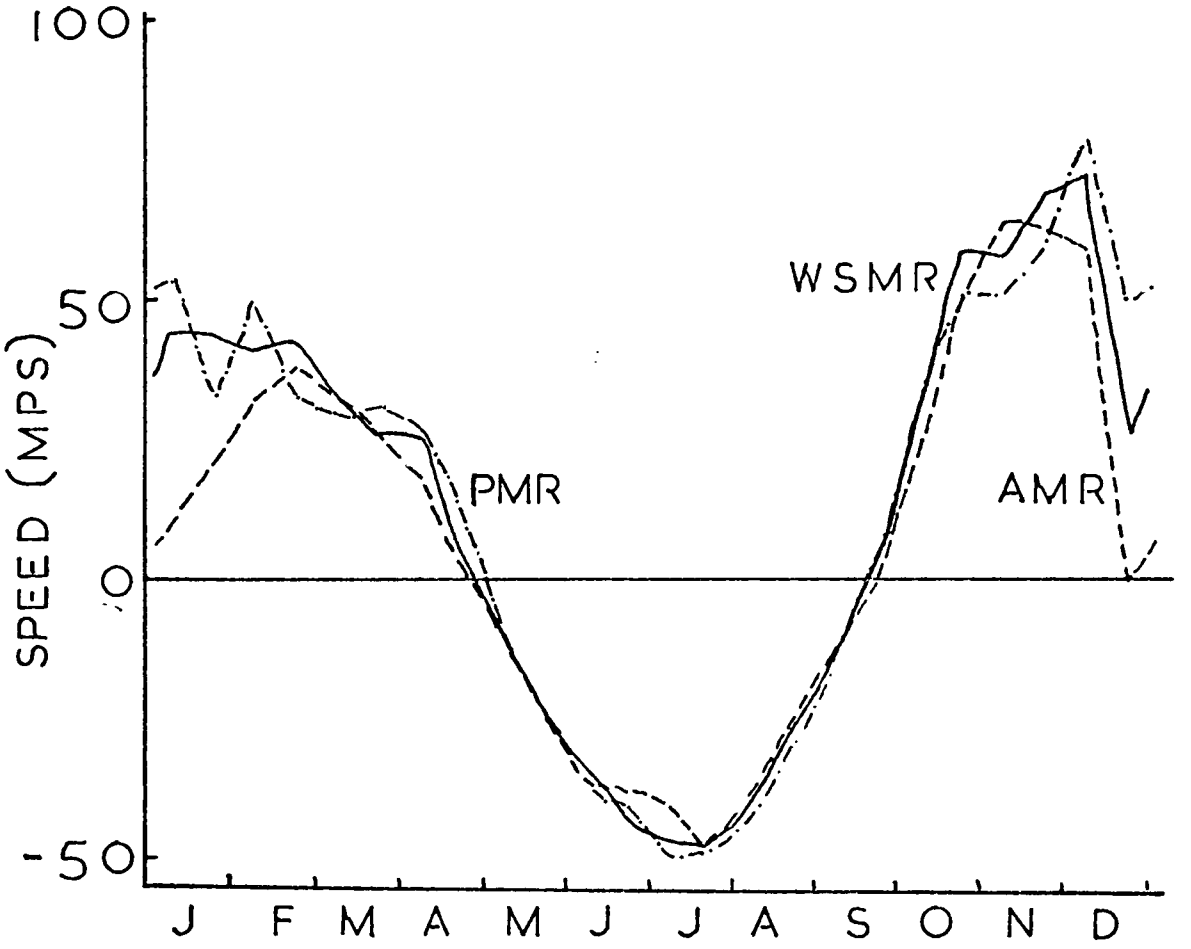


Fig. 2.4. The variation of wind direction and speed in the upper stratosphere with season for three rocket stations (White sands, Pacific, and Cape Kennedy) at different longitudes. (After Webb, 1966a).

transport of ozone from the low-latitude upper stratosphere to the high-latitude lower stratosphere during the winter months, but not in the summer. Evidently the observed vertical distribution of ozone and the seasonal and latitudinal variations of total ozone are intimately linked with the circulation of the stratosphere, although the relationship is not clear yet. In particular, the relative contributions of the mean circulation and eddy disturbances are not known.

2.5. Temperature Structure.

Such measurements as are available of the temperature structure of the mesosphere indicate an anomalous situation whereby an unexpected second maximum of temperature occurs between 65 km. and 80 km. in winter (fig. 2.5), and where the summer temperatures near the mesopause are unexpectedly low, being less than the corresponding winter values at the same latitude. These findings are quite contrary to expectations based on the radiative theory of the region, and may or may not be typical of the region, implying a more complicated structure than previously believed.

Fig. 2.6 shows temperature maps obtained from the two highest channels of the selective chopper radiometer on Nimbus 4. A remarkable amount of interesting structure is shown at 45 km., much more than at 35 km. at the same time. One would therefore expect to find a lot of interesting detail on the 55 km. and 65 km. maps, when they become available.

The question of diurnal temperature variations in the stratosphere and mesosphere is a particularly complex one. In theory, the amplitude of the variations should be small in the lower stratosphere, where the relevant atmospheric time constants are large compared with 24 hours, and should increase with height as the thermal capacity falls and the energy input increases. However, the effect of enhanced molecular diffusion at large mean free paths will tend to damp the oscillations, and efficient convection may do the same in the mesosphere (Webb, 1966). Beyers and Miers (1965) have observed both a steady increase in height

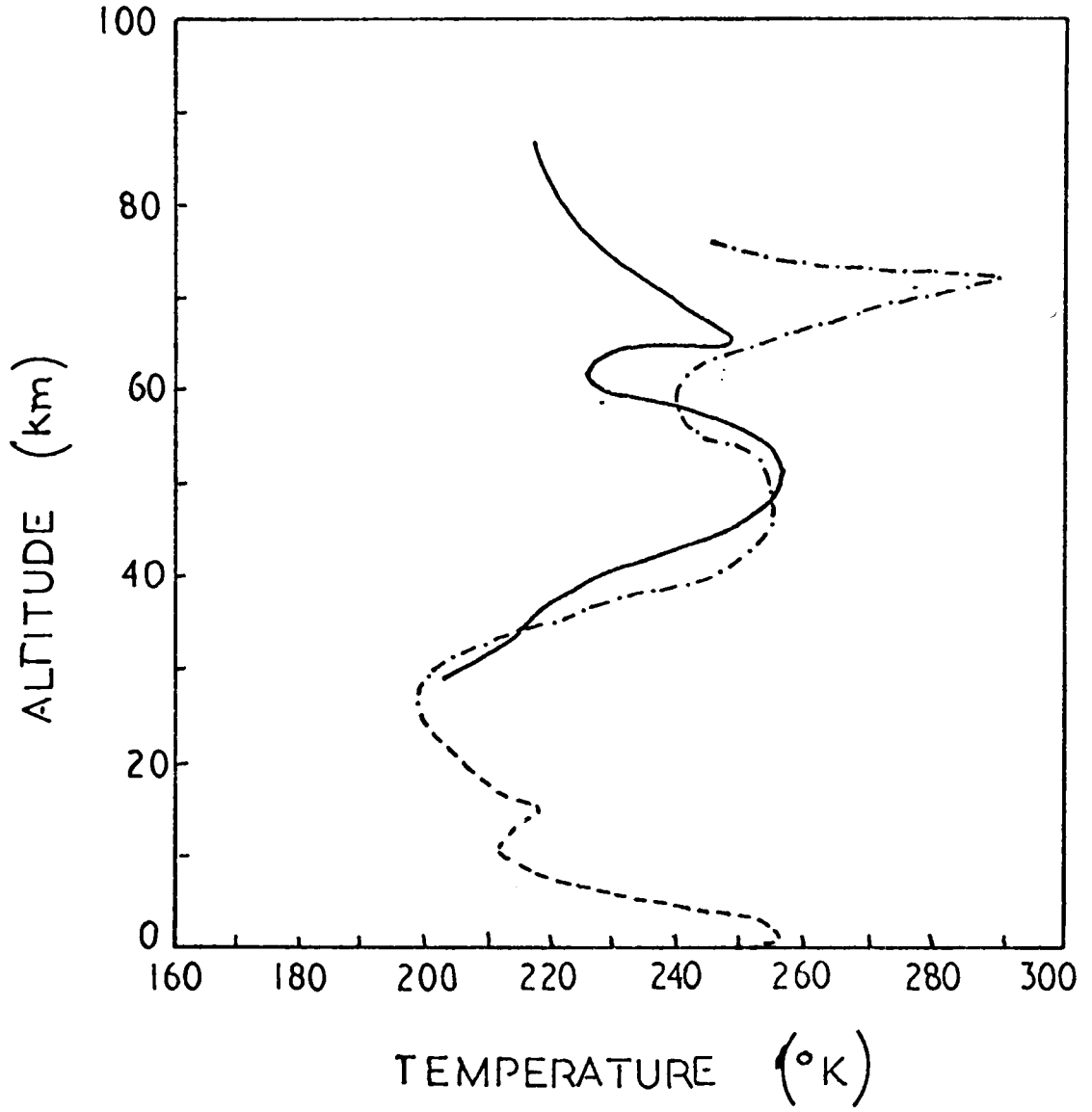
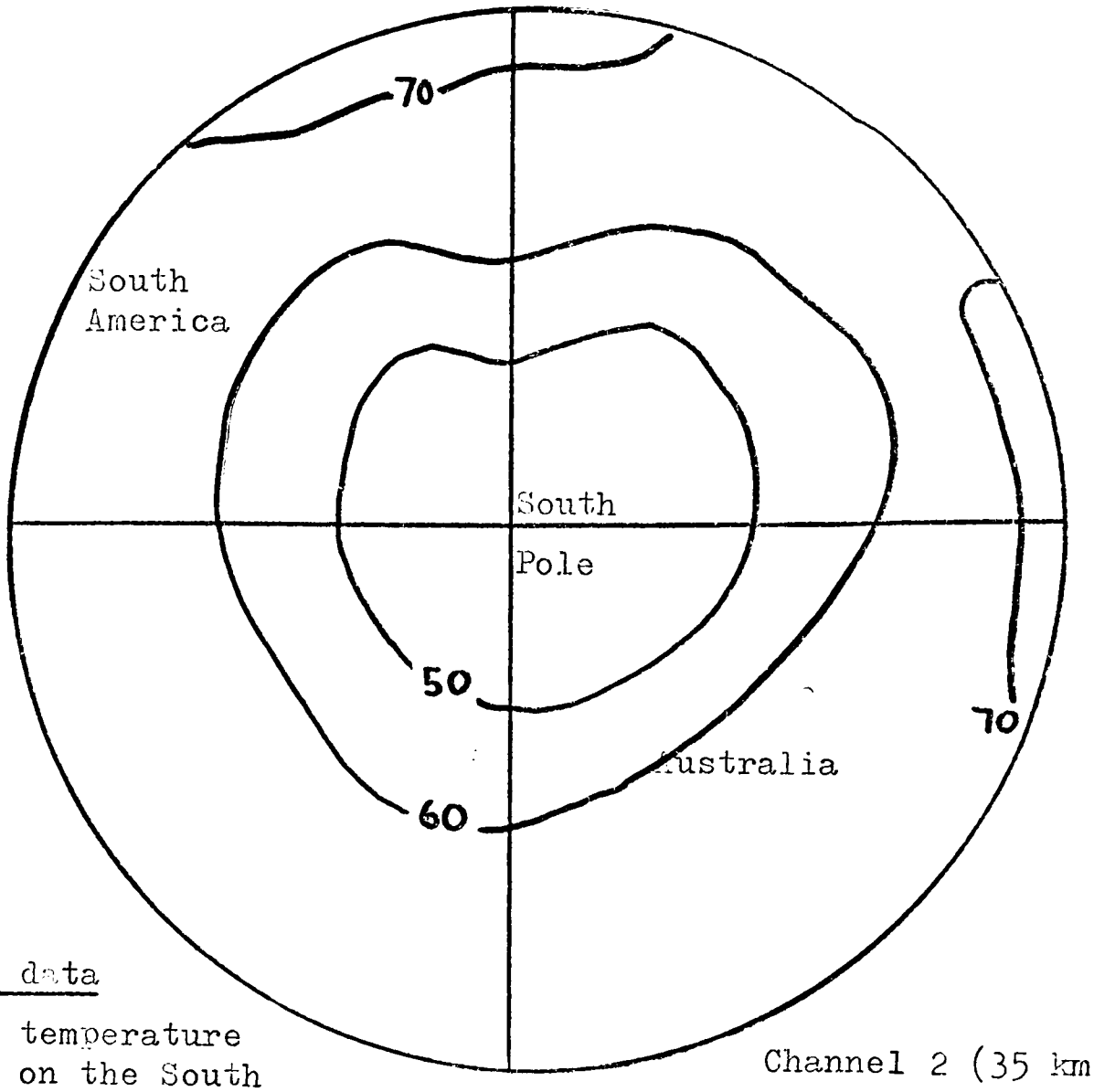
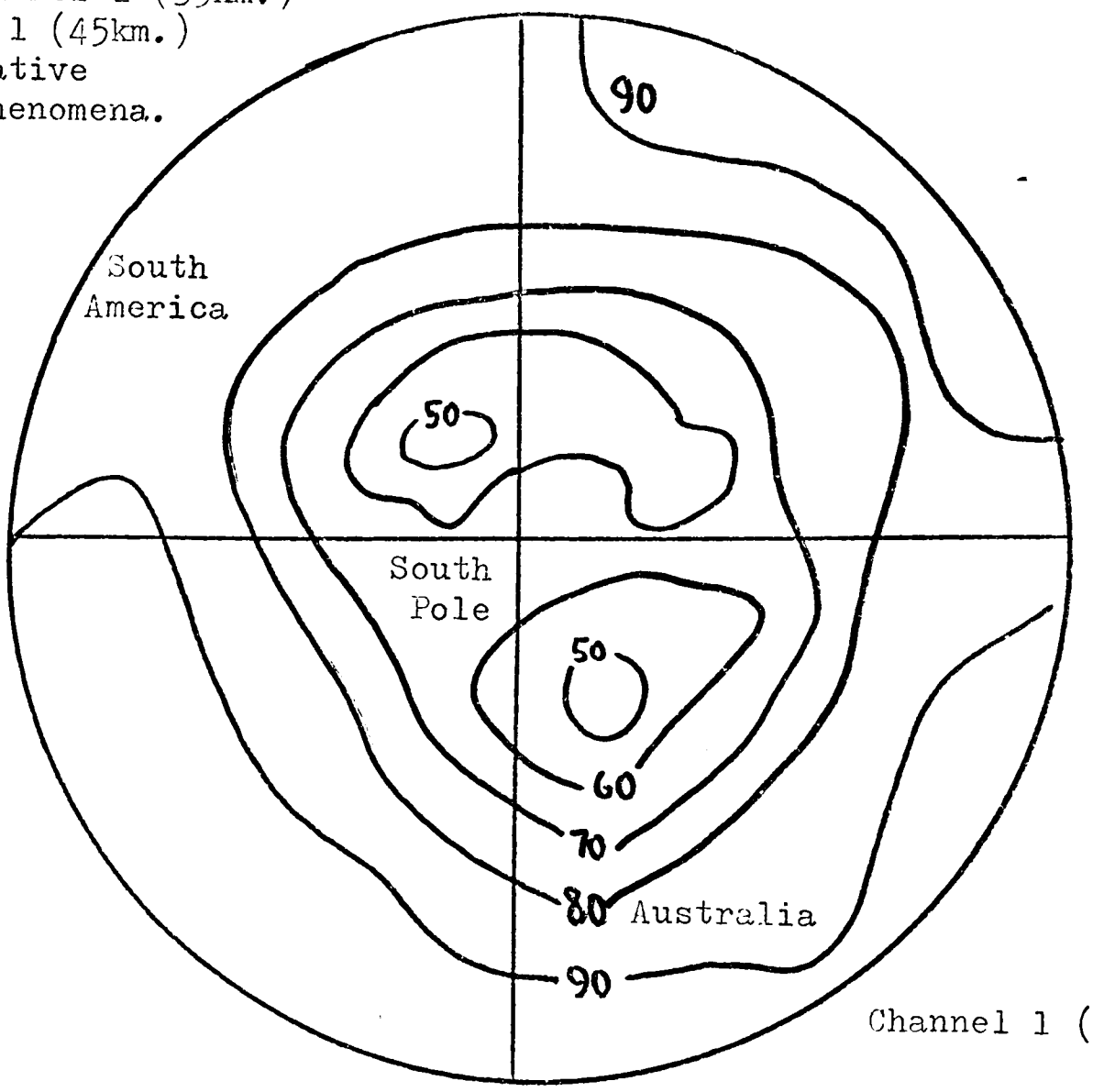


Fig. 2.5. Temperature profiles above Churchill for two days in December 1957 (2200 hrs. on 11th., dotted; 1500 hrs. on the 14th, solid) showing an unexpected second maximum in the mesosphere. (After Stroud et. al.,1960).



Channel 2 (35 km.)



Channel 1 (45 km.)

Fig. 2.6.
Nimbus 4 SCR data

Simultaneous temperature maps centred on the South Pole for Channel 2 (35km.) and Channel 1 (45km.) showing relative detail of phenomena.

(in February) and a much more complicated pattern (in November) in which diurnal effects were small until above 50 km. (fig. 2.7). Their measurements show swings of up to 20°K in the mesosphere, and those of Finger and Woolf (1967) are of the same order, although both used the rocket thermistor technique, the accuracy of which has been questioned (Wagner, 1964). The rocket grenade technique used by Theon et al. (1967) produced results on the phase of diurnal temperature variations which were quite contrary to those found by users of the thermistor method, while McClatchy and Shaw (1969) made measurements by a balloon-borne radiometric technique which found no diurnal variation at all in the 30-39 km. region, in conflict with both types of rocket sonde.

It is clear that more, and more reliable, measurements are needed to resolve the situation. It would be particularly interesting to study the seasonal dependence of the diurnal temperature variation at different levels.

2.6. Sudden and Explosive Warmings.

Temperature changes of as much as 30 deg.C in a few days are a regular winter feature of the lower stratosphere. Similar features have been observed in the upper stratosphere; an example is shown in fig. 2.8 in which the effect did not penetrate below the 25 km. level. Quiroz (1969) has reported a major warming of the 10 mb. level, in which supporting rocket soundings established the occurrence of warming to at least 70 km. It is interesting to speculate about the possibility of independent mesospheric warmings.

2.7. The Ionosphere.

Features of the ionospheric D-layer such as the anomalous winter absorption are probably linked with the mesospheric circulation. This is a phenomenon whereby unusually large electron densities are found in patches of about 1000 km. in extent, occurring only at high latitudes in winter. The effect is not correlated with solar activity in any obvious way, but does seem to coincide with anomalities in the temperature

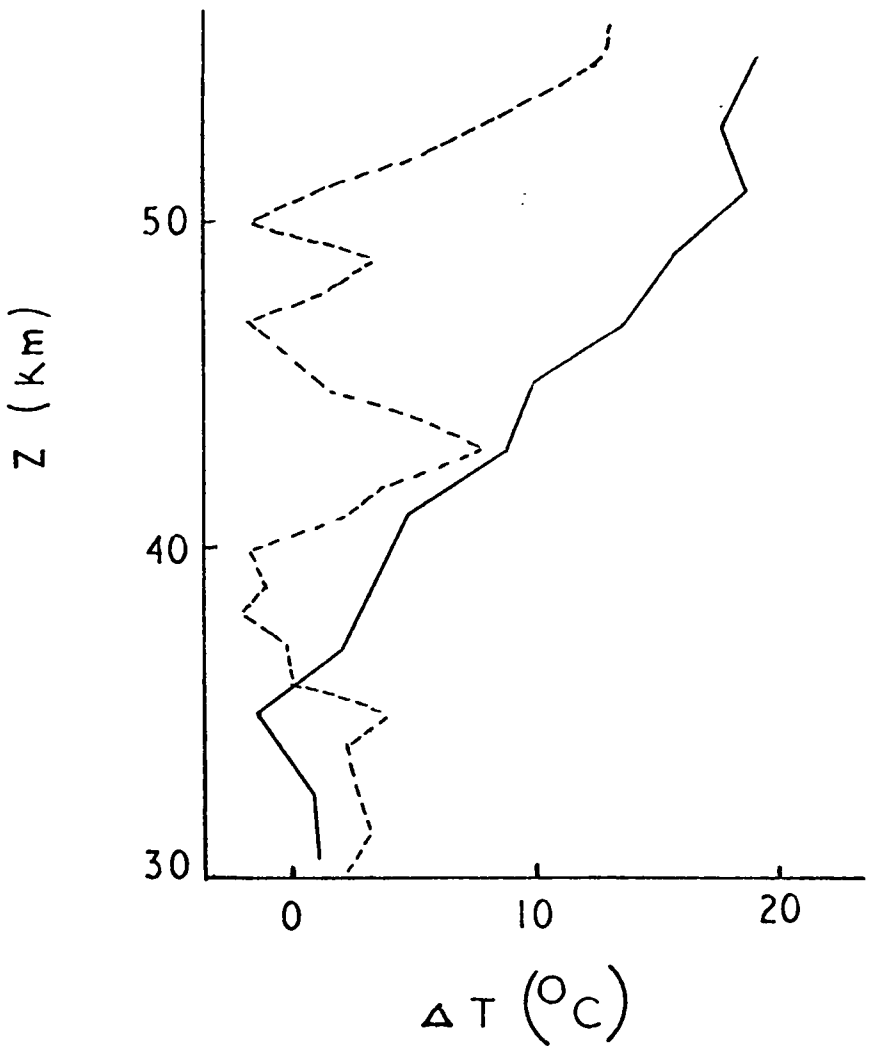


Fig. 2.7. Amplitude of Diurnal Temperature Changes.
(After Beyers and Meirs, 1965).

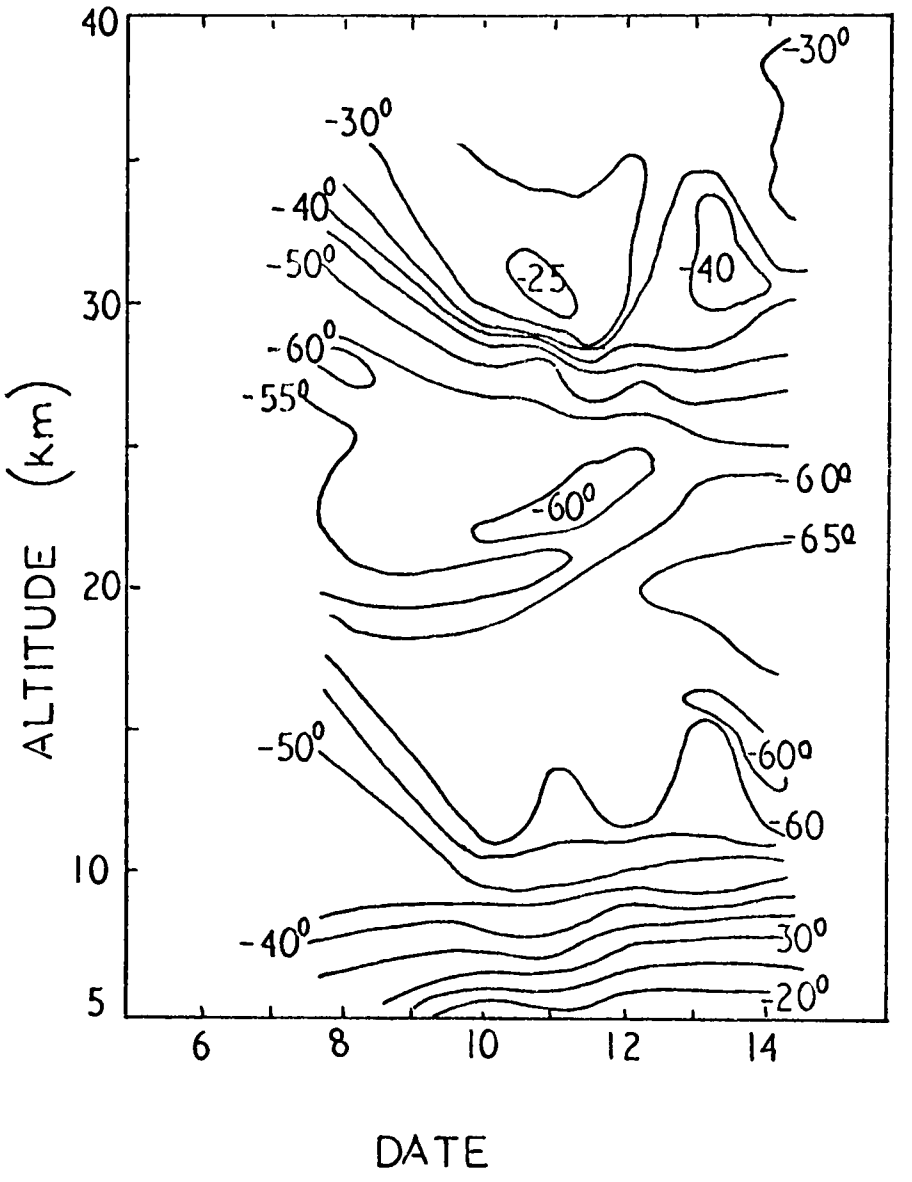


Fig. 2.8. A time-height cross-section of temperature (°C) over New Jersey for a period in January, 1960, showing a sudden warming of the upper stratosphere similar to those which are commonly observed at much lower levels (After Conover, 1961).

and density of the mesosphere (Mawdsley, 1961).

Other D-region irregularities have been observed by studying the echoes of radio waves at various frequencies. The same frequency can be reflected from several different altitudes at any given time, or several different frequencies from the same level, attributed to irregularities of ionisation of unknown origin. Craig (1965) notes that the average horizontal spacing of the irregularities is about the same (5 km.) as the scale of the vertical wind shears in the mesosphere, but there is no further evidence yet that the two are connected.

2.8. Gravity Waves.

The motions of the stratosphere and mesosphere contain a large amount of detailed vertical structure, which can be observed in meteor trails, sodium trails, and in the structure of noctilucent clouds. The motion is normally described as turbulent, and indeed the thermal and kinetic structures tend towards instability so that considerable turbulent activity may be expected. However, similar apparently irregular activity in the lower thermosphere (80-120 km.) has been convincingly explained by Hines (1960) in terms of the superposition of various modes of organised wave motion. It is possible that this is a general physical process which extends quite naturally to lower regions. Fig. 2.9 shows the exponential relationship between the vertical scale of eddy phenomena and the height at which they occur. The curves are quite continuous through the stratosphere, mesosphere and lower thermosphere, implying that the same mechanism is at work in each. Gille (1966) states that the propagation of gravity waves must depend markedly on the temperature structure, but that the exact nature of the dependence remains obscure. The contribution of heating due to the viscous damping of the waves and consequent dissipation of their kinetic energy may also be significant in the energy budget of the region.

2.9. Noctilucent clouds.

These consist of relatively high concentrations of particulate matter at very high levels, near the mesopause, and they only appear under very

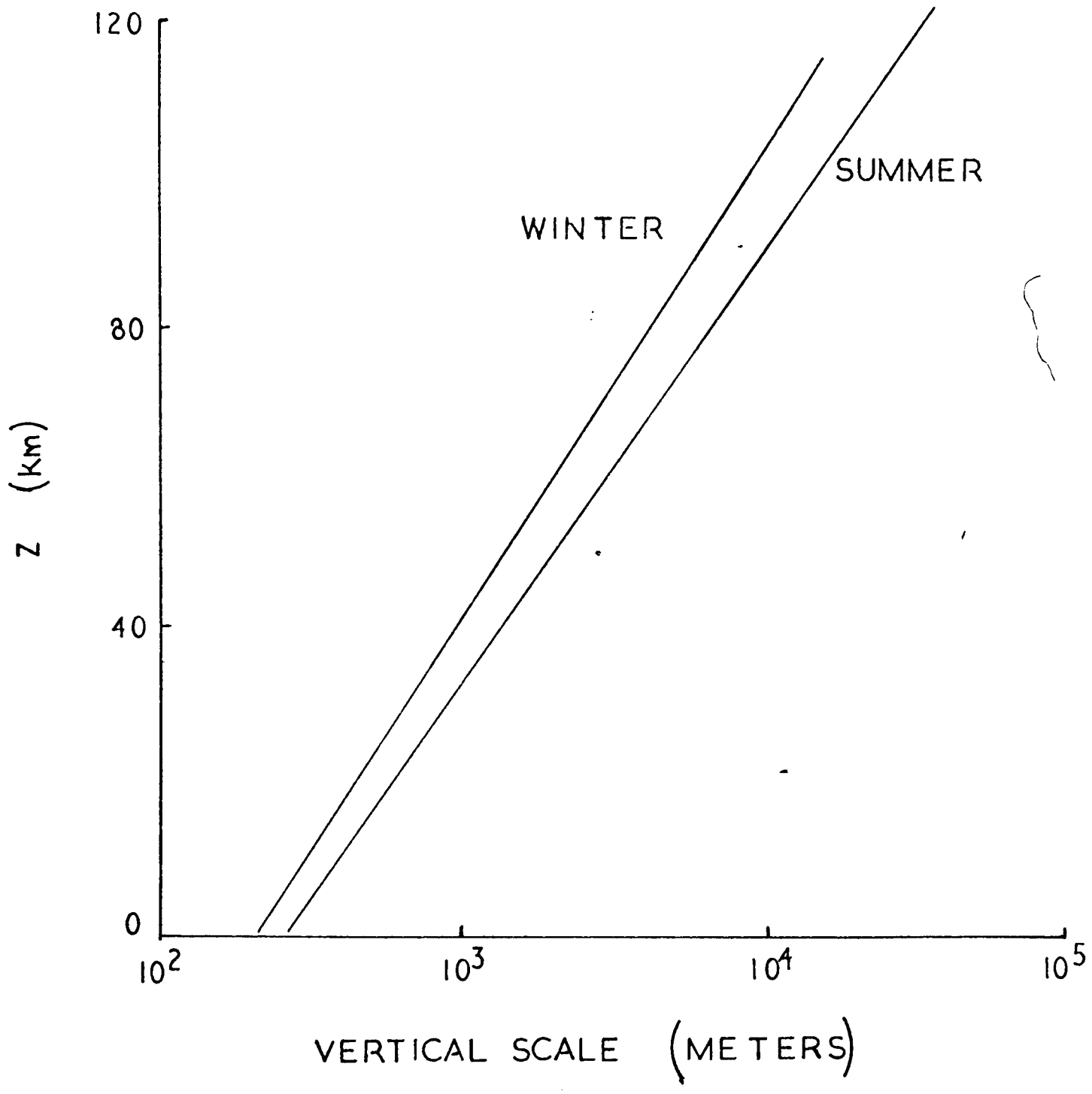


Fig. 2.9. Variation of vertical dimensions of detail structure with altitude (Webb, 1966).

special conditions near the summer solstice, and then only infrequently. The nature and origin of the particles making up the clouds is the subject of controversy. It has been variously suggested that they are ice crystals, or that they are minute solid particles of either volcanic or meteoric origin. The ice crystal theory appears to require either more water vapour than is generally believed to be present or lower temperatures than are generally observed at the mesopause. Ludlam (1957) has calculated that if the water vapour mixing ratio of 10^{-6} observed in the lower stratosphere by frost-point hygrometer measurements is continued to the mesopause, the vapour density there would be about 3×10^{-4} gm.cm.$^{-3}$ and would require an improbably low temperature of less than 145^{o}K for saturation. On the other hand, attempts to correlate the appearance of the clouds with meteor showers or volcanic activity have not been successful.

In 1963 a sampling of mesospheric temperatures using the rocket-grenade technique by scientists at the University of Stockholm (B.A.M.S., 1963) fortuitously coincided with an appearance of the clouds. They quote an unusually low temperature of 130^{o}K at the mesopause, compared with 150^{o}K when the clouds were not present. However, Theon et al. (1967) recorded temperatures of 130-140^{o}K at the mesopause on all of a large sample of soundings, and noticed no significant difference in the temperature obtained during or in the absence of a display. If all observations of noctilucent clouds could be related to a measurement of mesospheric temperature, strong evidence for or against the ice-crystal theory would be forthcoming. A value for the mixing ratio of water vapour at the mesopause would also be obtained.

2.10. Heat Budget.

Meteorological conditions in the stratosphere require that the atmosphere should transport heat in a meridional direction. Order of magnitude calculations show that radiative transfer plays a major role in this (Murgatroyd and Goody, 1958). The contribution of heat transport

by eddy processes is still unclear because the computations involved require wind and temperature measurements in the upper stratosphere with a much greater abundance and accuracy than is available so far.

The nature of transport mechanisms in the mesosphere is even more obscure. Some attempts have been made to compute the circulation patterns responsible for the observed situation of a warm mesopause in winter and a cold mesopause in summer. Murgatroyd and Singleton (1961) derived a simple model from gross assumptions, including the conjecture that eddy transfer was negligible, as did Haurwitz (1961). The use of different approximations led to different solutions in each case. Murgatroyd and Singleton's results showed a flow from summer pole to winter pole, with upward motion in the summer hemisphere and downward motion in the winter hemisphere. Haurwitz found, for the winter, poleward motion between 50 and 80 km., with equatorial motion above and below. The true situation will not be known until the appropriate empirical evidence is available.

2.11. Conclusions.

A large amount of experimental data is required before the ignorance embraced by the topics discussed above can be dispelled. In most cases, temperature data is the most important; it is also the easiest atmospheric parameter to measure from space. The next chapter deals with the derivation of a suitable experimental technique.

Chapter 3.

Experimental Techniques for Upper-Atmosphere Temperature Sounding

3.1. Basic Principles.

The infra-red radiation arriving at a satellite from the atmosphere below contains information on the temperature of the emitting gases. This information may be interpreted from radiometric measurements made by the satellite provided the distribution of the emitter is known, and provided it is in thermodynamic equilibrium with its surroundings so that

the emission is related to the temperature by Planck's formula. The varying opacity of the atmosphere with wavelength enables radiation originating principally from a chosen level to be selected by the choice of a suitable spectral interval. The simultaneous measurement in a number of such intervals could theoretically yield a complete temperature profile of the atmosphere below the satellite (Kaplan, 1959).

3.2. Theory.

At a given frequency ν, the extinction of radiative flux in the atmosphere is proportional independently to the intensity of the flux F_ν, and to the absorber amount u, by Beer's Law

$$dF_\nu = -k_\nu F_\nu \, du \qquad (3.1)$$

which defines the absorption coefficient k_ν at that frequency. k_ν has units of $(\text{atmos.cm})^{-1}$ if u is in atmos.cm.; the units of F_ν are watts cm^{-1} steradian^{-1}. The emission is also proportional to the amount of matter, so

$$dF_\nu = k_\nu J_\nu \, du \qquad (3.2)$$

from Kirchoff's law, where J_ν is called the source function and has the same units as F_ν. If the atmosphere is in thermodynamic equilibrium at the level in question, then J_ν is equal to the Planck function B_ν. Combining both equations gives

$$dF_\nu = -k_\nu (F_\nu - B_\nu) \, du \qquad (3.3)$$

which is called Schwartzchild's equation. If we denote the transmission of the atmosphere at frequency ν by τ_ν and define it by

$$d\tau_\nu = k_\nu \tau_\nu \, du \qquad (3.4)$$

so that the transmission between any level at which the pressure is p and the top of the atmosphere is

$$\mathcal{T}_\nu = \exp\left(-\int_0^p k_\nu \, du\right) \tag{3.5}$$

we can write

$$dF_\nu = -\frac{d\mathcal{T}_\nu}{\mathcal{T}_0}\,(F_\nu - B_\nu) \tag{3.6}$$

or

$$\mathcal{T}_0\, dF_\nu + F_0\, d\mathcal{T}_\nu = B_\nu\, d\mathcal{T}_\nu \tag{3.7}$$

which on integration gives

$$F_\nu = \int_0^1 B_\nu\, d\mathcal{T}_\nu = \int_0^\infty B_\nu \frac{d\mathcal{T}_\nu}{dz}\, dz \tag{3.8}$$

for the flux F_ν at the frequency ν arriving at the satellite, where z is vertical distance above the ground. This flux is therefore a weighted mean of the Planck black body flux from all levels in the atmosphere, and the weighting function is simply the derivative with respect to height of the transmission at that frequency. This quantity is susceptible to calculation or laboratory measurement, and B_ν is a function only of frequency and temperature, given by the well-known formula

$$B_\nu(T) = \frac{2h\nu^3}{c^2\left[e^{h\nu/kT} - 1\right]} \tag{3.9}$$

in which h is Planck's constant and c the velocity of light (Planck, 1913).

The monochromatic weighting function $d\mathcal{T}_\nu/dz$ is computed from (3.4) by substituting the Lorentz formula for the profile of pressure-broadened spectral lines

$$k_\nu = \frac{1}{\pi}\,\frac{\alpha}{(\nu-\nu_0)^2 + \alpha^2} \tag{3.10}$$

where $S = \int_0^\infty k_\nu d\nu$ is called the strength of the line and $\alpha = \alpha_0 p/p_0$ is the line half-width, a linear function of pressure. Some single-frequency weighting functions are shown in fig. 3.1; the shape and height of the peak depends very strongly on the choice of ν. If ν did not coincide with any atmospheric line, then the weighting function would be a δ-function at the ground. If it coincides with the frequency of a strong line centre then the weighting function would be peaked high in the atmosphere, and would be zero at $z = 0$. Weighting functions peaked anywhere in the atmosphere are theoretically available by choosing ν such that the peak lies between these extreme cases. In practice monochromatic weighting functions cannot be obtained, because they imply infinite spectral resolution and zero energy grasp. Any real function will have the form $\int_{\Delta\nu}\int_0^\infty \frac{d\tau_\nu}{dz}\, dz\, d\nu$ and will be wider than that corresponding to a single frequency (fig. 3.2), implying reduced vertical spacial resolution.

3.3. Instrumentation.

(i) Grating Spectrometer. Kaplan's original suggestion was for a grating spectrometer selecting ten intervals in the 15μ band of CO_2, each with a width of five wavenumbers. The suggestion was taken up by Wark et al. (1966) who designed and built first a 'breadboard' and then a high-altitude balloon model of such an instrument, successfully demonstrating its suitability for satellite use. The device was finally launched into orbit on Nimbus III in April, 1969, and James (1969) has reported the production of excellent temperature profiles.

Ground level temperatures were obtained from a channel in the atmospheric window at 11.1μ, and the highest weighting function, peaked at 40 km., was obtained from an interval in the Q-branch of the band, where absorption is strong and the corresponding path length a minimum. The instrument cannot generate weighting functions peaked higher than this, because the resolution of 5 cm^{-1} is large enough to admit three or more complete spectral lines, and this channel is already selecting the strongest part of the band.

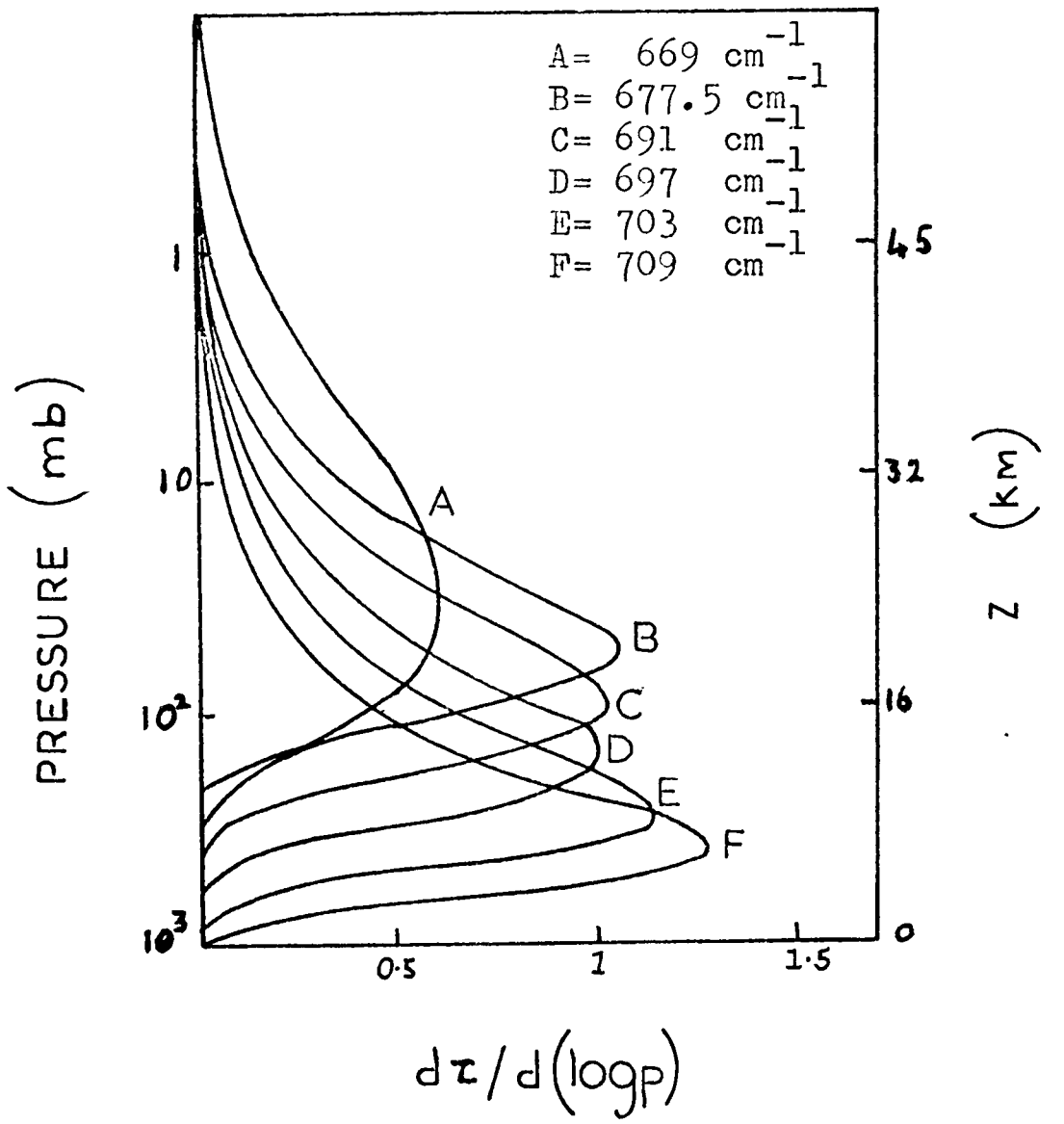


Fig. 3.1. Six theoretical weighting functions corresponding to single frequencies lying within the 15 micron band of CO_2. (Wark and Fleming, 1966).

(ii) Michelson Interferometer. The Michelson is superior to the grating spectrometer in two main respects; firstly, it uses circular apertures, rather than slits, and secondly, it measures many spectral elements simultaneously rather than individually. These all contribute to a much larger overall energy grasp, but a high price must be paid in terms of instrument complexity and arduous mathematics to interpret the data. The problem has received much attention lately, however, and a Michelson device has already flown on Nimbus 3.

Unfortunately the Michelson is not capable of a spectral resolution better than about 1 cm^{-1}. This is narrow enough to select the centre of the Q-band, raising the peak of the highest weighting function by perhaps as much as 10 km. over the grating spectrometer, but it is still much greater than the widths of individual lines in this band (about 0.07 cm^{-1} at surface pressures).

(iii) Parallel Plate Interferometer. An important feature of the P and R branches of the 15μ carbon dioxide spectrum is that the strongest lines are regularly spaced about 1.6 cm^{-1} apart. Houghton (1961) suggested that use could be made of this fact by tuning a parallel-plate interferometer to the same spacing, and thus collecting energy corresponding to the same absorption coefficient from each line. In this way a very high spectral resolution could be combined with a good energy grasp.

Abel (1966) has described some preliminary experimental work on a solid interferometer made of germanium. He concluded that the very highest precision would be required to produce an operational instrument with adequate performance. It does not seem likely that weighting functions peaked above the stratopause could be produced in this way.

(iv) Radiometers. Simple radiometers were the first kind of instrument to be used to make temperature measurements from satellites, because they are relatively robust and easy to make. The spectral interval is selected by an interference filter only, and so is fairly wide (about 500 cm^{-1} for TIROS II, for example). The resulting weighting functions are correspondingly broad, and the temperatures obtained were means over the whole stratosphere.

(v) Selective Chopper Radiometer. Radiometer weighting functions can be considerably sharpened by the use of an absorption cell containing a selected atmospheric gas as an additional spectroscopic element. The selective chopper radiometer of Houghton, Smith et al. (1966) uses narrow-band filters to isolate intervals of the 15μ band of CO_2, and a cell containing this gas as a chopper. The detected radiation is therefore only at the frequencies absorbed in the cell, and it originates mainly at the same optical depth in the atmosphere. To observe the lowest levels, radiation from the wings of the pressure-broadened CO_2 lines must be selected. Frequencies corresponding to these wings are not present in radiation from higher levels, because the pressure is lower and the lines narrower (fig. 3.3). Such a selection is made by removing the line centres with a fixed low-pressure path of CO_2. Chopping with such a path length would produce the inverse effect, i.e. the selection of line centres rather than their exclusion, and would result in the detection of radiation from very high levels. Fig. 3.2 compares a specimen selective chopper radiometer weighting function with that corresponding to a good spectrometer and to the ideal monochromatic weighting function; it is almost as sharp as the latter, implying near optimum vertical resolution.

Balloon flights with such an instrument have been described by Abel (1966) and a satellite version was launched on Nimbus D in April 1970.

(vi) Limb Scanning Devices. All of the preceding approaches may theoretically be used to examine high levels in the atmosphere by a limb scanning approach, whereby the field of view is directed at an angle to the vertical such that it intersects the level of interest tangentially. Very high spectral resolution is now no longer an advantage, since the weighting function will tend to be peaked at the highest pressure in the line of sight, i.e. at the desired level. This means that a relatively large spectral band pass may be used, and this partially offsets the very small field of view which must be used to obtain adequate vertical resolution. However, the method remains unattractive in view of the difficulties encountered in pointing the

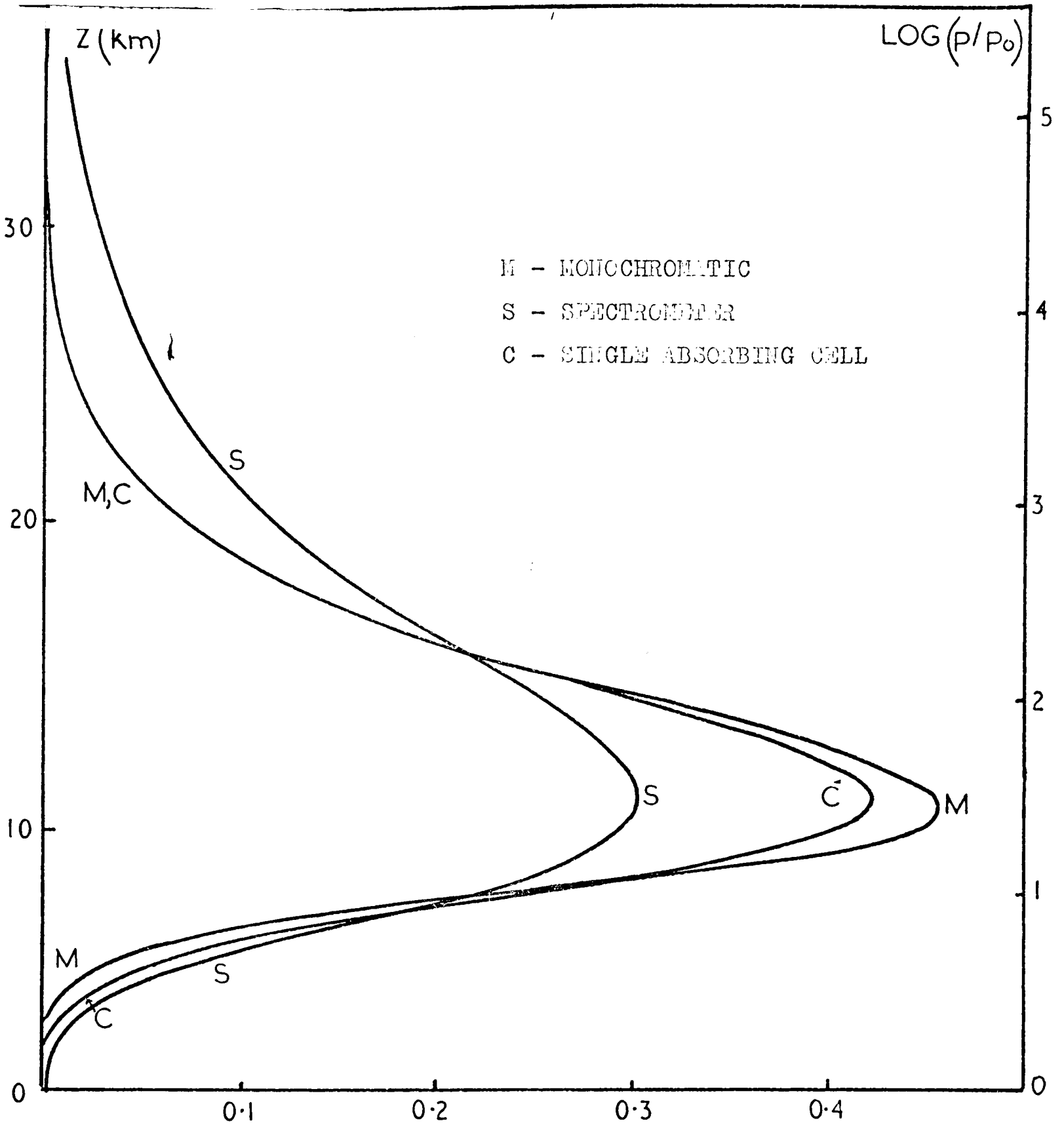


Fig. 3.2. Comparison of a monochromatic weighting function with that obtained using a spectrometer of 5 cm^{-1} resolution and that for the spectrometer plus a path of CO_2. (After Peckham, Rodgers, Houghton and Smith, 1966).

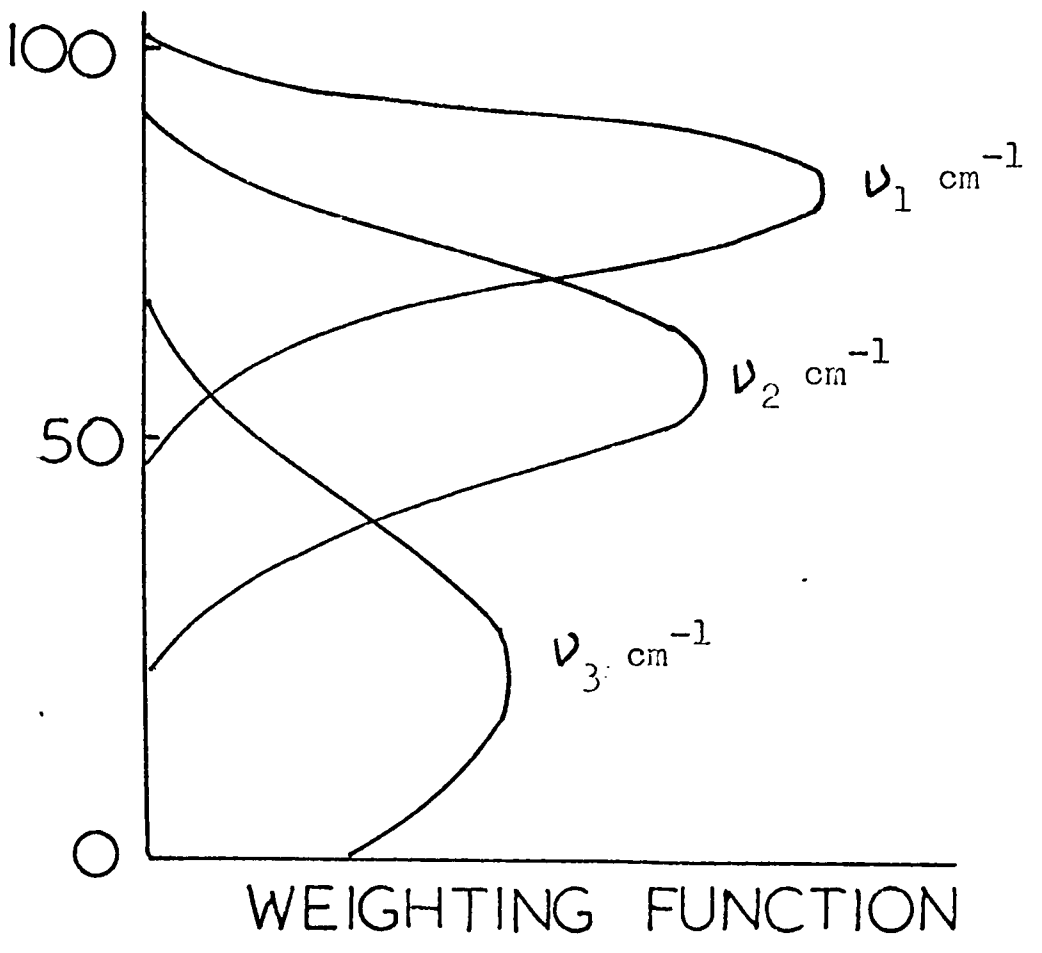


Fig. 3.3. Relative line width as a function of height and the weighting function for three frequencies within a single line. The line widths are not to scale.

viewing aperture to the very high accuracy required, and was rejected in favour of the neater approach described in the next paragraph.

(vii) The Pressure-Modulated Selective Chopper Radiometer. To generate weighting functions peaked in the upper stratosphere and mesosphere, when viewing vertically, an effective spectral resolution of the same order as the line widths at the corresponding pressures is required. These widths range typically from 0.001 cm^{-1} at 30 km. to 0.0001 cm^{-1} at 65 km., and may be contrasted with 5 cm^{-1} for the resolution of a good grating spectrometer and perhaps 1 cm^{-1} for a Michelson. The selective chopper radiometer may, in principle, be used to operate at these levels simply by using a low enough pressure in the chopping cell. In practice, chopping between two different paths must always lead to a small spurious signal since it is not possible to balance the transmissions of the two paths exactly. At very low cell pressures fluctuations of this imbalance signal tend to mask the true signal, so that useful accuracy is no longer obtained. For the Nimbus D instrument, the lower pressure limit for an absorbing path 1 cm. long has been set at about 50 mb., giving a weighting function peaked near 45 km. as the highest obtainable.

Rodgers and Williamson (1964) suggested that this difficulty could be removed and higher levels sounded by the use of a pressure modulated or path length modulated system in which the optical path between the detector and the atmosphere was fixed and only the amount of absorbing gas varied. A crude preliminary calculation based on this idea predicts that an accuracy of $\pm$ 1°K at 70 km. is feasible (Sect. 4.4.) The further development of this approach is the subject of the remainder of this thesis.

3.4. Choice of band.

The frequency interval in which the radiometer operates must lie within a spectral band of a suitable atmospheric constituent. Previous efforts in this field have concentrated on the infra-red spectrum of carbon dioxide, since it has two strong, isolated bands at frequencies

(667 cm^{-1} and 2350 cm^{-1}) at which good optical components and detectors are available, and because carbon dioxide is uniformly distributed in the atmosphere up to at least 80 km. (Sect. 4.3(v)), so that the problem of discriminating between signals produced by changes in concentration and temperature do not arise. The choice between the two suitable bands of CO_2 (the other bands of this molecule are either very weak or coincident with bands due to another species) was made on the basis of the following criteria:

(i) The ν_2 band (at 15μ) lies near the peak of the terrestrial black-body curve (fig. 1.1) and $B_\nu(T)$ is many orders of magnitude larger than for the ν_3 band at 4.3μ at the same temperature. However, $\partial B_\nu/\partial T$ is a more important quantity, and this is greater at 4.3μ, where the slope of the Planck curve is steeper.

(ii) The best detectors at 4.3μ are nearly 10^3 times more sensitive than the best detectors at 15μ.

(iii) The ν_3 band is stronger by a factor of 3 than the ν_2 band.

Another interesting band is that of oxygen at about 5 mm., in the microwave region of the spectrum. It is more difficult to handle optical components, detectors, etc. for this wavelength than for the infra-red, and serious difficulties of interpretation are introduced by the Zeeman splitting of the spectral lines.

Overall, it appeared that the 4.3μ band of CO_2 represented the best choice, a conclusion which later turned out to be fallacious (Chapter 6).

Chapter 4. Theoretical Study.

4.1. Weighting Functions.

The experimental configuration of fig. 4.1 is envisaged. Denoting the weighting function by $K(h,z)$ we have

$$K(h,z) = \frac{d}{dz}\int_0^\infty \tau(z,h,\nu)\,\tau_o(\nu)\,\tau_c(\nu,t,p_{co})\,\tau_D(\nu)\,d\nu \qquad (4.1)$$

where $\tau(z,h,\nu)$ is the transmission of the atmospheric path from height z to the radiometer at height h

$\tau_o(\nu)$ is the transmission of the windows and filter

$\tau_c(\nu,t,p_{co})$ is the transmission of the gas in the absorbing cell, at a mean pressure of p_{co}

$\tau_D(\nu)$ is the transmission of the detector optics.

The transmission of the atmospheric path is given by

$$\tau = \exp\left(-\int_{u(z)}^{u(h)} k_\nu\,du\right) \qquad (4.2)$$

where the absorption coefficient k_ν is given by the Lorentz formula (leaving the effect of Doppler broadening of the lines aside until later)

$$k_\nu = \sum_i \frac{S_i}{\pi} \quad \frac{\alpha_i\, p/p_o}{\left[(\nu-\nu_i)^2 + \alpha_i^2 p^2/p_o^2\right]} \qquad (4.3)$$

where ν_i is the centre frequency of the ith line, which has width α_i cm^{-1} at standard pressure p_o, and S_i is its strength in units of $mb^{-1}cm^{-2}$. If nearly all of the absorption is due to the strong lines in the band, i.e. those for which $\frac{S_i\,u\,p_o}{2\pi\alpha_i p} \gg 1$ then the approximation

$$k_\nu = \sum_i \frac{S_i}{\pi}\,\frac{\alpha_i\, p/p_o}{(\nu-\nu_i)^2} \qquad (4.4)$$

is valid and

$$\tau = \exp\left(-\sum_i \frac{S_i\alpha_i}{\pi(\nu-\nu_i)^2}\int_{u(z)}^{u(h)} p/p_o\,du\right) \qquad (4.5)$$

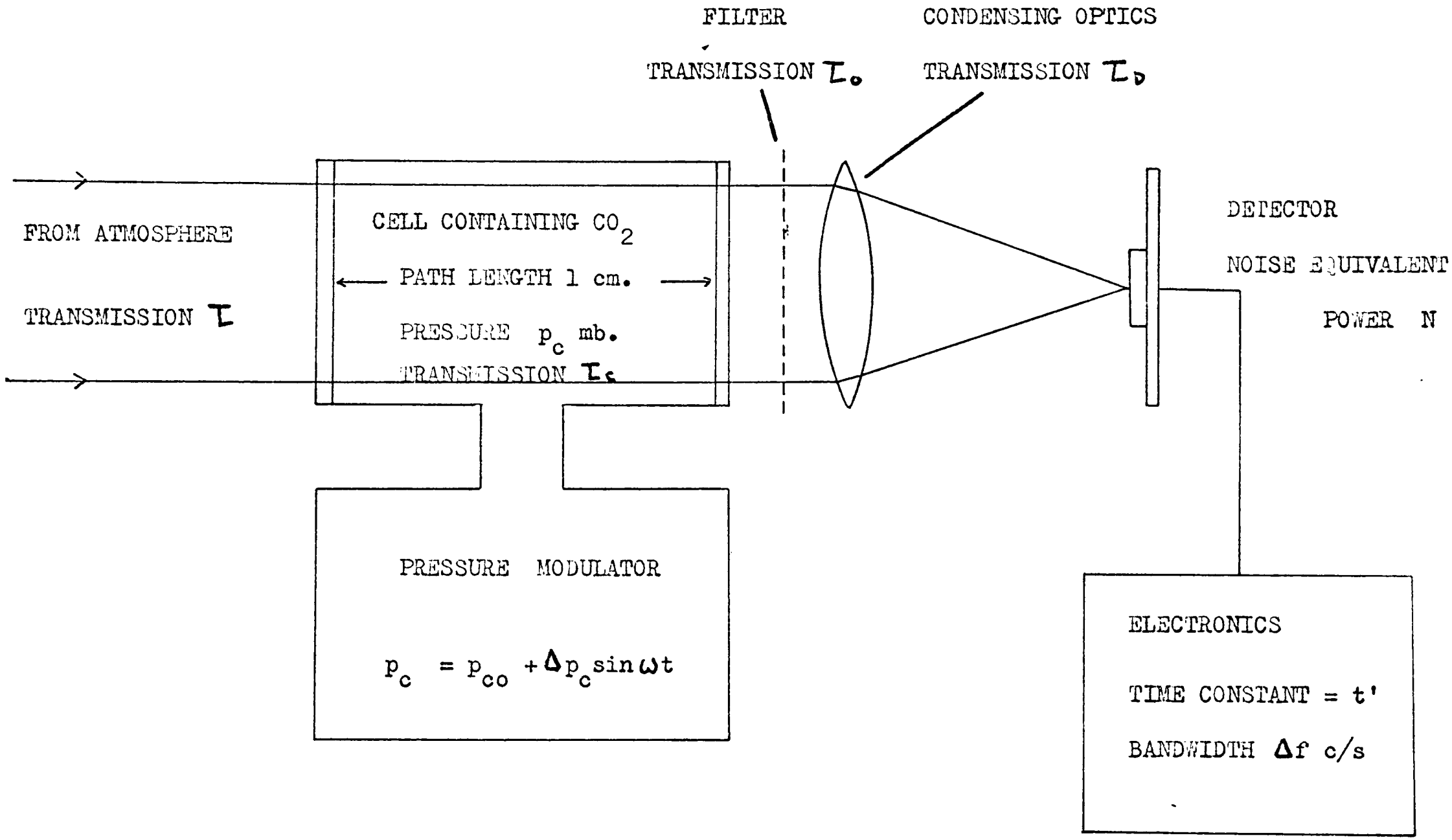


Fig. 4.1. Generalised systems for theoretical study.

Erratum. This is a bit confusing as it stands. If (4.8) is derived without making the approximation (4.4), then the solution is that determined by Ladeberg and Reiche and includes Bessel functions. If $\frac{S_i u \rho_o}{2\pi\alpha_i \rho} \gg 1$ (strong absorption) then it simplifies to give (4.9). A simpler and more direct approach, which does not require us to invoke Ladeberg and Reiche, is to make the simplification from the outset (as here) which leads to (4.8) as shown: this can now be integrated directly to give (4.9).

FWT

For a satellite h is ∞ and the absorber amount u between the instrument and the level z is $\int_z^\infty \rho\, dz = a\rho$, where $a = \int_0^\infty \frac{\rho}{\rho_0} dz$ is the total path length of CO_2 in the atmosphere, so

$$\tau = \exp\left(-\frac{u p^2}{2 p_0} \sum_i \frac{S_i \alpha_i}{\pi(\nu-\nu_i)^2}\right) \tag{4.6}$$

Similarly, for the path of CO_2 in the cell,

$$\tau = \exp\left(-\frac{l p_c^2}{p_0^2} \sum_i \frac{S_i \alpha_i}{\pi(\nu-\nu_i)^2}\right) \tag{4.7}$$

where l is the length of the cell and p_c is its pressure. α_i in (4.7) has to be multiplied by a factor $(1+\beta)$ to allow for the self-broadening of the lines in the pure CO_2 of the cell. (4.1) then becomes

$$K(z) = \frac{d}{dz}\int_0^\infty \tau_0 \tau_D \exp\left[-\left(\frac{u p^2}{2 p_0} + \frac{(1+\beta) l p_c^2}{p_0}\right)\sum_i \frac{S_i \alpha_i}{\pi(\nu-\nu_i)^2}\right] d\nu \tag{4.8}$$

The solution to an integral of this type has been given by Ladeberg and Reiche (1913) in terms of Bessel functions of the first kind with imaginary arguments. For strong absorption an approximation is valid, which gives

$$K(z) = \frac{d}{dz}\left\{2\sum_i \tau_0(\nu_i)\tau_D(\nu_i)\left[\left(\frac{u p^2}{2 p_0} + \frac{(1+\beta) l p_c^2}{p_0}\right)\sum_i (S_i \alpha_i)\right]^{1/2}\right\}$$

$$= \frac{u p^2}{p_0}\left(\frac{a p^2}{2 p_0} + (1+\beta)\frac{l p_c^2}{p_0}\right)^{-1/2} \sum_i \tau_0(\nu_i)\tau_D(\nu_i)(S_i \alpha_i)^{1/2} \tag{4.9}$$

The cell pressure p_c is time-dependent and may be written

$$p_c = p_{c0} + \Delta p_c \sin \omega t \tag{4.10}$$

If $p_{c0} \gg \Delta p_c$, p_c^2 in the equation (4.9) may be replaced by

$(p_{co}^2 + 2 p_{co} \Delta p_c \sin \omega t)$ and the expression in brackets expanded as a binomial series. The component at frequency ω comes out as

$$K_\omega(z) = C \frac{a p^2}{p_o^2} (1+\beta) l \Delta p_c p_{co} \left(\frac{a p^2}{2 p_o} + \frac{(1+\beta) l p_{co}^2}{p_o} \right)^{-\frac{3}{2}} \sin \omega t \quad (4.11)$$

where $C = \sum_i \Gamma_o(\nu_i) \Gamma_D(\nu_i) (S_i \alpha_i)^{1/2}$ is a constant for a given experimental configuration. It is present in the expression as a multiplier and so does not affect the shape of the curve, nor the height of the peak, but merely the scale. The irrelevant factors are removed by normalizing the weighting function, so that

$$\int_0^\infty K_\omega(p)\, dp = 1$$

which gives

$$K_n(p) = \frac{p^{*2}}{(1+p^{*2})^{3/2}}, \text{ where } p^* = \left(\frac{a}{2(1+\beta) l} \right)^{1/2} \frac{p}{p_{co}} \quad (4.12)$$

The shape of the weighting function depende only on p^*, i.e. only on the mean cell pressure p_{co} and the length of the cell l. If the instrument is inside the atmosphere, for example on a balloon, rather than above it, the same expression holds except that α is a further parameter. Equation (4.12) shows that K tends to $1/p$ near the ground, where p is large, and to p^2 at very high levels, where p is small. The peak is at the altitude where the pressure is

$$p_{peak} = \left(\frac{4(1+\beta) l}{a} \right)^{1/2} p_{co} \quad (4.13)$$

For a weighting function peaked in the mesosphere at 65 km., equation (4.13) implies a cell pressure of only $\frac{1}{3}$ mb. The pressure swing will be even smaller. The chopping action of such an insignificant amount of gas will clearly be slight, and it is necessary to consider whether the modulated energy arriving at the detector is sufficient to produce a useful signal.

4.2. Energy Considerations.

The r.m.s. energy arriving at the detector at the chopping frequency ω is given by

$$E_\omega(T) = \frac{1}{\sqrt{2}} A \Omega \bar{\tau} \left(\overline{B(T_a)} - \overline{B(T_{cell})}\right) \Delta W \qquad (4.14)$$

where A is the entrance aperture (cm^2), Ω is the angular field of view (steradians), $\bar{\tau}$ is an equivalent mean transmission for the optics and filter, $\overline{B(T)}$ is the Planck black body function averaged over frequency across the band, and T_a is the effective temperature of the atmosphere as seen by the instrument, i.e. a mean of the temperatures of every level weighted by the appropriate $K(z)$. T_{cell} is the temperature of the gas in the cell, and $\Delta W (cm^{-1})$ is the chopped equivalent width of the lines in the band. Without pressure modulation, the equivalent width of the cell path is given by

$$W = 2 \sum_i (S_i \alpha_i)^{1/2} [(1+\beta) \ell p_c^2]^{1/2} \qquad (4.15)$$

(strong line approx See eg Houghton & Smith — FWT)

If the pressure is modulated the equivalent chopped band pass is

$$\Delta W = 2 \sum_i (S_i \alpha_i)^{1/2} [(1+\beta) \ell]^{1/2} \Delta p_c \qquad (4.16)$$

The criterion determining the minimum useful energy at the detector is that the change in signal ΔE_ω produced by the smallest change in T which we need to measure should not be smaller than the instrument noise. The equation expressing this is

$$\Delta E_\omega = E_\omega(\Delta T) \geq N (\Delta f)^{1/2} \qquad (4.17)$$

where N is the noise equivalent power of the detector for a 1 c/s band width and $\Delta f = 1/2\pi t'$ sec^{-1} is the actual band width of

the electronics for a time constant of t' seconds. It is assumed that the noise contributed by the amplifiers is negligible compared to that due to the detector, a situation which can be established in practice.

4.3. Discussion of Assumptions.

Certain assumptions and approximations are made in the preceding derivations. These are justified in the discussions below.

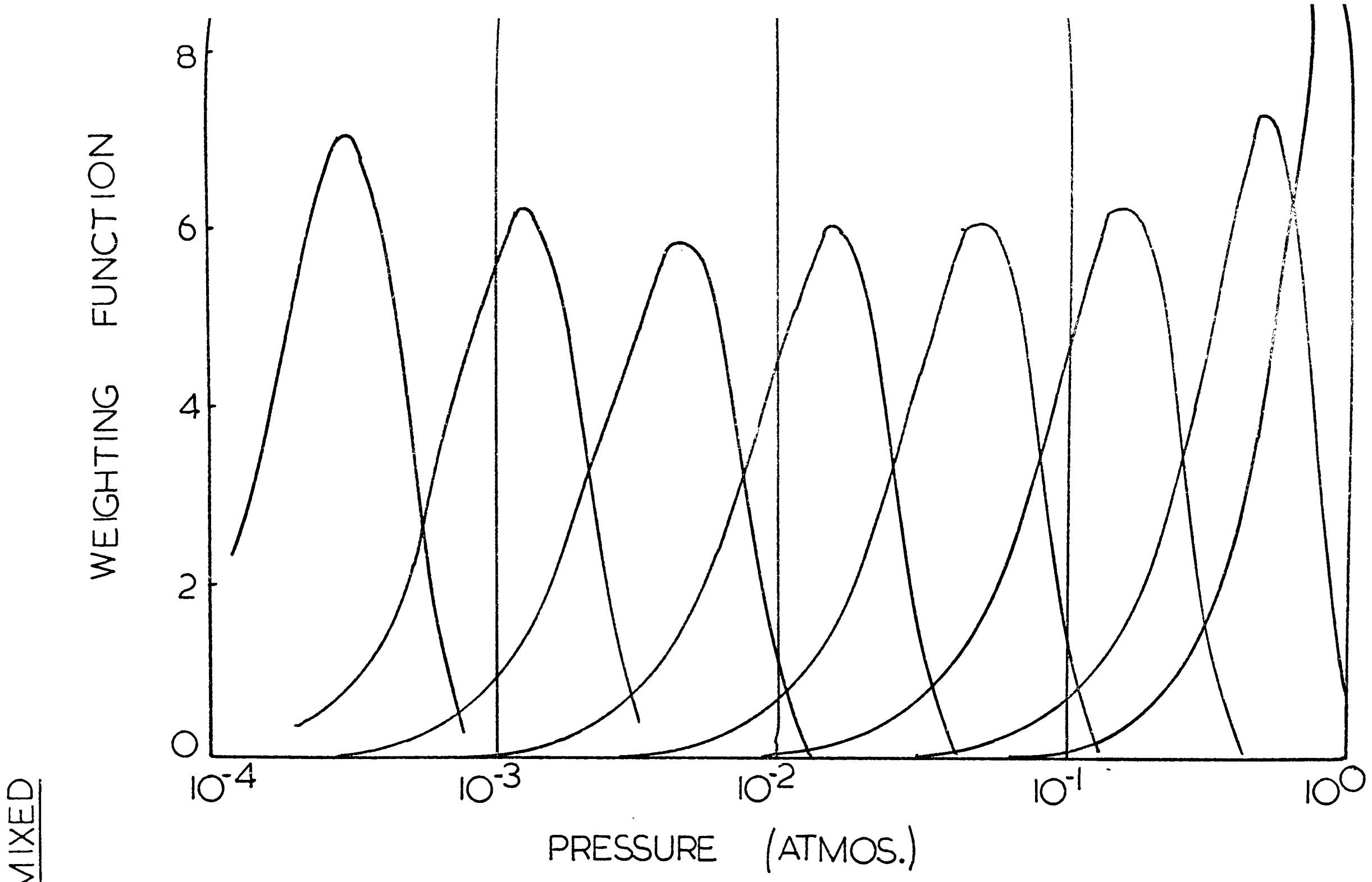
(i) Effect of Doppler Broadening. The shapes of the lines are only Lorentzian at levels where the pressure is high and the mean free path is small, i.e. effectively only below 30 km. Between 30 and 50 km. the effect of the Doppler contribution to the weighting function is negligible, because the effect is all in the line centre, which is strongly absorbed by the remaining gas in the levels above. Above 50 km., however, the Doppler contribution cannot be disregarded and the weighting functions should be computed on the basis of a mixed line shape. Such a computation is very complex, but Barnett (1970) has calculated weighting functions for a single line of mixed shape. Some of his results are shown in fig. 4.2, with the equivalent pressure broadened curves for comparison. The main dissimilarity is that the curves representing the real situation are peaked a little higher than those corresponding to the over-simplified case described above. This is advantageous in that the theoretical maximum sounding altitude of a projected satellite instrument is increased by some useful amount (around 5 km.), but it also means that the complex and laborious task of evaluating the mixed line shape weighting functions for the whole band will have to be tackled in order to obtain useful accuracy at high altitudes from a functional instrument.

(ii) Strong lines. The strong line approximation (eq. 4.4) is valid for lines which have

$$S \gg \frac{2\pi\alpha}{u} \qquad \text{(Goody, 1964)}$$

If we take

$$S > \frac{10\pi\alpha}{u} = \frac{10\pi\alpha_0}{l}$$


WEIGHTING FUNCTION
8
6
4
2
0
10^{-4}
10^{-3}
10^{-2}
10^{-1}
10^{0}
PRESSURE (ATMOS.)
MIXED

LORENTZ

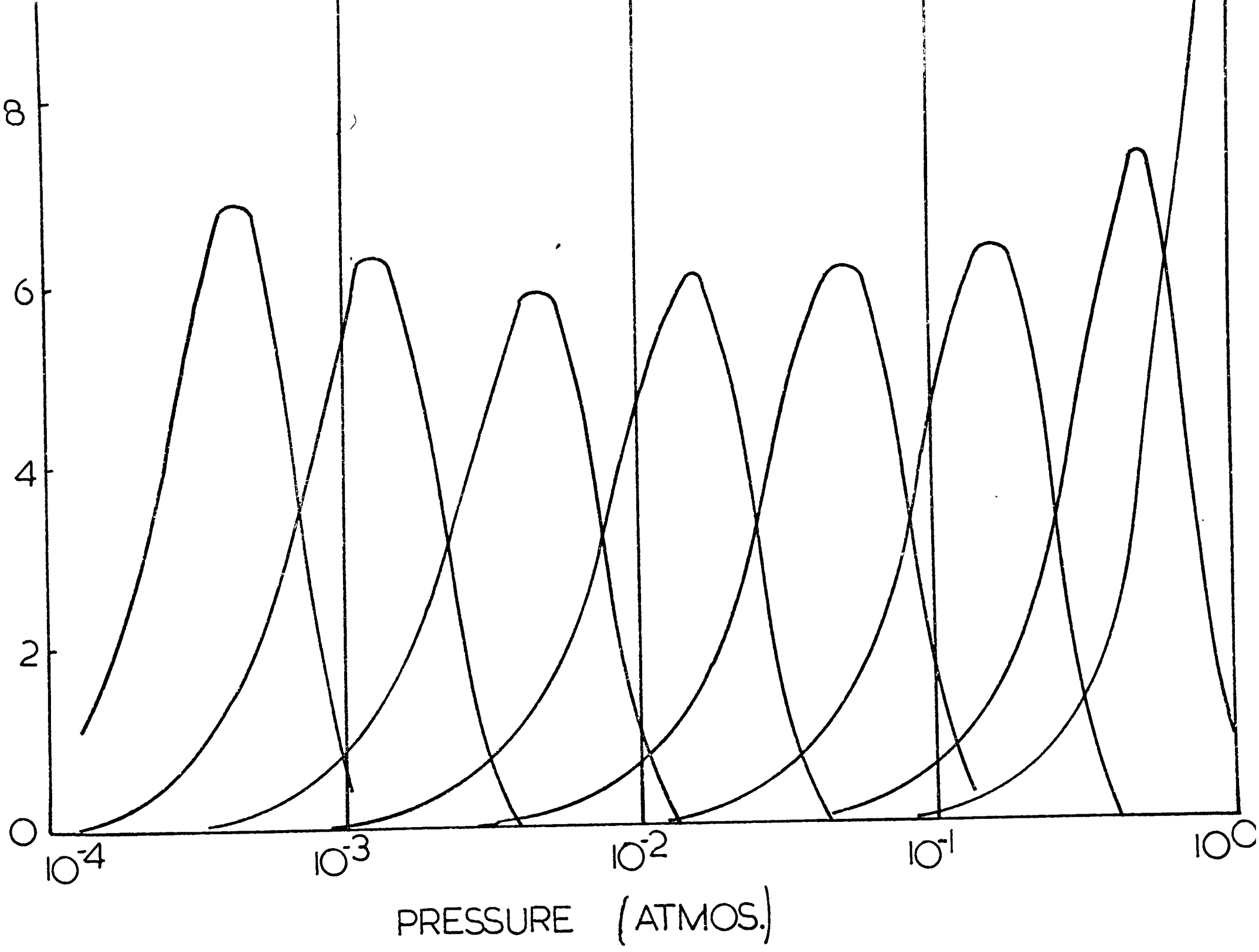


Fig. 4.2 (After Bumett, 1970)

as the criterion then it reduces to $S > 0.06$ a$_t$mos.$^{-1}$cm.$^{-2}$ for a cell of length 6 cm. and a mean line width of 0.07 cm^{-1}. Tables of the strengths of the lines in the 15μ band are available (Rodgers, 1968) and show that more than 97% of the strength of the band resides in lines for which this condition is valid.

(iii) Independent lines. It has been assumed that the lines do not overlap to any appreciable extent. This is certainly true for the pressures found at 30 km. or higher, so the speculative satellite calculations are not affected. At lower levels, however, such as those at which the balloon radiometer operates, the effect of overlapping is not negligible and must be taken into account. This problem was dealt with by an experimental technique described in Chapter 10.

(iv) Temperature Structure. The line shapes are temperature as well as pressure dependent, and weighting functions that are to be used to deduce accurate temperature profiles have to be corrected for the effect of the mean atmospheric temperature structure on their shape (see Chapter 10). The size of the correction required is not large enough to significantly alter the conclusions of sections 4.1 and 4.2.

(v) CO_2 distribution. It is assumed that the mixing ratio of CO_2 is constant at all levels of interest, except very near the ground where it is generated by combustion of fossil fuels and removed by photosynthesis in green vegetation. It is widely accepted (Junge, 1963) that sufficient mixing occurs to prevent the gravitational separation of gases up to at least 80 km., and CO_2 is both chemically and photochemically inert, having neither source nor sink within the atmosphere. Hagemann et al. (1959) have measured the mixing ratio up to 30 km. and report variations of less than 0.7%. A similar inconsequential variation, this time with horizontal displacement at 6 km. altitude, has been recorded by Kelley (1969) for samples taken over the North American continent. The horizontal and vertical

variations of the mixing ratio of CO_2 are probably even smaller in the height range 30-80 km. (Bischof, 1962).

4.4. Performannce of a Real Instrument.

Rewriting equation (4.17) using (4.14), the criterion for useful performance becomes

$$\frac{\sqrt{2}\,A\,\Omega\,\bar{E}\left(\bar{B}(T_a+\Delta T_a)-\bar{B}(\bar{T}_a)\right)\Sigma_i(S_i\alpha_i)^{1/2}[(1+\beta)\ell]^{1/2}\Delta\rho_c}{N\left(1/2\pi t'\right)^{1/2}} \geq 1 \qquad (4.18)$$

where the fraction on the left-hand side of the inequality is called the signal-to-noise (S/N) ratio.

The best detectors available for a satellite instrument are photoconductive indium antimonide, which have $N = 1.0 \times 10^{-11}$ watts r.m.s. at a wavelength of 4.3 μ. $\Sigma(S_i\alpha_i)^{1/2}$ for this band is about 125 atmos.$^{-\frac{1}{2}}$cm$^{-\frac{3}{2}}$ and β is about 0.3 (Burch et al., 1962). For a given orbital height of 1000 km. (typical of the Nimbus series) a field of view of $\Omega = \pm 5^\circ \equiv 0.024$ steradian gives an acceptable horizontal resolution of about 150 km. The viewed area would change completely every 30 seconds, so 15 seconds would be a suitable value for t'. Using these figures in equation(4.18)together with reasonable values for the physical dimensions ℓ and A of 6 cm. and 5 cm^2 respectively, shows that a satellite radiometer with a mean cell pressure of about 0.2 mb. and a modulation coefficient of about 0.33 should be capable of measuring a temperature change of 1°C at an altitude of 70 km. with a signal to noise ratio of 1. Very accurate temperature measurements in the stratosphere and mesosphere seem to be feasible. The next step was to construct a laboratory prototype instrument to verify the predictions of the theory.

Chapter 5. The 4.3 μ band Radiometer.

A laboratory prototype radiometer was built to test the theory, and to be the first step in the development of a sound practical design. The instrument described in this chapter evolved into the more successful design of chapter 7, and eventually into the flight model of chapter 8.

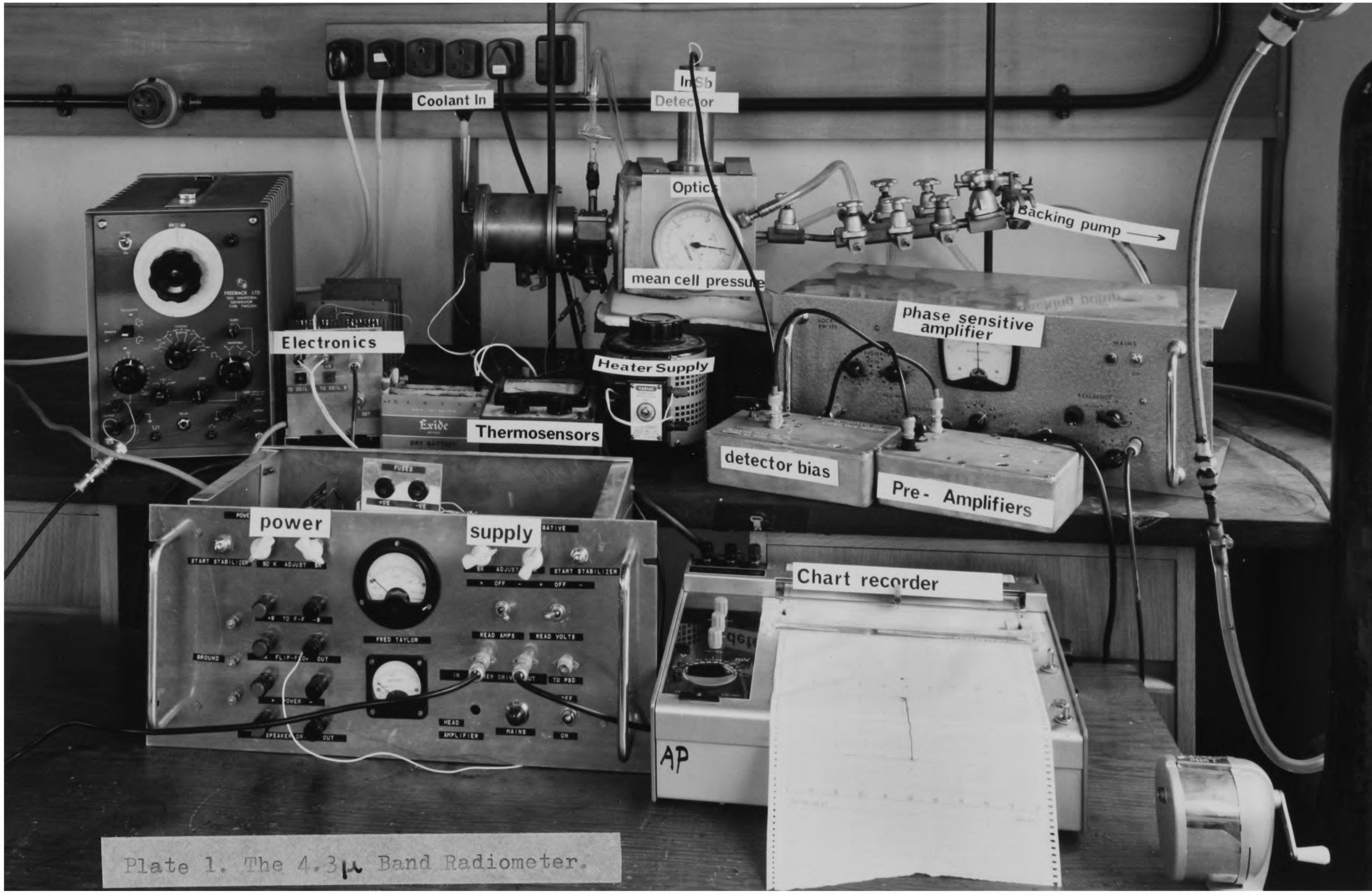
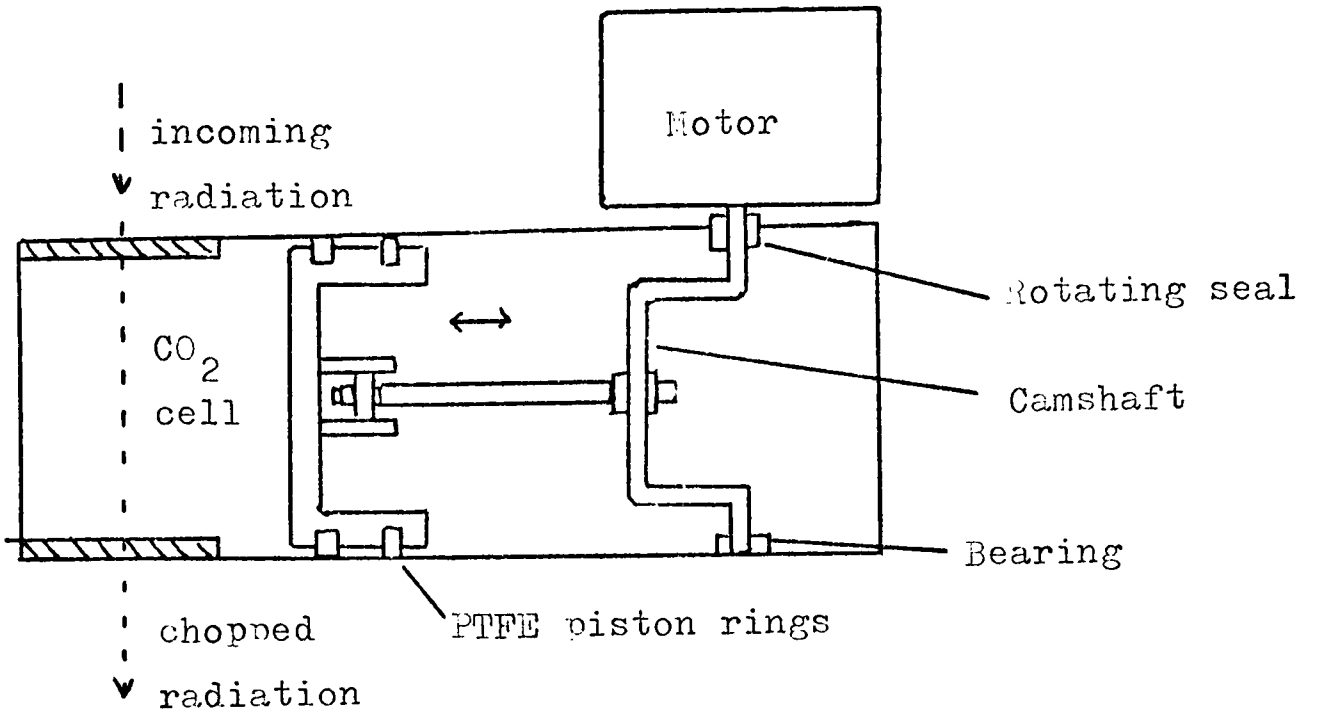


Plate 1. The 4.3μ Band Radiometer.

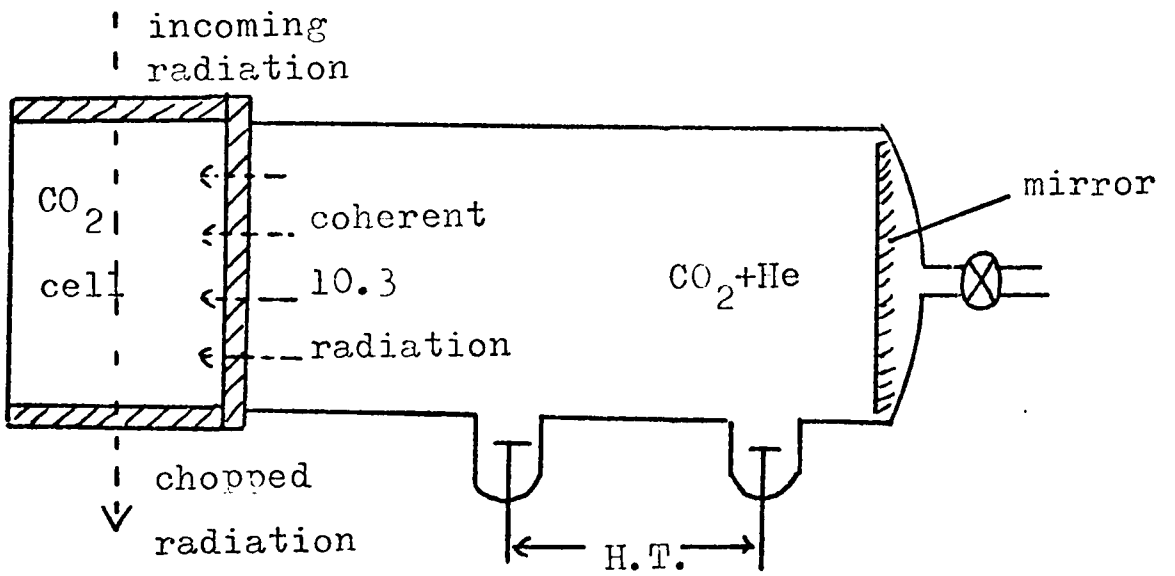
5.1. Design.

The most important feature of the new instrument is the pressure modulator. A design was sought which could produce a good pressure swing while retaining a modest power consumption, and which would not risk contamination of the CO_2 gas in the cell. The latter point is critical because of the low mean pressures involved and the long periods over which they would have to be maintained, and excludes methods which require motors, coils, electronic components and the like to be in contact with the gas. Some of the ideas which were considered are shown in fig. 5.1. That which was finally adopted appears in fig. 5.2. This uses an oscillating steel ball bearing magnetically driven inside a closely matched precision bore glass tube. In this way a very high standard of cleanliness is possible, and by tuning the driving voltage to the resonance frequency of the ball a suitable amplitude was obtained. The frequency at which the resonance occurred was principally determined by the mass of the ball and the strength of the annular permanent magnet which suspended it, and was chosen to be in the region of 10 c/s, which represents a compromise between the amplitude of oscillation and the efficiency of the electronics, both of which improve with frequency in opposite directions. The amplitude of the ball could be measured using a travelling microscope in conjunction with a stroboscope, enabling the compression ratio $\Delta p_c / p_{c_0}$ to be calculated but without allowance for the reduction in Δp_c caused by leakage of gas past the ball.

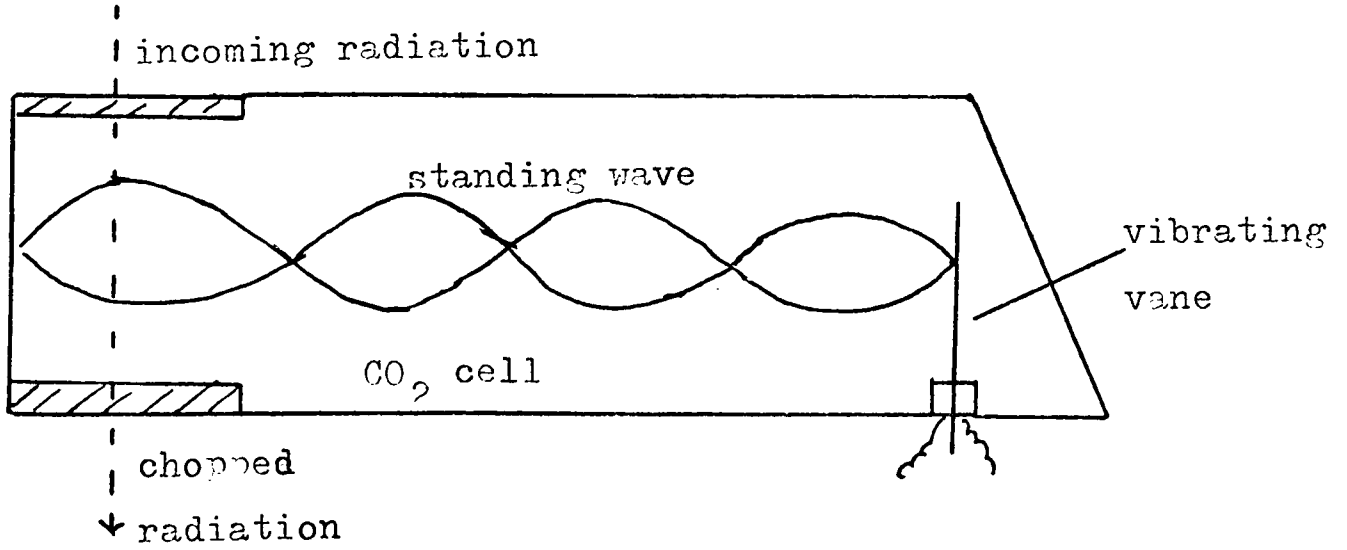
The optical system is also shown in fig. 5.2. The source was a blackened copper cone, the temperature of which could be regulated between 200°K and 400°K by cooling with liquid nitrogen or heating with a resistance coil and which was measured to within 1°K by a copper-constantan thermocouple. Radiation from the source passed through the sapphire windows of the chopping cell and was condensed onto the detector by a Newtonian arrangement of mirrors, which also defined the field of view so that only the black body was seen by the detector. The detector itself was a photoconductive indium antimonide cell (Mullard RPY 36), cooled by liquid nitrogen. Its spectral



(a) Motor driven piston type.



(b) Pulsed CO_2 laser type.



(c) Standing wave tube type.

Fig. 5.1. Some ideas for pressure modulators.

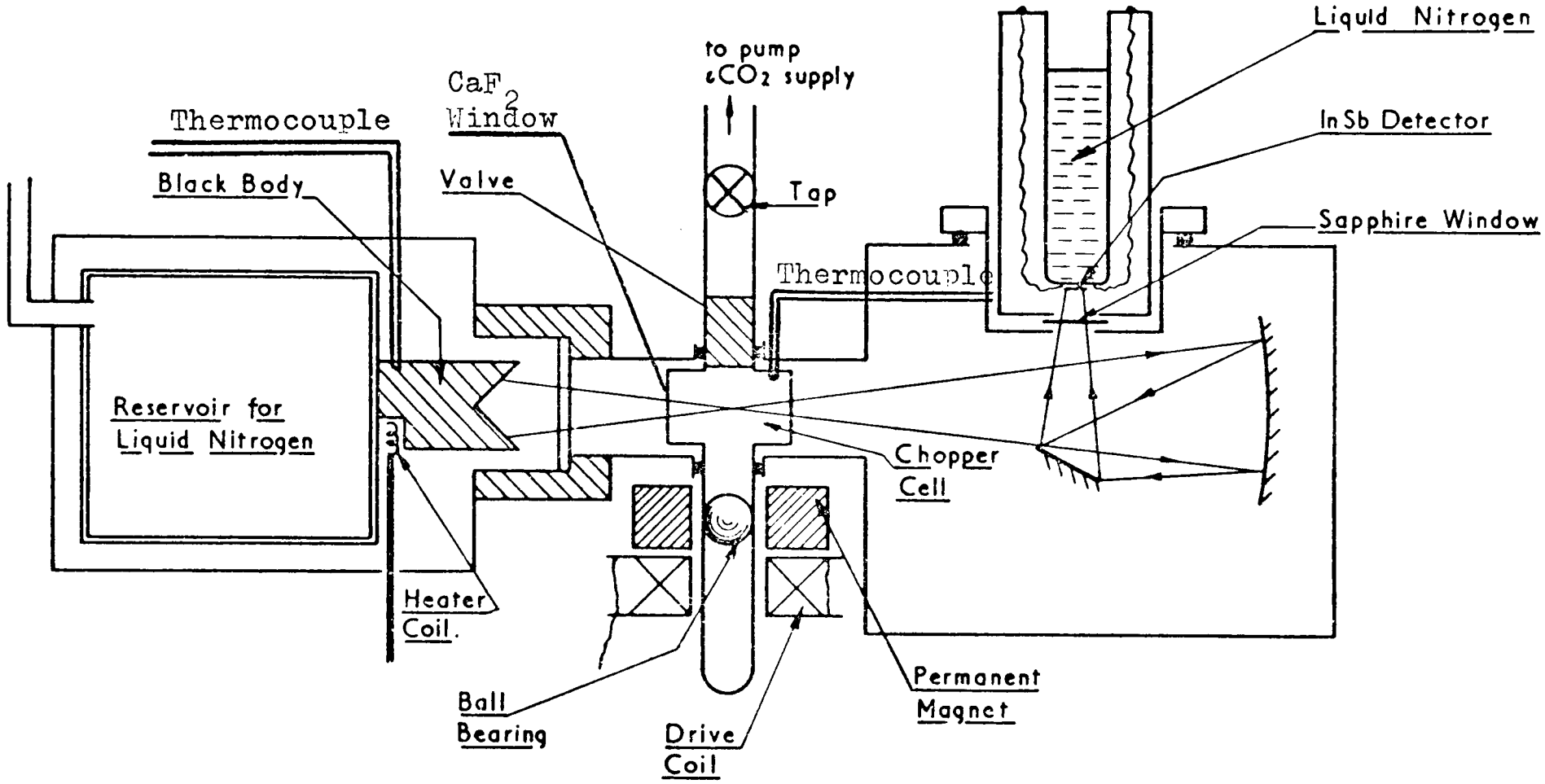


Fig. 5.2. Schematic diagram of the 4.3μ Radiometer.

response is shown in fig. 5.3. A narrow band filter (3.70μ- 4.93μ) was included to remove chopped radiation from water-vapour and other bands of CO_2, which would have confused the interpretation of the readings. The presence of spurious signals due to electromagnetic pick-up in the electronics was detected by admitting a large amount of pure CO_2 to the normally evacuated chamber containing the mirrors; this had the effect of absorbing virtually all of the true signal, exposing the unwanted part. The soft-iron screening around the detector was improved until all of the pick-up was eliminated.

Fig. 4 shows a block diagram of the electronics. A number of different coil configurations and permanent magnet strengths were tried until an amplitude of 1½ cms. was obtained at 10 c/s for a power consumption of 200 mW. A portion of the driving voltage was tapped off to provide a reference for a phase sensitive detector, which provided a d.c. voltage in the range 0 - 10 mV proportional to the signal strength at the reference frequency, integrated with a 5-second time constant. The p.s.d. output was recorded on a pen recorder, and the noise level estimated from the trace.

5.2. Results

Fig. 5.7 shows how the signal to noise ratio at the output varied with the temperature of the black body source. For a source temperature 20°C higher than that of the cell, the S/N ratio was 3.5, corresponding to a temperature discrimination of 6°C. Thie was smaller by a factor of about 6 than that predicted by inserting the correct values of A (4 mm.^{2}), Ω (0.03 steradians), $\bar{\tau}$ (0.75), ℓ (1 cm.) Δp_c (1 mb.) and Δf (1/30 sec.$^{-1}$) in equation (4.18), which gives S/N = 20 for ΔT = 20°C, but with an uncertainty of $\pm$ 30% due to the difficulty in estimating Δp_r accurately. For the pressure modulator to work properly, friction between the ball and the tube had to be eliminated by carefully selecting the bore size so that the ball rode on a gas cushion. The resultant leakage reduces the effective pressure modulation to something less than that calculated simply from

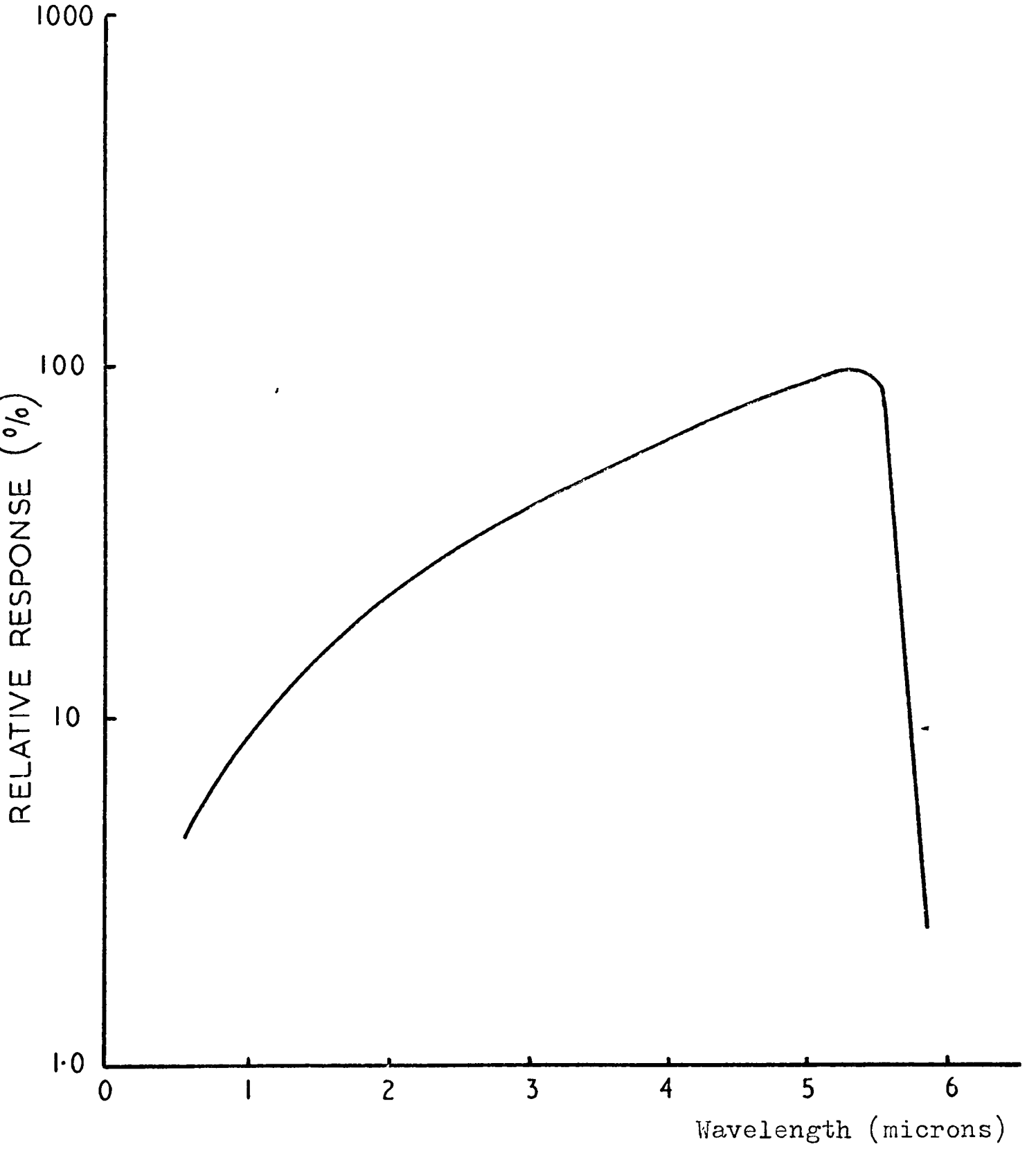


Fig. 5.3. Spectral Response Curve for InSb Detector.

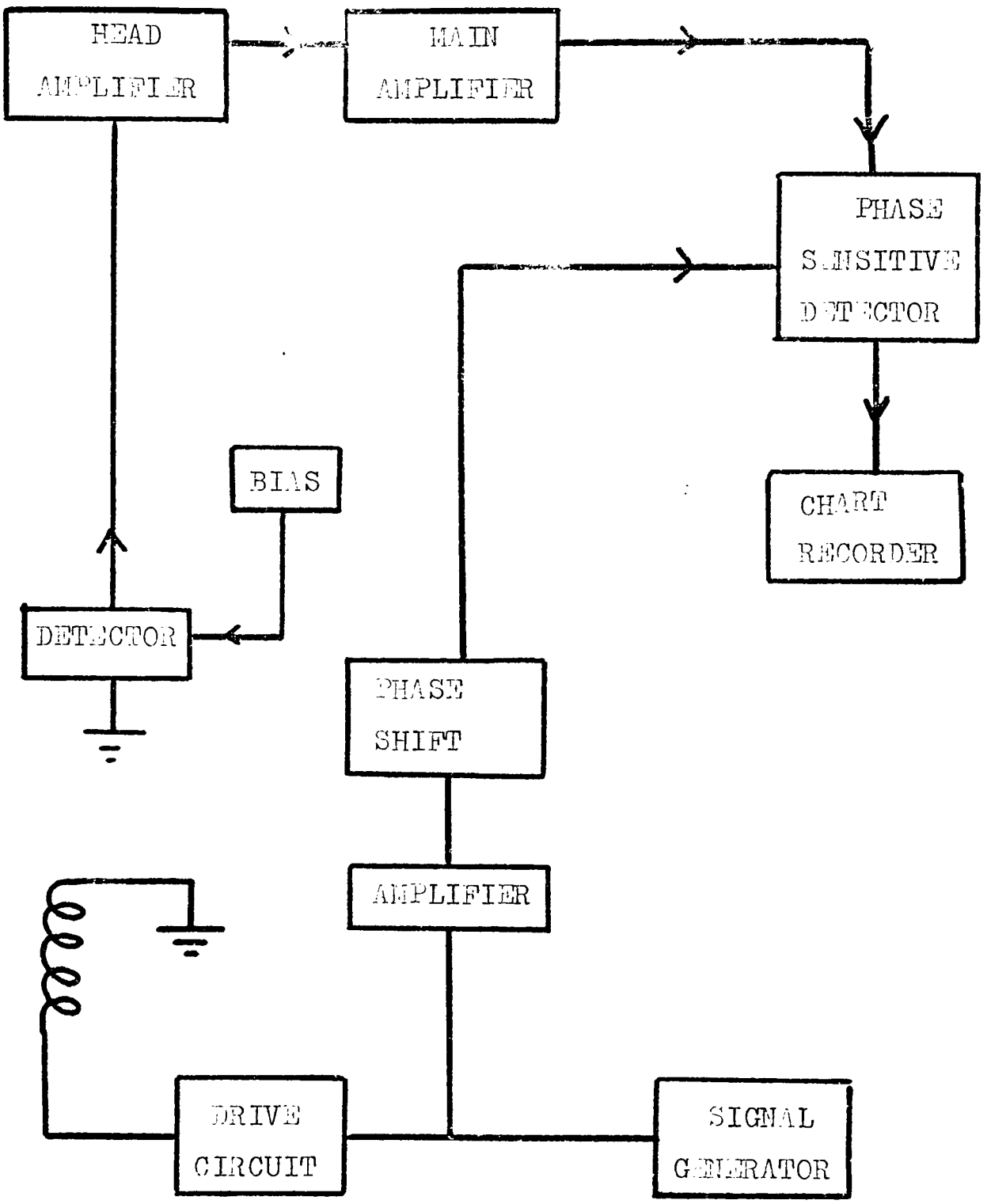


Fig. 5.4. Electronics for the 4.3 μ band radiometer.

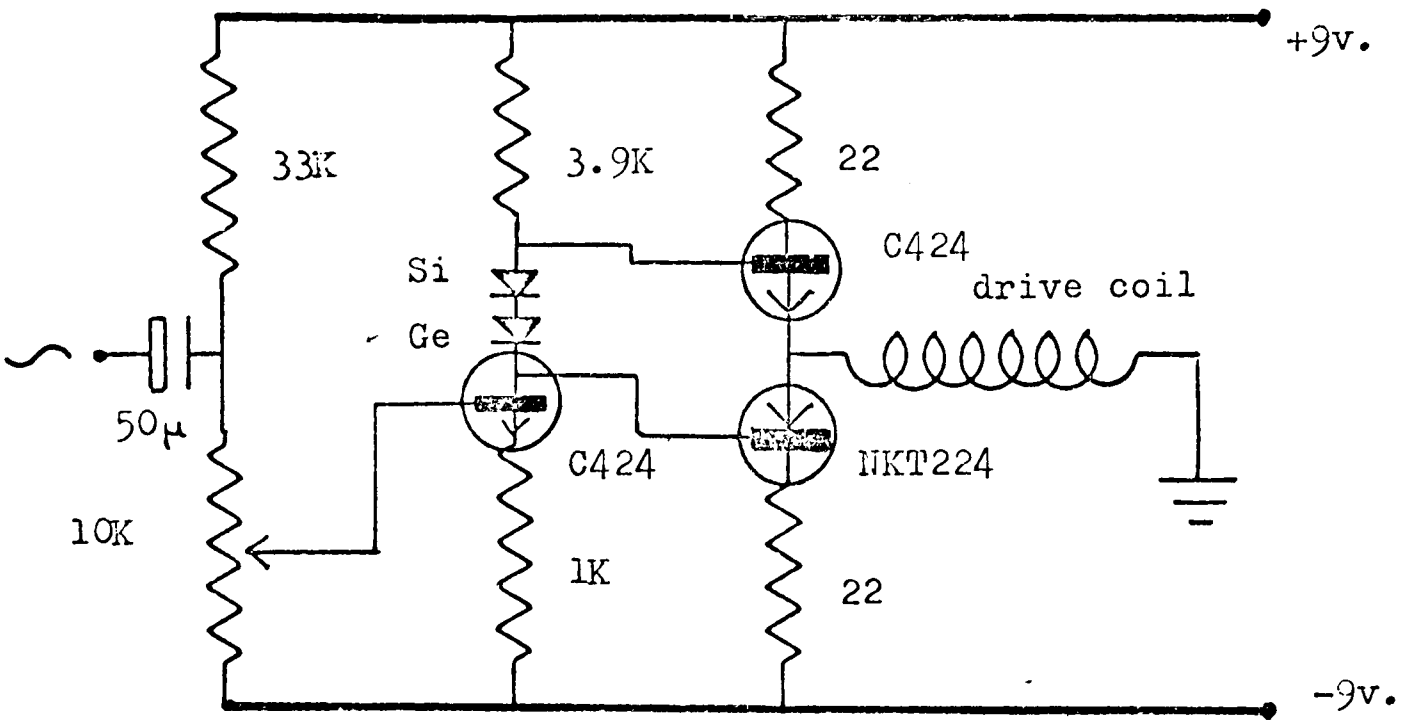


Fig. 5.5. Driving circuit.

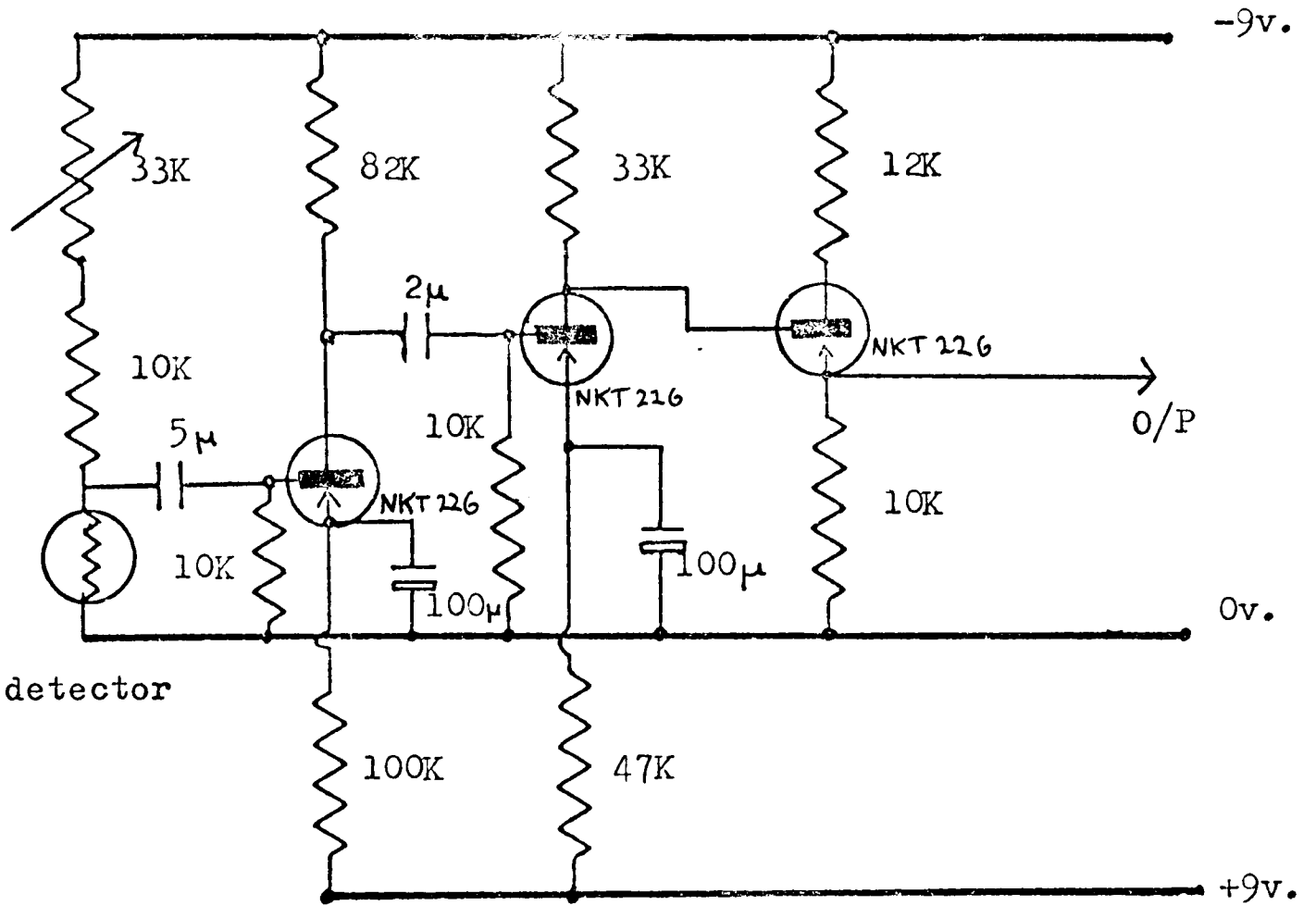


Fig. 5.6. Detector head amplifier. All resistors are wirewound.

The detector bias current is adjusted by the 33K pot. to •5 mA.

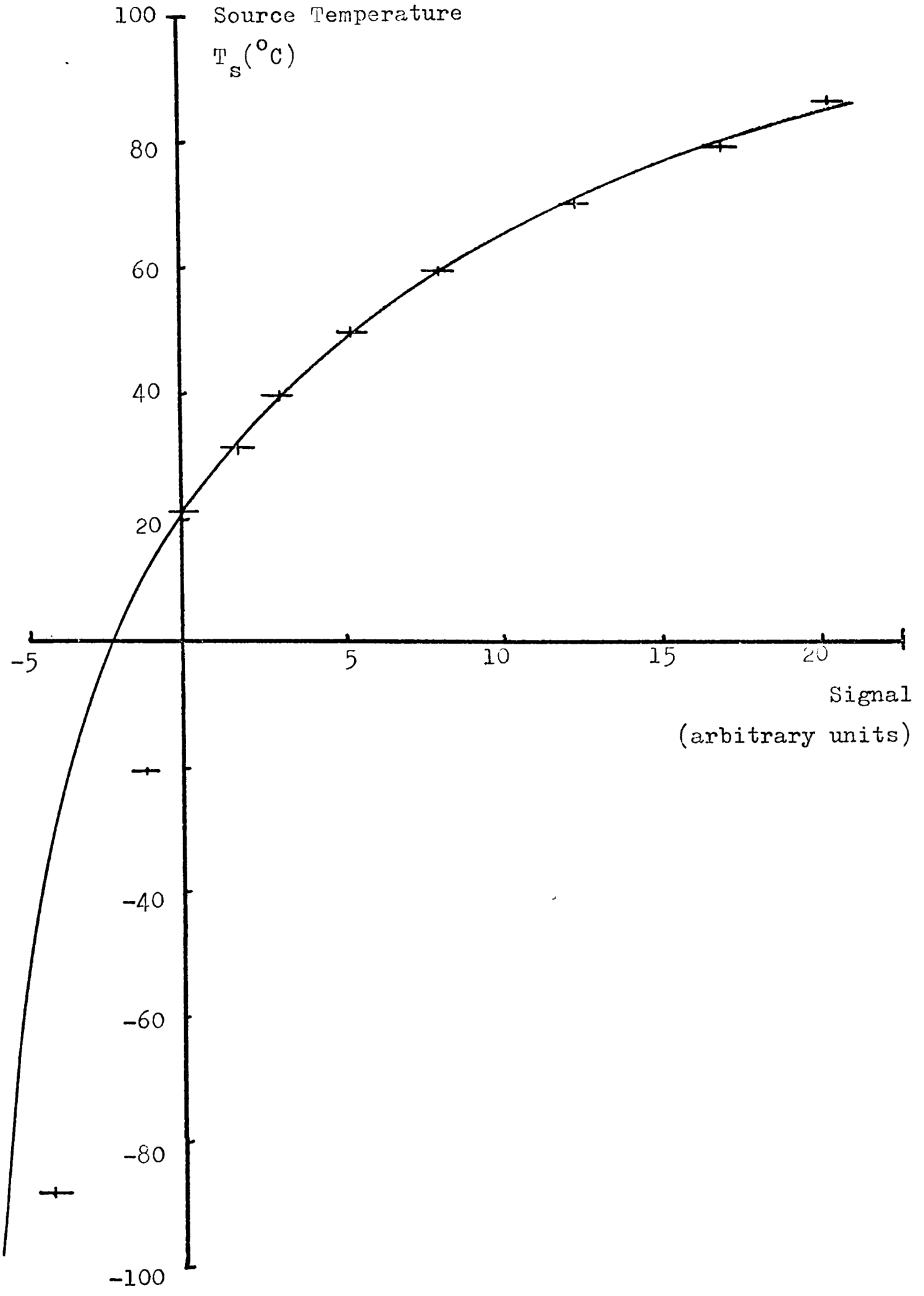


Fig 5.7. Experimental results from the 4.3μ band radiometer. The error bars denote the noise on each measurement. The solid curve is the function B(T) at 4.3μ fitted to the point at 23^oC.

Boyle's law. The loss was estimated at 30% from an elementary kinetic theory calculation assuming a uniform annular gap, leading to the corrected figure for Δp_c of 1 mb. which was used in the calculation. In fact, it became apparent that the ball was adopting a rolling mode along one wall of the tube, resulting in a crescent-shaped gap which would lead to a higher rate of leakage. Notwithstanding this, most of the discrepancy between the experimental and theoretical figures was accounted for by a measurement of the detector noise equivalent power, which turned out to be five times worse than the manufacturer's figure. This was apparently because the latter was made at a frequency of 800 c/s, whereas the radiometer chopper worked at 10 c/s, a frequency too low for 1/f noise to be disregarded.

5.3. Further Development.

Three main problems were outstanding at the time work on the 4.3 μ band radiometer was discontinued.

1. The S/N ratio was too small. Improved optics with an increased field of view, and a larger pressure modulator were designed to try to give a useful performance.

2. There was a tendency for the ball to seize in the tube due to their unmatched temperature coefficients. It was planned to replace the ball with a small magnet set in a PTFE slug to prevent this, and also to reduce leakage.

3. The system was fallible under the effects of drifts in the oscillator frequency or in the resonance frequency of the pressure modulator. Q for the latter was very high and unless the frequencies were perfectly matched the amplitude of the ball was very small. A feed-back system was clearly needed. The first one tried used two coils, one of which picked up an induced voltage from the magnetic moment of the ball, so that this could be amplified and fed to the second coil, which provided the drive. Unfortunately the two coils tended to lock on to each other, with a frequency determined

by their mutual inductance, ignoring the ball altogether. A different approach was then considered, using a piezo-electric pressure transducer mounted on a flexible disphragm in one wall of the gas cell to generate the signal for the drive coil.

While these modifications were in progress, a much more grave problem came to light. This is the subject of the next chapter.

Chapter 6. The Radiative Relaxation Problem.

It was shown in chapter 3 that the energy received by a downward-looking radiometer in or above the atmosphere is a weighted mean of the black body emission as given by Planck's formula, and that this fact enables an equivalent temperature to be determined from the flux measurements. The derivation in chapter 3 rested on the assumption that the atmosphere is in local thermodynamic equilibrium at all levels of interest, that is, that a Boltzmann distribution of molecules exists among the vibrational and rotational energy levels. Without this assumption, the equation for the energy flux at the radiometer (3.8) becomes

$$F_\nu = \int_0^\infty J_\nu \frac{d\tau_\nu}{dz}\, dz \qquad (6.1)$$

where the Planck function $B_\nu(T)$ has been replaced by some other source function $J_\nu(T)$. This would have serious consequences for a temperature sounding instrument, since $B_\nu(T)$ is a known function of temperature but $J_\nu(T)$ is not.

Curtis and Goody (1956) derived an expression for $J_\nu(T)$ at a level where the number density of emitting molecules is N:

$$J_\nu(T) = B_\nu(T) \quad \frac{\Theta + \lambda X}{\Theta + \lambda} \qquad (6.2)$$

where Θ = radiative lifetime of the vibrational state

λ = collisional relaxation time for the vibrational mode

$$\chi = \int_{band} \int_{0}^{4\pi} N k_\nu I_\nu \, d\Omega \, d\nu \Big/ \int_{band} \int_{0}^{4\pi} N k_\nu B_\nu \, d\Omega \, d\nu$$

λ is inversely proportional to the collision frequency and hence to the pressure. At low levels in the atmosphere, $\Theta \gg \lambda$ and $J_\nu = B_\nu$. At some sufficiently high level, Θ will be negligible by comparison with λ and $J_\nu = I_\nu$. This means that all incoming radiation is simply scattered, none of it being converted to translational energy prior to reradiation. At intermediate levels a fraction $\frac{\Theta + \lambda\chi}{\Theta + \lambda}$ of the molecules will lose the energy gained by absorption of a photon by collision with other molecules; the remainder will re-radiate before a collision has time to occur.

The relaxation times Θ and λ are not known well enough for 6.2 to be used in the temperature sounding experiment. Curtis and Goody used $\Theta = 0.43$ sec. and $\lambda = 15 \times 10^{-6}$ sec. at 220°K and 1 atmosphere for the 15μ band of CO_2, for which they found that the vibrational relaxation could be neglected for radiation to space from below 70 km. Above 70 km. B_ν and J_ν diverge rapidly (fig. 6.1).

Obtaining corresponding estimates for the 4.3μ band was more difficult, since more complex modes of decay are available. The collisional de-excitation of the ν_3 vibration can occur through a number of stages involving nitrogen, water-vapour and other atmospheric components in a way that is only partially understood at present. Measurements of the radiative relaxation time Θ at 4.3μ were being made by Alexander, Houghton and McKnight (1968) at the same time as the development of the 4.3μ band radiometer of chapter 5 was in progress. It was anticipated that the results would be similar to those quoted by Curtis and Goody for the ν_2 band, leading to a departure from LTE at about 70 km. In fact, however, Houghton (1969) summarizing all of the available results of measurements on the relaxation times concludes

that effective values for θ and λ of 2.4×10^{-3} sec. and 1.6×10^{-4} sec/atmosphere are appropriate. These lead to the equation

$$J_\nu = \frac{B_\nu}{(1 + 1.2 \times 10^{-4}/p)} \qquad (6.3)$$

so that $J_\nu = B_\nu$ only at levels below about 30 km. (fig.6.1). Although this result is approximate, and although experimental data obtained by McClatchey and Shaw (1969) failed to show any departure from LTE at altitudes up to 40 km., it is clearly no longer safe to assume that an instrument working in the 4.3μ band could make useful measurements of upper atmospheric temperatures. Houghton confirms that this restriction does not apply to the 15μ band below 80 km., in agreement with Curtis and Goody.

The interesting situation whereby the ν_2 vibration of CO_2 is in local thermodynamic equilibrium over an important section of the atmosphere while the ν_3 vibration of the same molecule is not, suggests an attractive experiment which could be performed by the modified pressure-modulated CO_2 radiometer shown schematically in fig. 6.2. A slab of magnesium oxide crystal acts as a beam splitter, reflecting radiation at 15μ and transmitting that at 4.3μ. The system is therefore effectively two radiometers, having a common field of view, cell pressure and pressure swing. The measurements at 15μ would give a profile of $B_\nu(T)$, and hence T; those at 4.3μ would give $J_\nu(T)$, from which λ could be deduced. Simultaneous measurements of λ and T would lead to interesting information on the collisional and radiative processes at work in the upper atmosphere; they would also provide the first direct investigation of the contribution of CO_2 to the heating and cooling of the Mesosphere, which is known to be important.

For temperature sounding alone, it was evidently politic to transfer attention to an instrument operating in the 15μ band.

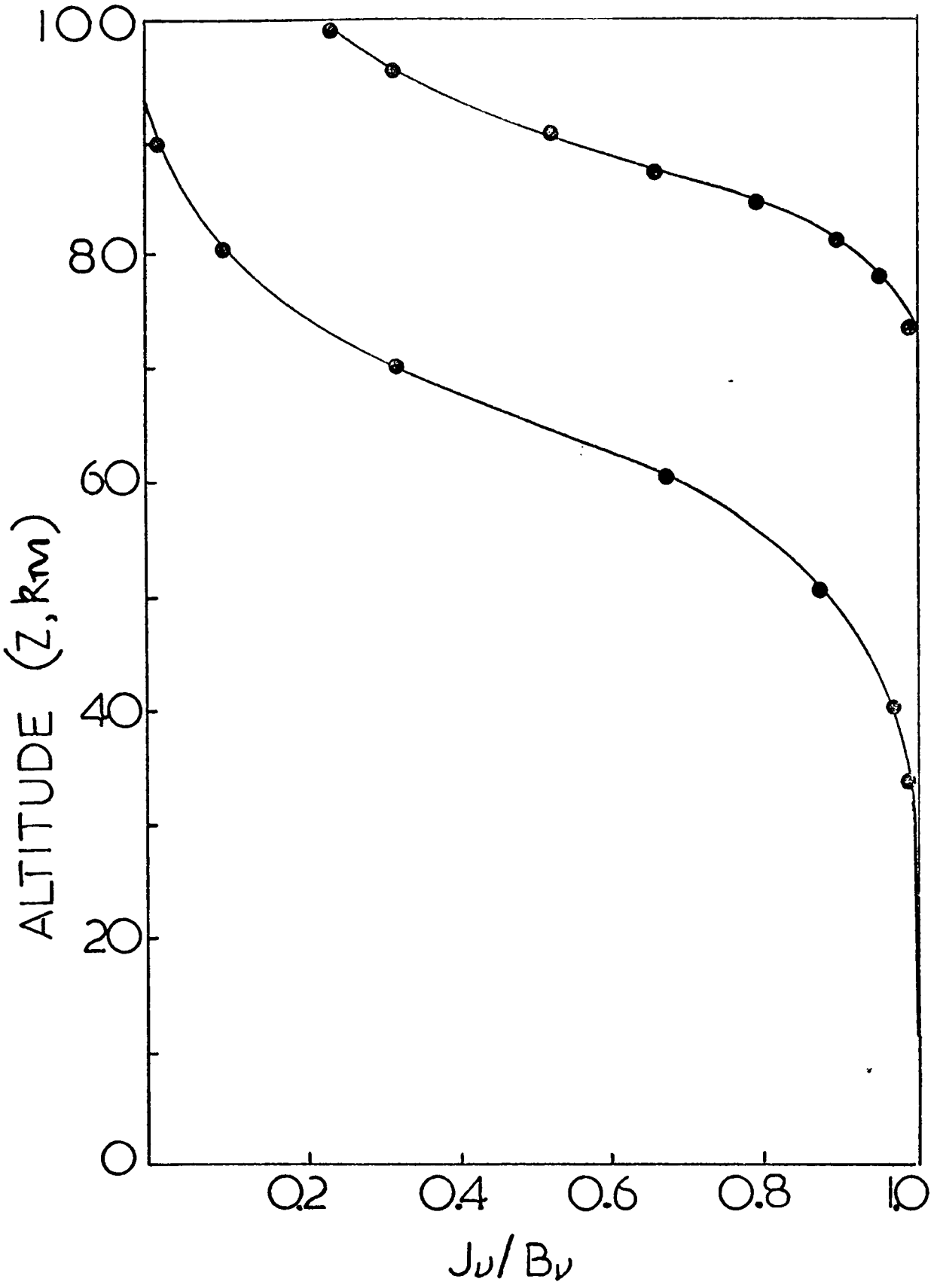


FIG. 6.1 BREAKDOWN OF L.T.E. FOR 15μ AND 4.3μ BANDS OF CO_2

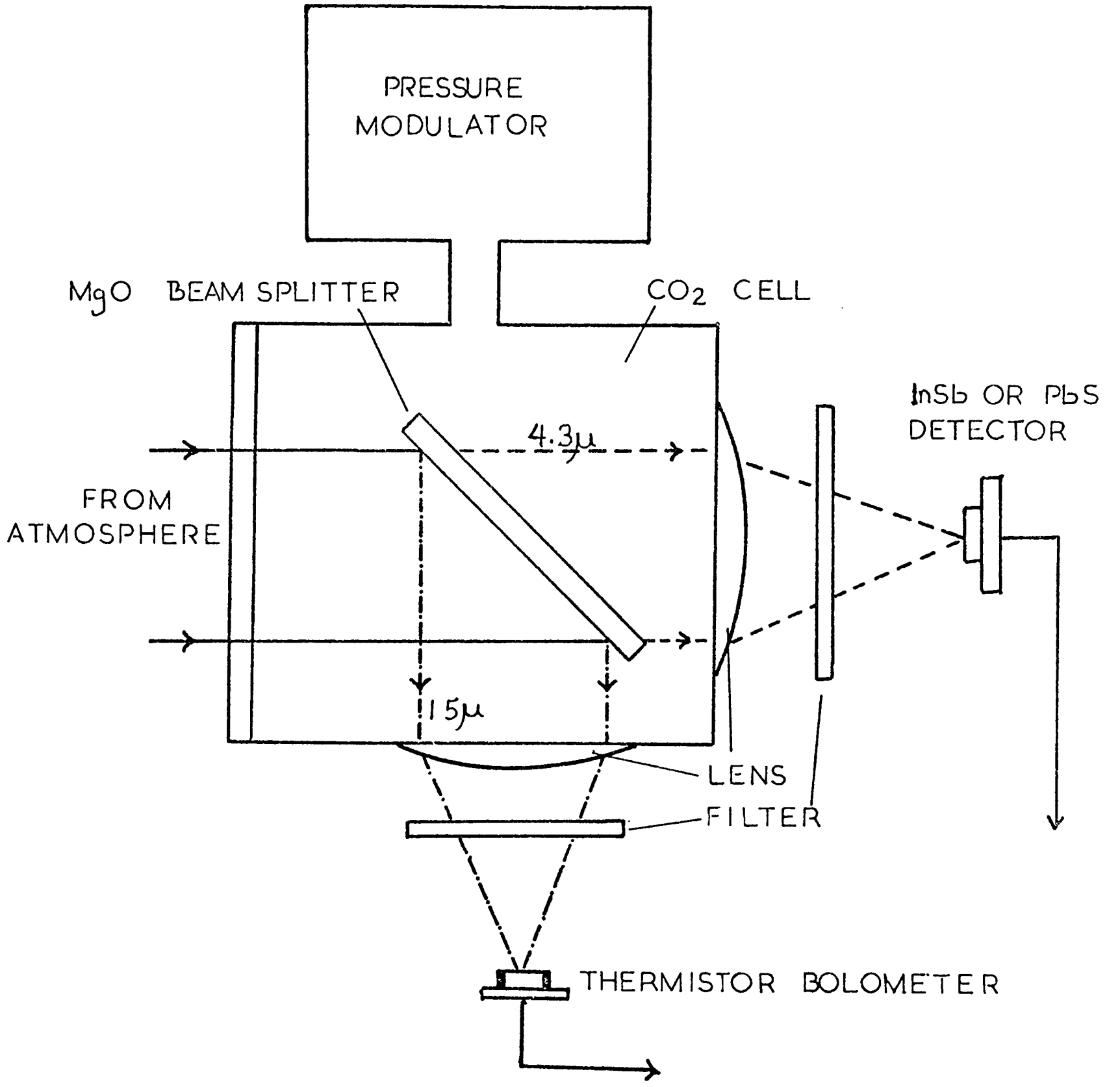


Fig. 6.2. Apparatus for studying radiative relaxation.

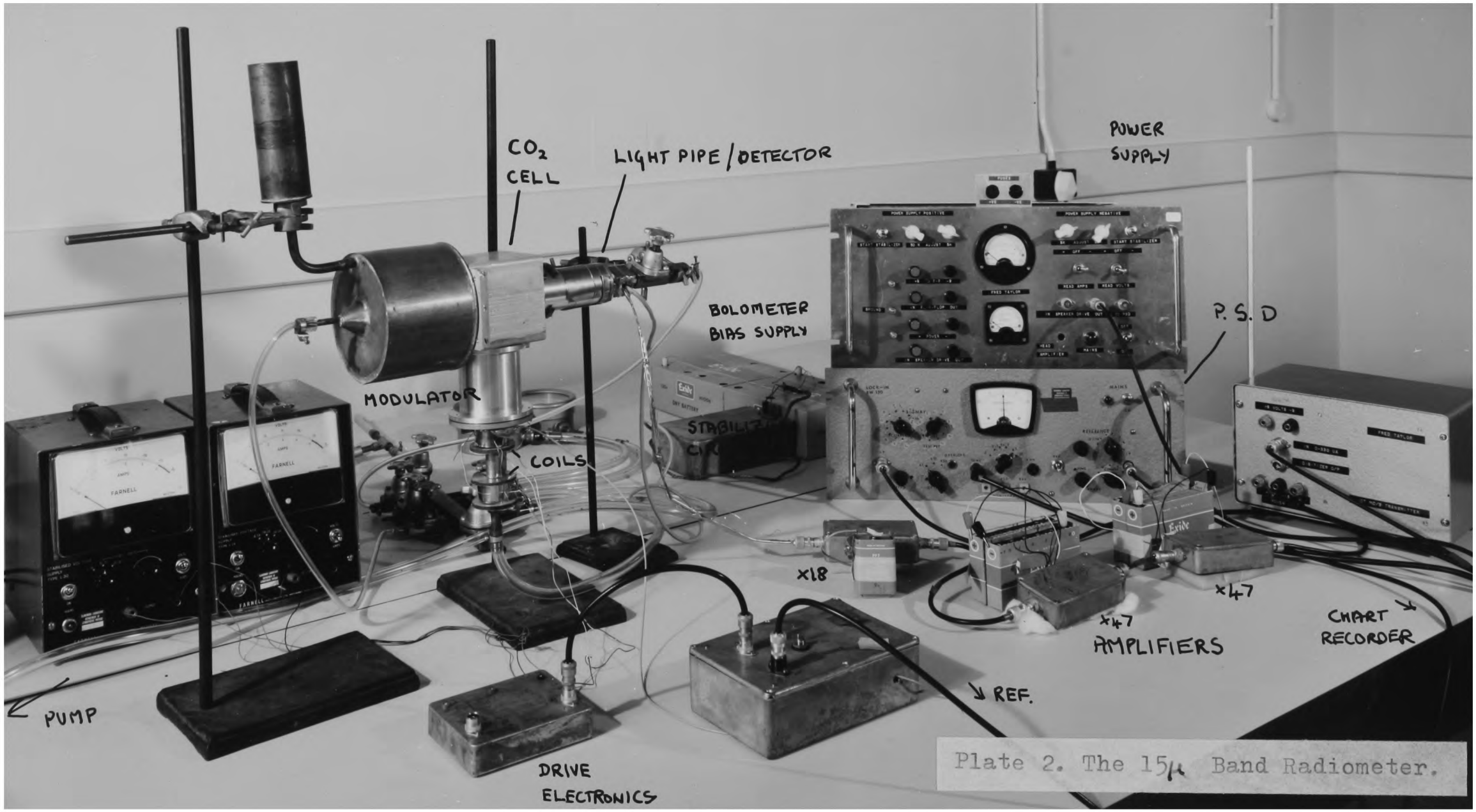


Plate 2. The 15μ Band Radiometer.

Chapter 7. The 15 -band Radiometer

The new radiometer was designed around the use of a longer absorption cell, with a piston of large area to modulate the pressure, and with a much larger radiation grasp than the 4.3μ device, resulting from the use of cone channel optics. The basic design is illustrated in fig. 7.1, and described below.

7.1. Design of the Pressure Modulator.

G. D. Peskett suggested that a light-alloy piston mounted on flat beryllium-copper spider springs and driven magnetically could run at its resonance frequency with a minimal power consumption. The idea was tried for a number of different shapes and thicknesses of spring, made from Be/Cu sheet by a photo-etching process. It was found that a piston 6 cm. across could oscillate with an amplitude of 1 cm. with a sideways movement of less than 0.002 cm. on spiders 0.012 cm. thick (fig. 2). The rate of leakage past such a piston may be estimated from the formula derived by Tao and Donovan (1955) for the flow rate through a fine annulus:

$$Q = \pi v (r_2^2 - r_1^2) = \frac{\pi \Delta p}{8 \eta l} \left[r_2^4 - r_1^4 - \frac{(r_2^2 - r_1^2)}{\log(r_2/r_1)} \right] \qquad (7.1)$$

where Q = flow rate in $cm^3 sec^{-1}$

v = mean velocity of flow of gas past piston ($cm.sec^{-1}$)

r_2 = radius of cylinder bore (cm.)

r_1 = radius of piston crown (cm.)

Δp = pressure gradient across piston (dynes cm^{-2})

η = viscosity of CO_2 (142×10^{-6} poise, assumed constant)

l = depth of piston skirt (0.35 cm.)

The last term in this expression is difficult to work out if r_1 and r_2 are nearly the same. For $(r_2 - r_1) \ll 1$ it can be shown that

$$Q = \frac{\pi \Delta p \, r_2 (r_2 - r_1)^3}{12 \eta l} \qquad (7.2)$$

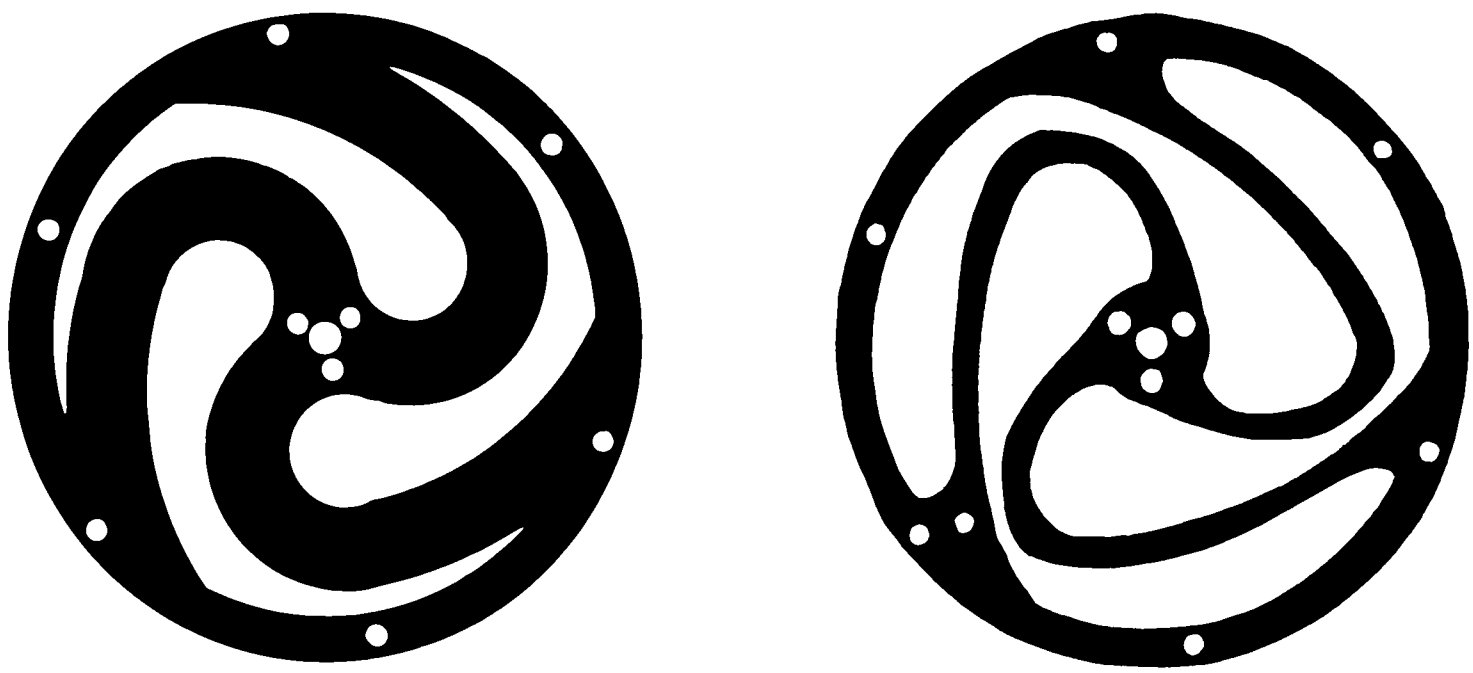


Plate 3. Evolution of the Spider Springs.

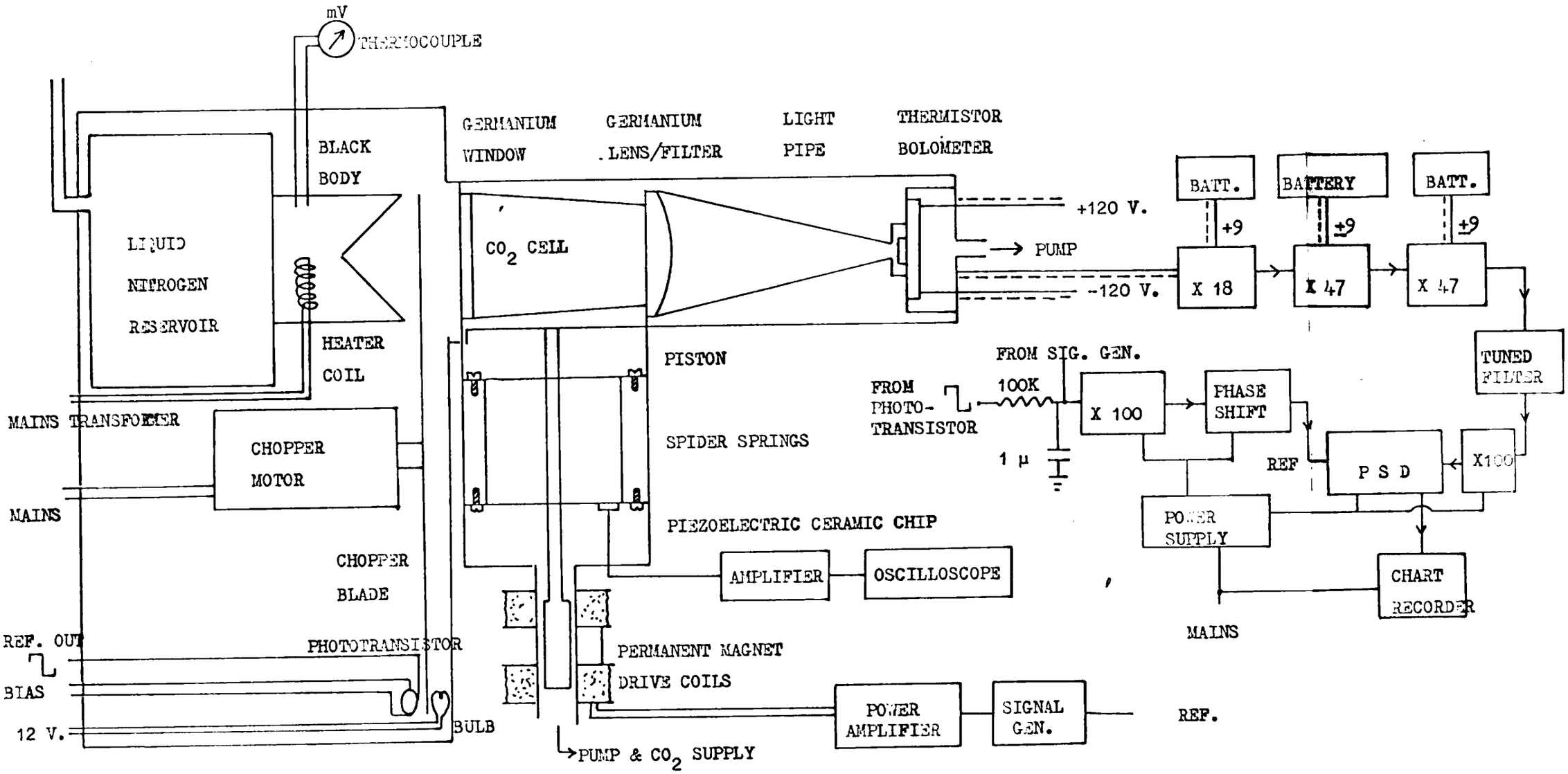


Fig. 7.1. Systems Diagram of 15μ Band Radiometer. Two means of chopping the radiation from the source are shown, a rotating chopper blade and the pressure-modulated CO_2 cell. Only one of these is used at any given time; the former is used to calibrate the latter.

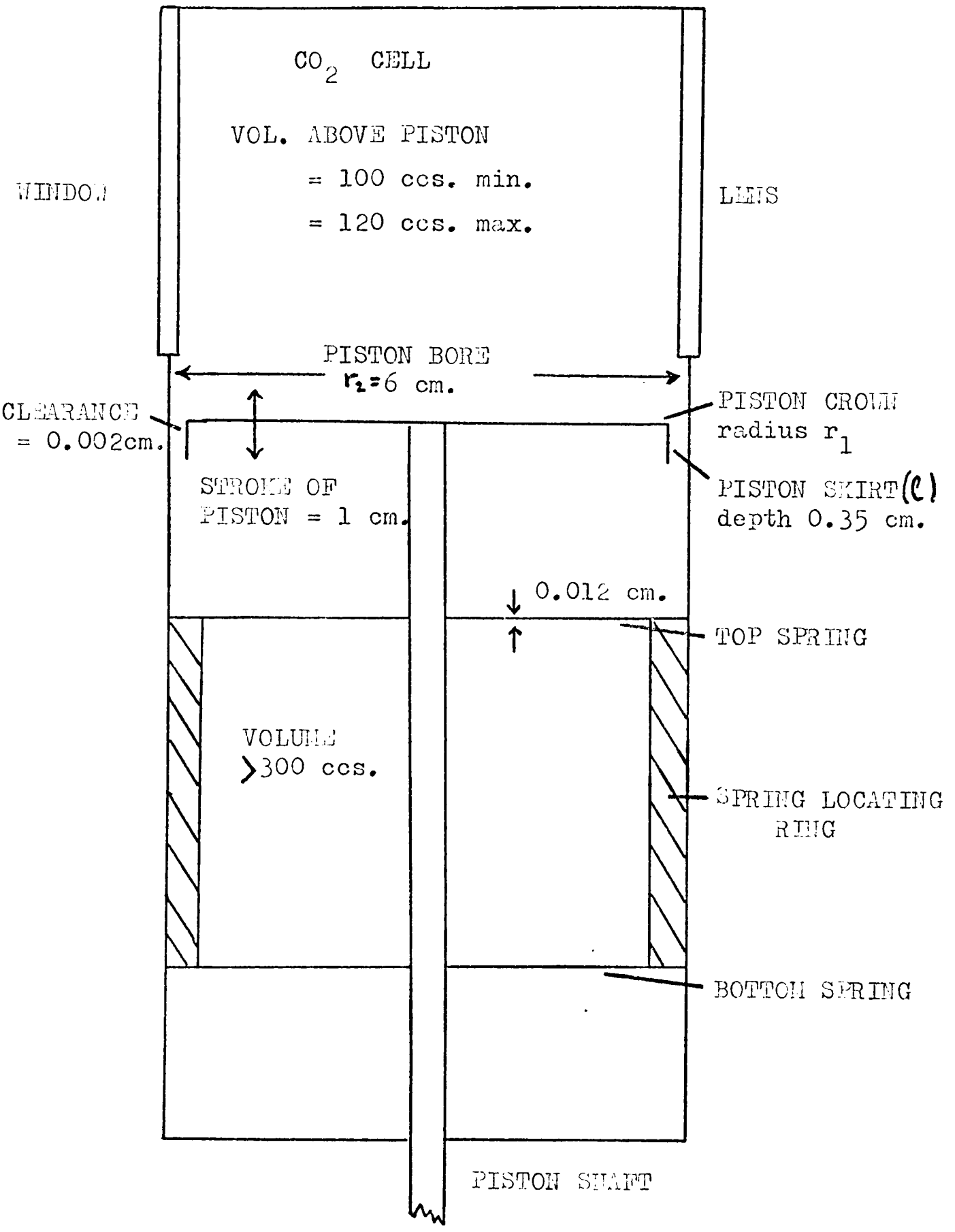


Fig. 7.2. Quantities used in the leakage rate calculation.

For a cell of volume 100 cm^3 containing CO_2 at an average pressure of 1 mb., the mean pressure gradient across the piston would be $\overline{\Delta p} = 0.1$ mb. without leakage, corresponding to a loss of pressure modulation of roughly 0.003 mb. or only 3%. A pressure swing of about 0.14 mb (14% of the mean pressure) is therefore predicted.

It is interesting to consider whether the flow down the annular gap is laminar or turbulent, particularly since 7.1 is valid only for laminar flow. Chandrasekhar (1961) states that the critical Reynold's number for this kind of flow is

$$R_{crit} = 35.94\sqrt{\frac{r_1}{r_1 - r_2}} \approx 800 \qquad (7.3)$$

The Reynold's number for the mean flow past the piston is

$$R = \frac{V_m (r_2 - r_1)\rho}{\eta} \approx 0.002$$

corresponding to laminar flow.

For a large piston amplitude, the resonance frequency ω should be low. On the other hand, if ω is too low the leakage rate rises, and the electronics are noisier. As a compromise, a frequency of between 10 and 20 c/s was aimed for. If the springs are operating in the linear region of their loading curve (fig. 7.3), then

$$\omega = \left(k/m - \left(\frac{f^*}{2m}\right)^2 \right)^{1/2} \qquad (7.4)$$

where k ($gm.sec^{-2}$) is the spring constant
m (gm.) is the mass of the moving parts
f^* ($gm.sec^{-1}$) is the frictional retarding force constant.

For a high-Q system $f^* << 2k$ so the first term in 7.4 is dominant. To keep the sideways motion of the piston under gravity to a minimum, the mass m was made as small as possible by machining a thin piston from light alloy, and using a light ceramic magnet of high coercive force. The whole assembly weighed about 15 gm. The required spring constant

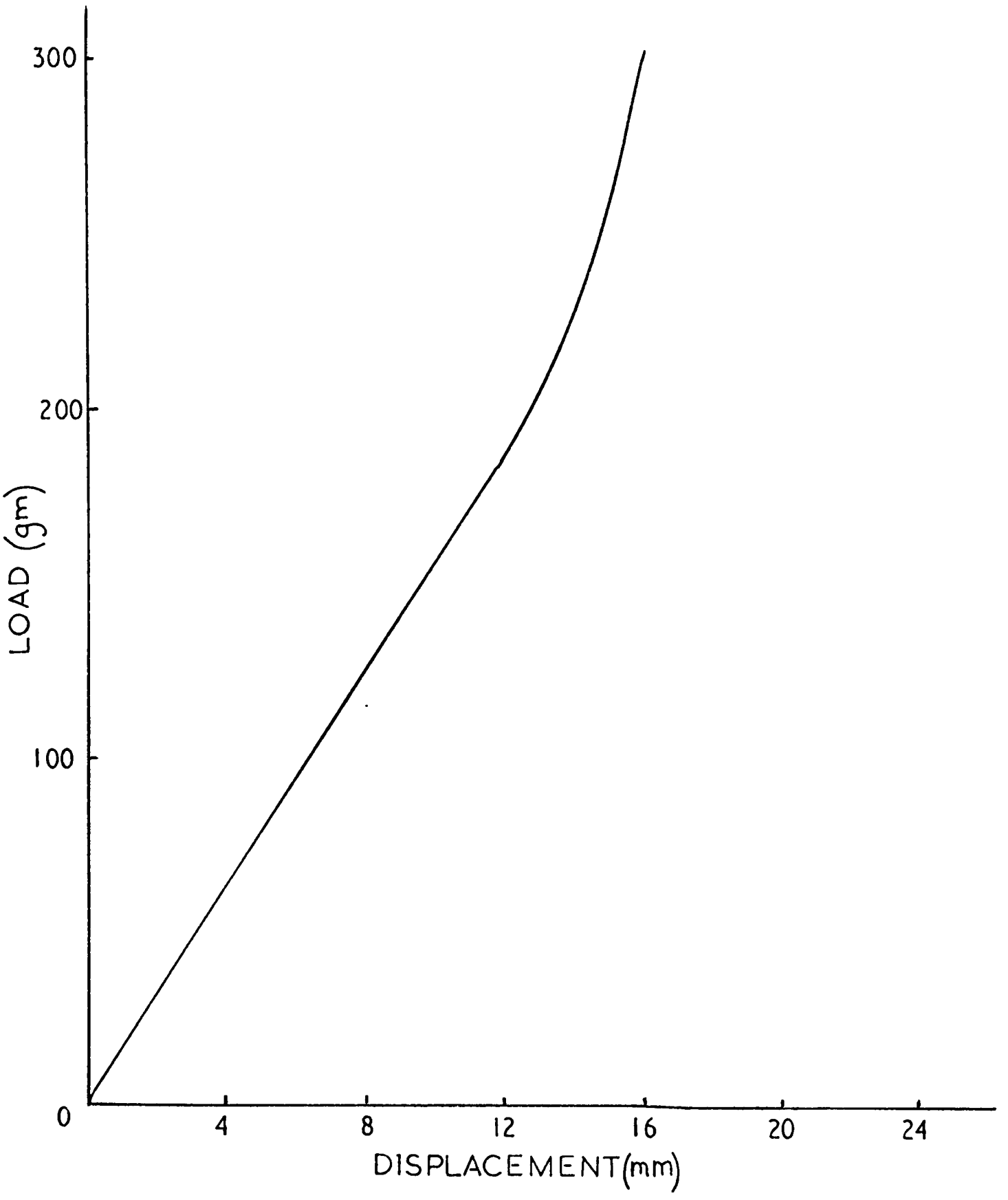


Fig. 7.3. Loading curve for the double spring system used in the final version of the pressure modulator.

for a resonance frequency of 16 c/s was then $k = 16 \times 10^4$ gm.sec^{-2}. This can be equated to the equivalent spring constant $k_{eq.}$ calculated by treating each arm of the spring as a massless cantilever of length L, with a load equal to m/6 on the free end:

$$k_{eq} = \frac{Y\, bd^3}{L^3} \qquad (7.5)$$

Y = Young's modulus for Be/Cu alloy
b = width of the arm of the spider
d = thickness " " " "
L = length " " " "

The alloy was conveniently available in sheets 0.012 cm. thick. Inserting this for d in eq. (7.5) and using $Y = 12.5 \times 10^{11}$ gm.cm^{-1}sec^{-2}, suitable values for L and b were found. The springs designed in this way turned out to be resonant at 13 c/s, which was very satisfactory.

Obtaining the desired amplitude was now simply a question of feeding in enough power to compensate for the frictional losses. The amount of power required is $\frac{1}{2\epsilon} F^* V^2$, where V is the velocity of the piston at its rest position, and is fixed for a given ω; ϵ is the efficiency of the conversion from electrical to mechanical energy, and should be maximised. The fixed coil-moving magnet arrangement has maximum efficiency when the flux linkage between the coils and the magnet is greatest. This was achieved by using a soft iron housing to give a good magnetic circuit, and by positioning the coils so that the true poles of the magnet lay at their centres. The number of turns on the coils was determined by the condition that the ratio of inductance to resistance should be as large as possible. The maximum power consumption was set at 2 watts, a reasonable value for a satellite or balloon-borne instrument. Knowlton (1964) has shown that the optimum diameter for a coil intended to produce a field in a central hole of diameter d is 3d. From data on wire thicknesses and resistivities,



Plate 4. Pressure Modulator Components.

these three conditions together led to the best coils being made from 2000 turns each of SWG 37 copper wire, with a total inductance of 120 mH. To avoid contamination of the CO_2, the coils were outside the cell, wound directly onto a thin german silver tube surrounding the magnet.

The piston amplitude was measured by noting the output voltage from a small chip of nickel-plated piezo-electric material which was soldered onto one arm of the lower spider spring. This voltage was amplified by the circuit of fig. 7.4, and was a sine wave whose peak amplitude was related to the maximum displacement of the piston. The display on an oscilloscope was calibrated by engraving a scale on the inside wall of the piston bore, and using a stroboscope tuned to the drive frequency to measure the maximum displacement. The calibration curve is fig. 7.5. The maximum amplitude of the piston was about 1.4 cm. p-p for a cell pressure of 1 mb.

7.2. Optical design.

The field of view at the entrance aperture was chosen to be 5° (0.024 steradian). For a satellite instrument at $z = 1000$ km. this corresponds to a view of a circular patch of Earth 88 km. in radius, which is about the horizontal resolution which might be required of an operational instrument. The field of view is conveniently defined by the use of a conical light pipe of high internal reflectivity, with the detector at the narrow end and a field lens at the wide end. Williamson (1952) has shown that if the focal length of the field lens is

$$f = \frac{1 \cos(\alpha_{max})}{1 - \sin(\alpha_{max})} \qquad (7.6)$$

where α_{max} is the semi-angle of acceptance and 1 is the length of the light pipe, then

$$\alpha_{max} = \sin^{-1}\left(\frac{1}{m}\right) \qquad (7.7)$$

where m is the linear demagnification. 1 was chosen to be 5 cm.,

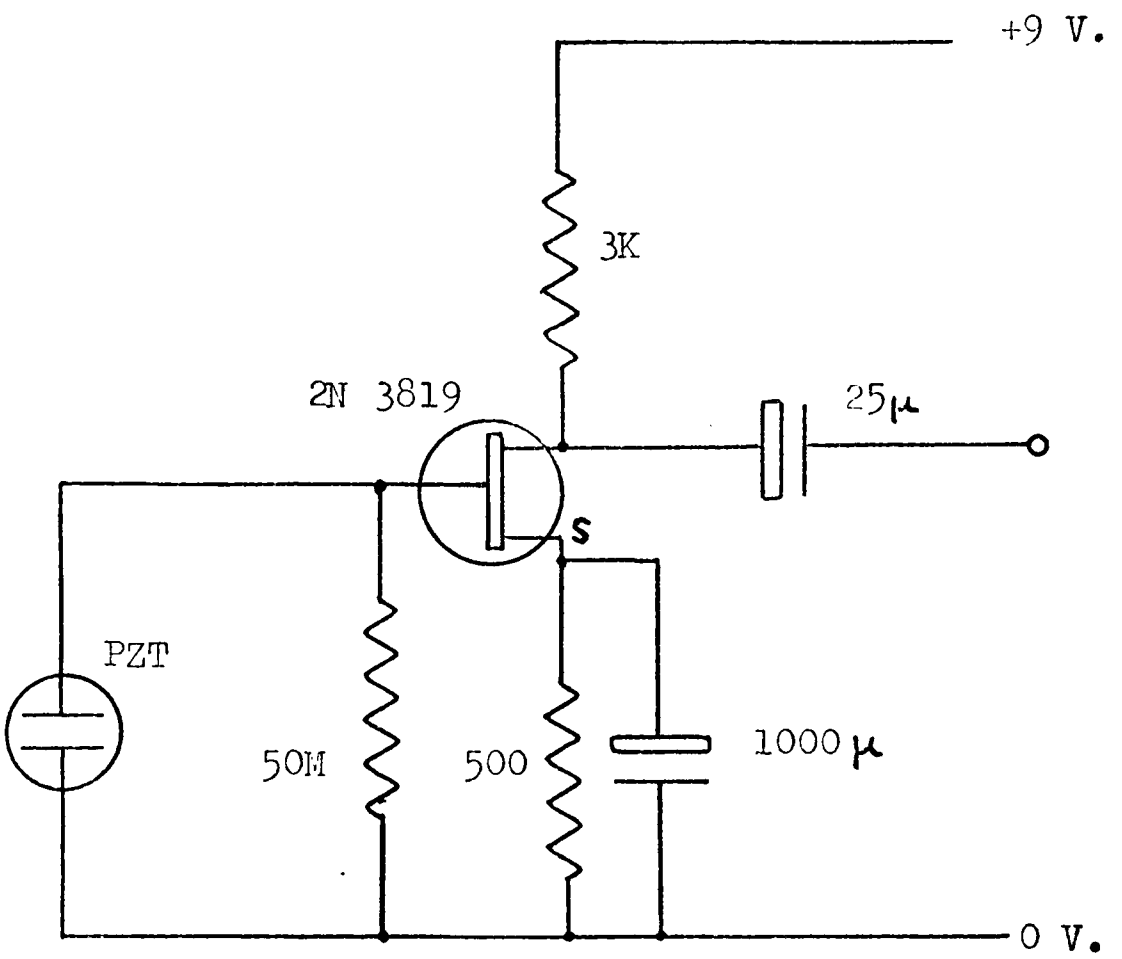


Fig. 7.4. Amplifier for PZT sensor.

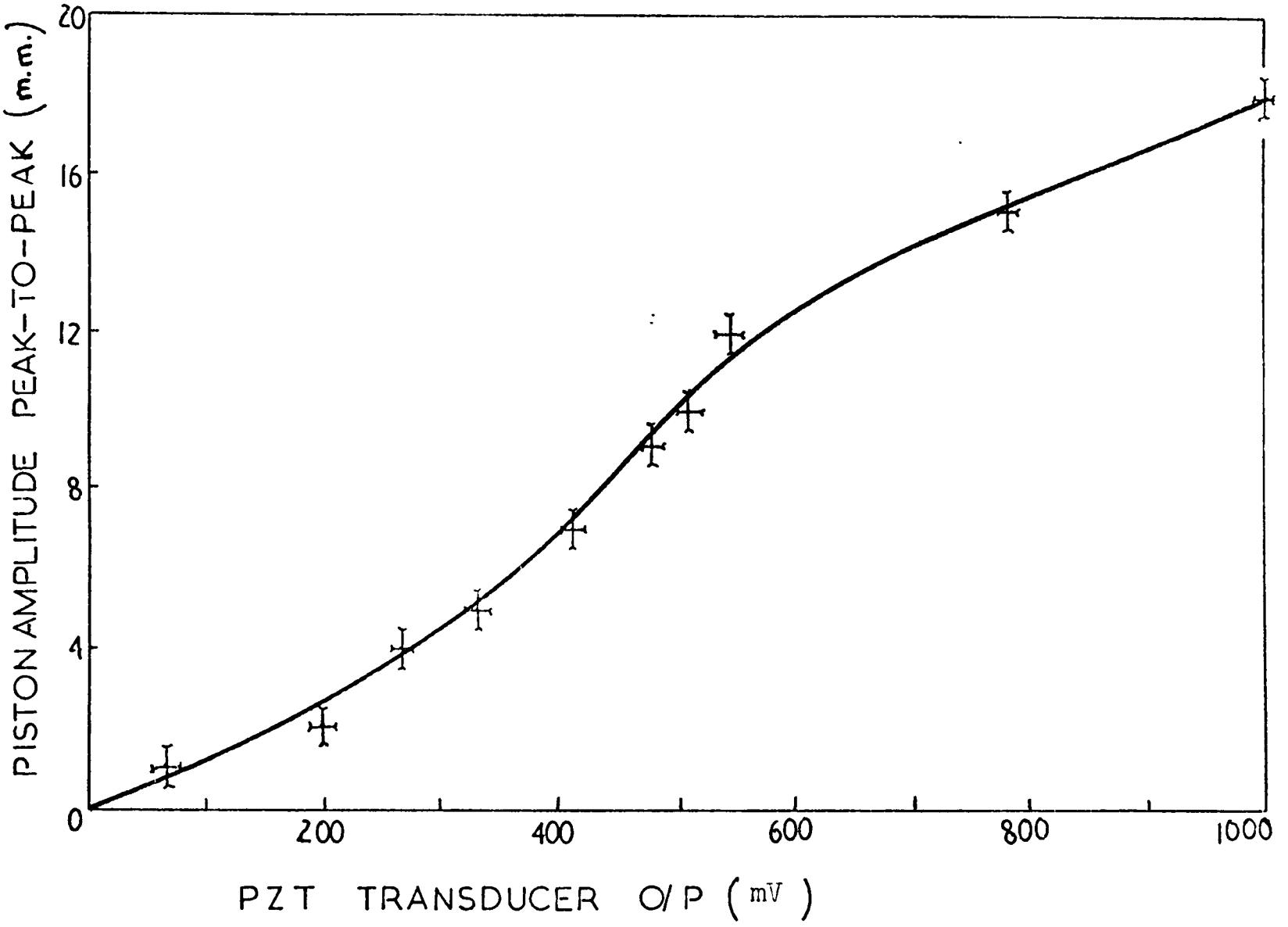


Fig. 7.5. Output of the piezoelectric sensor (after amplification by the circuit of Fig. 7.4) as a function of piston amplitude.

since this corresponds to maximum transmission in the theoretically-computed results of Abel (1966, fig. 7.6). This fixes the diameter of the lens at 3.8 cms., and the focal length at 5.5 cm. The lens was germanium, plano-convex with an interference filter deposited on the plane side. The filter was intended to exclude the other bands of CO_2 to which the detector was sensitive, and had the profile shown in fig. 7.7. The germanium window in the entrance to the chopping cell was antireflection coated for 15μ. The light pipe was machined out of brass, heavily gold-plated and polished for maximum transmission.

7.3. Detector and electronics.

The detector was a thermistor bolometer of the Barnes Engineering Co., consisting of two flakes of blackened sintered semiconductor material, each of resistance 200 K at room temperature, connected in series with bias voltages of $\pm$ 120 V. One flake is exposed to the incident radiation and, by virtue of its high negative temperature coefficient of resistance, a signal appears at the junction with the shielded flake. The time constant of this arrangement is a few milliseconds when the flakes are mounted on a brass flange, which may be conveniently bolted to the end of the light pipe, with shims between to locate the active flake less than 0.01 cm. from the end of the cone. This resulted in a very efficient and very stable optical system, capable of resisting jolts and vibration without deterioration.

Fig. 7.8 shows the detector electronics. The bias voltages were provided by 120 volt batteries, connected across large electrolytic capacitors for smoothing. The preamplifier has a low noise FET input stage, with the input impedance increased by bootstrapping via C2. Negative feedback is provided by R9, in parallel with C6; the gain of the amplifier is X18. The main amplifier which follows consists of two identical stages, of which only one is shown, having a total gain of about x 2200 and a bandwidth of 400 c/s. Both of these amplifiers were designed and built by B. J. Matley. The amplified signal was fed in to a commercial lock-in unit, consisting of further adjustable amplifiers, a filter, a phase-shifting network, and a phase sensitive

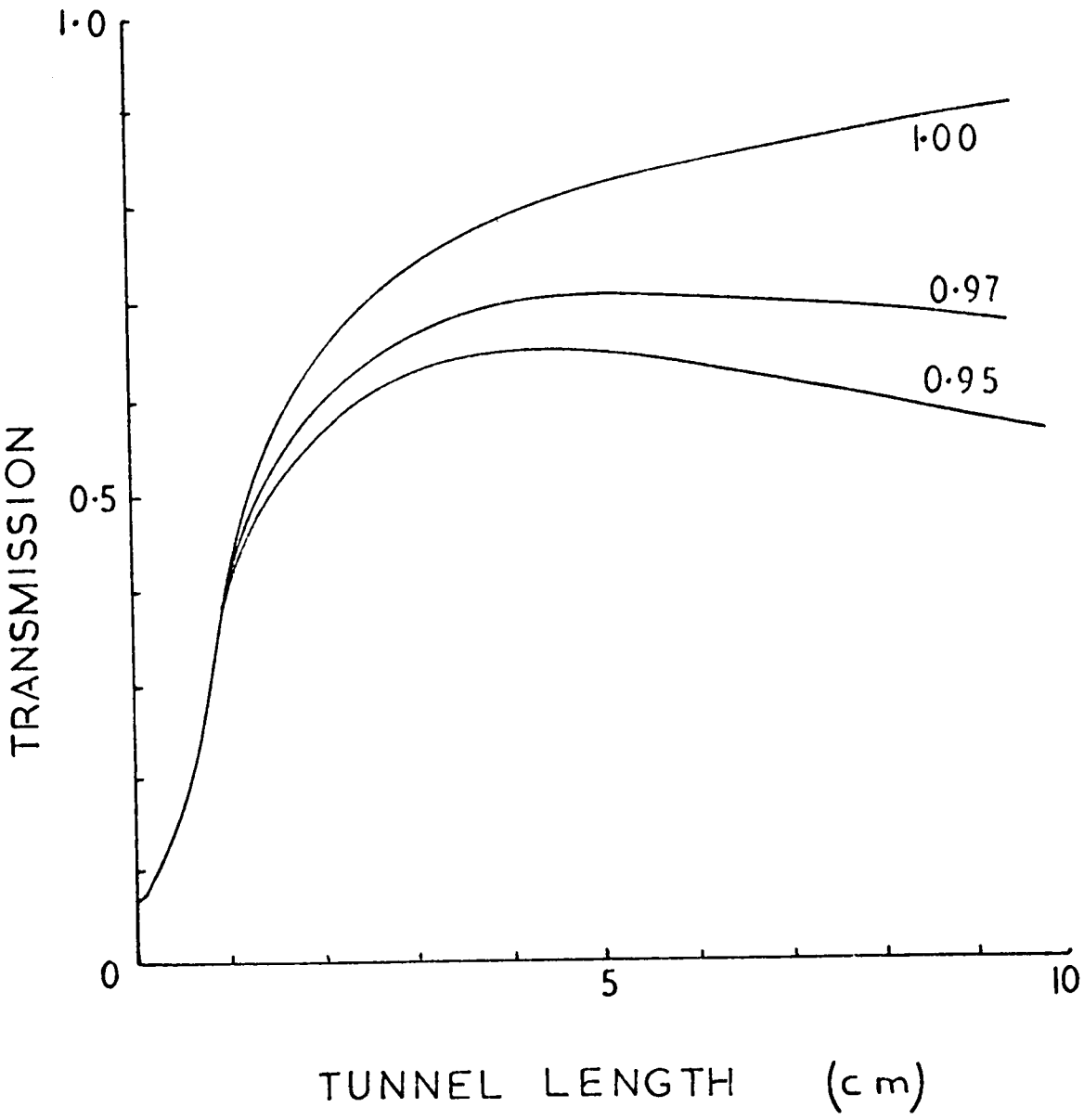
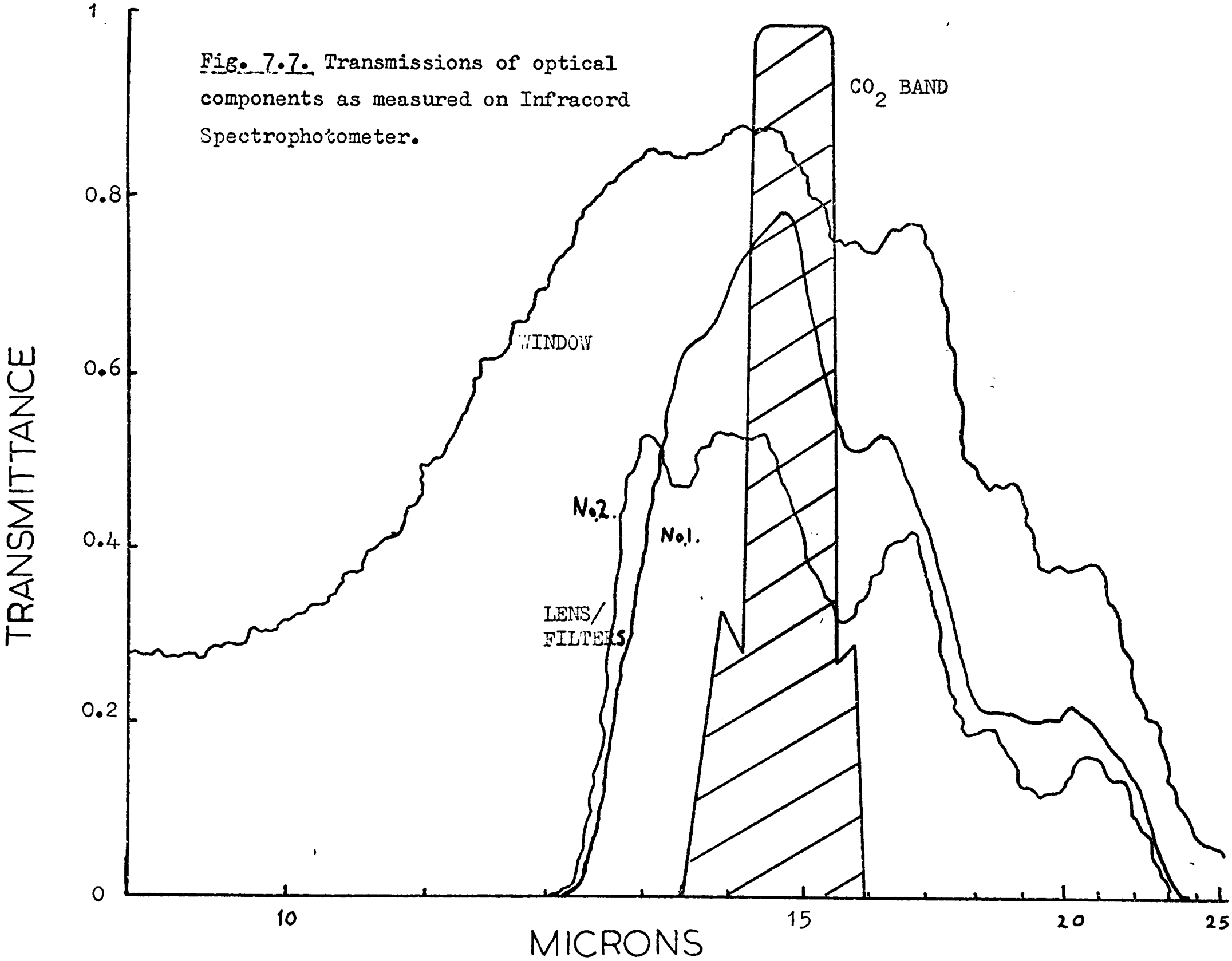


Fig. 7.6. Theoretically calculated transmissions for light pipes with a linear demagnification of 4 and the surface reflectivity given, as a function of tunnel length. (from Abel, 1966).

Fig. 7.7. Transmissions of optical components as measured on Infracord Spectrophotometer.



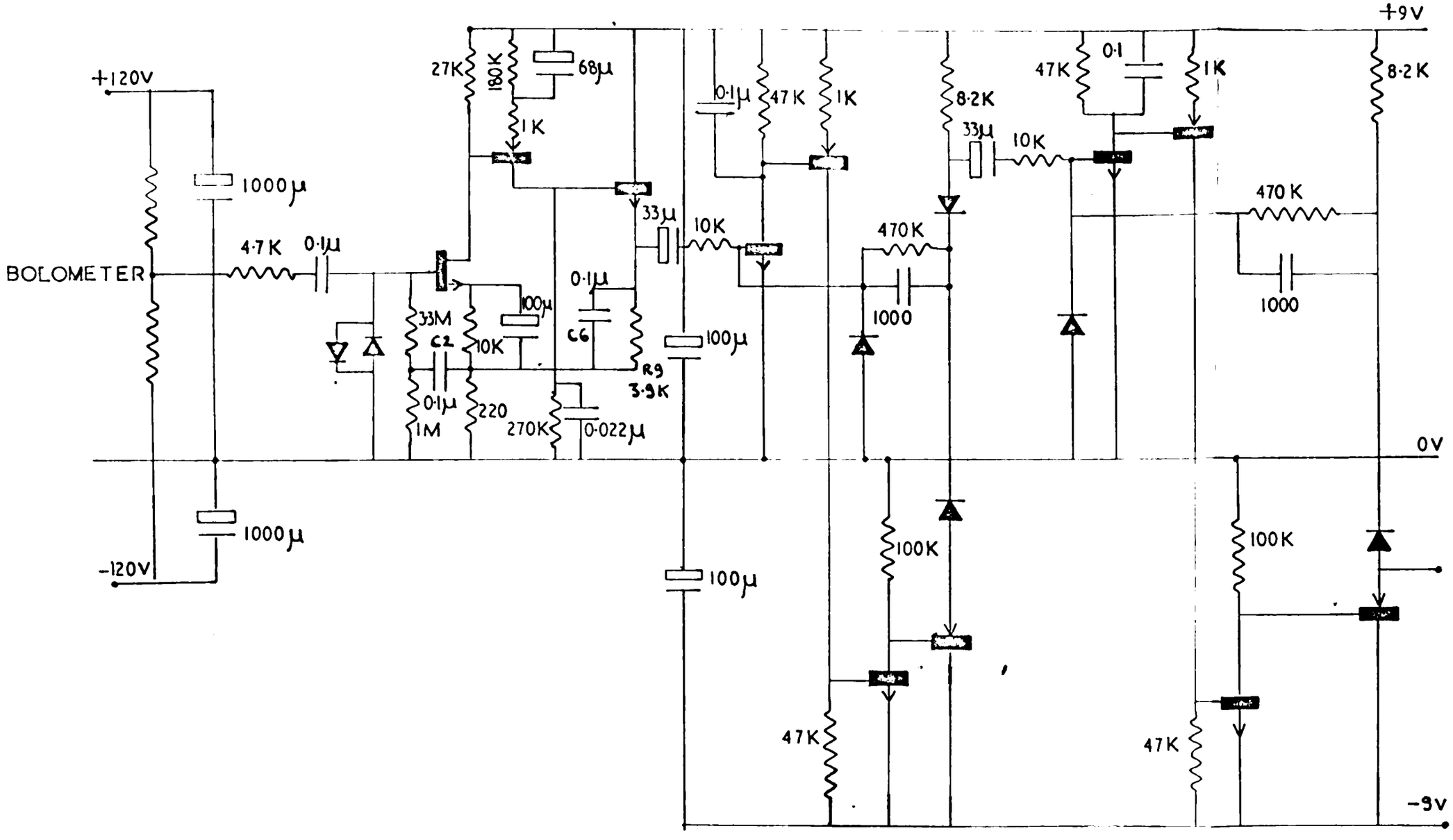


Fig. 7.8. 15µ Band Radiometer - Detector and Head Amplifier Electronics. All transistors are type BFX 37 (PNP) or 2N 2484 (NPN).

detector. The reference signal for the psd. was derived from the output of the piezo-electric element on the spring. The output was recorded on a pen recorder as before, and the noise level estimated from the trace.

7.4. Results.

7.4.1. Sensitivity.

Fig. 7.9 is a plot of the output of the radiometer as a function of source temperature. It shows that a temperature discrimination of better than $1^{o}C$ is obtained at all temperatures in the range 200-350^{o}K. These measurements were taken with a mean cell pressure of 10 mb. (equivalent to a weighting function peaked at 45 km.), and a piston amplitude of 5 mm. p-p. The sensitivity is nearly constant over the operational temperature range, because $\partial B/\partial T$ is a very weak function of T at 15μ.

The theoretical response curve may be calculated from equation 4.14 using the values

$\sum (S_i \alpha_i)^{1/2} = 40$ atmos.$^{-\frac{1}{2}}$cm.$^{-\frac{3}{2}}$ (Rodgers, 1968)

τ = 0.65 (filter, fig. 7.7) x 0.55 (light pipe, sec. 7.4.2) x 0.75 (window, fig. 7.7)

$A\Omega$ = .1 25 cm^2 steradian

Δp_c = 15 x 10^{-5} atmospheres

ℓ = 6 cm.

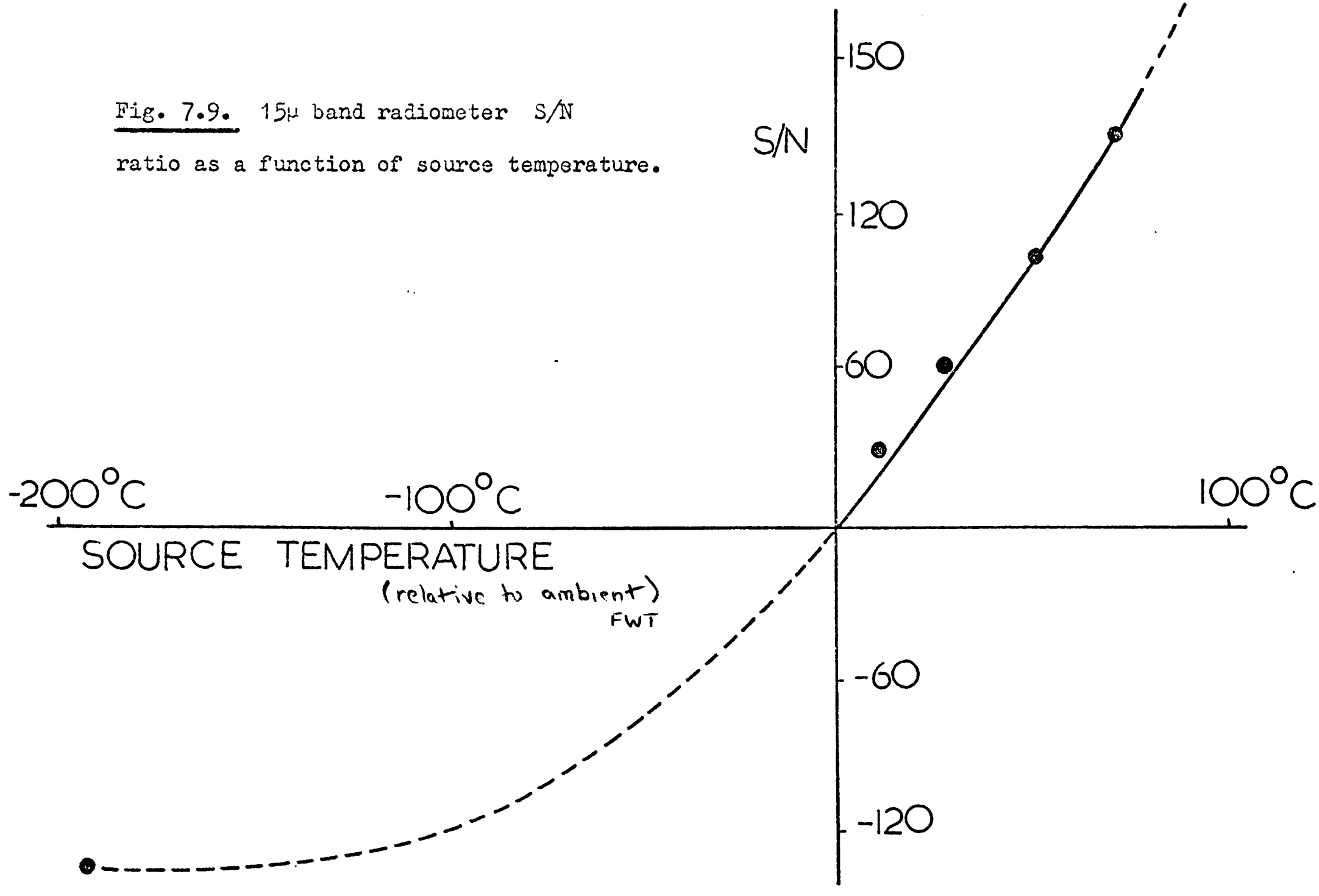
$(\Delta f)^{\frac{1}{2}}$ = $\frac{1}{4}$ sec^{-1}.

and the figure N = 2.7 x 10^{-9} watts (c/s)$^{-\frac{1}{2}}$ for the N.E.P. of the detector, which was measured in a noise-free environment. The theoretical and experimental curves are in good agreement, the small differences between the real and calculated signal to noise ratio being attributed to the strong background noise found in the laboratory, and indicate a sensitivity which is more than adequate for an operational instrument.

7.4.2. The transmission of the light pipe.

This is an important quantity, for two reasons: firstly, it enters into the theory of the performance of the radiometer, and secondly, one

Fig. 7.9. 15μ band radiometer S/N ratio as a function of source temperature.



wishes to know if it is worth expending a great deal of effort to try to improve it. There is no easy way of determining the efficiency of the light pipe. Abel (1966) prepared a laborious ray-tracing computer program to calculate it, but a number of approximations are made, and the reflectivity of the internal surface still has to be guessed. Here an attempt was made to measure the transmission by an indirect experimental method. For this purpose the pressure-modulator was left off and a rotating mechanical chopper used instead, giving a signal

$$S = (B(T_s) - B(T_c))\, A\Omega \int \tau_1 \tau_2 \tau_3 \, d\nu \; A^* \, 1/\sqrt{2} \text{ divns.}$$

where Ts is the temperature of the source, Tc is the temperature of the chopper blade, τ_1 = transmission of the germanium window, τ_2 = transmission of the lens/filter combination, and τ_3 is the transmission of the light pipe. A* is the overall electronic gain of the system, in units of chart recorder divisions/watt, putting S in units of chart recorder divisions. The source side of the chopper blade was highly polished, and changes in Ts were kept small, so that Tc could be considered constant at room temperature. For a given small change in Ts, we have

$$\Delta S = \Delta B(T_s)\, A\Omega\, \tau_3 \int \tau_1 \tau_2 \, d\nu \; A^* \frac{1}{\sqrt{2}} \text{ divns.}$$

for the change in S, where τ_3 has been taken to be constant over the small range of frequencies involved. τ_1 and τ_2 were measured against ν on an Infracord spectrophotometer, the resultant curves were quantized in 10 cm^{-1} steps and plotted as histograms (fig. 7.10). The products could then be taken and the equivalent width of the lens/filter/window combination calculated by counting squares. Dividing by the width of the band gives the mean transmission as 0.27, or

$$\int_{15\,\mu\text{band}} \tau_1 \tau_2 d\nu = 99.7 \text{ cm}^{-1}$$

The field of view Ω was set by the light pipe formula (7.7), and A was obtained accurately by inserting a stop of 1 mm. radius between the chopper and the radiometer. A* is more difficult, but is available if the r.m.s. noise is measured at the same time as the signal, using the equation

$$\text{RMS noise} = N(\Delta f)^{\frac{1}{2}} A^*$$

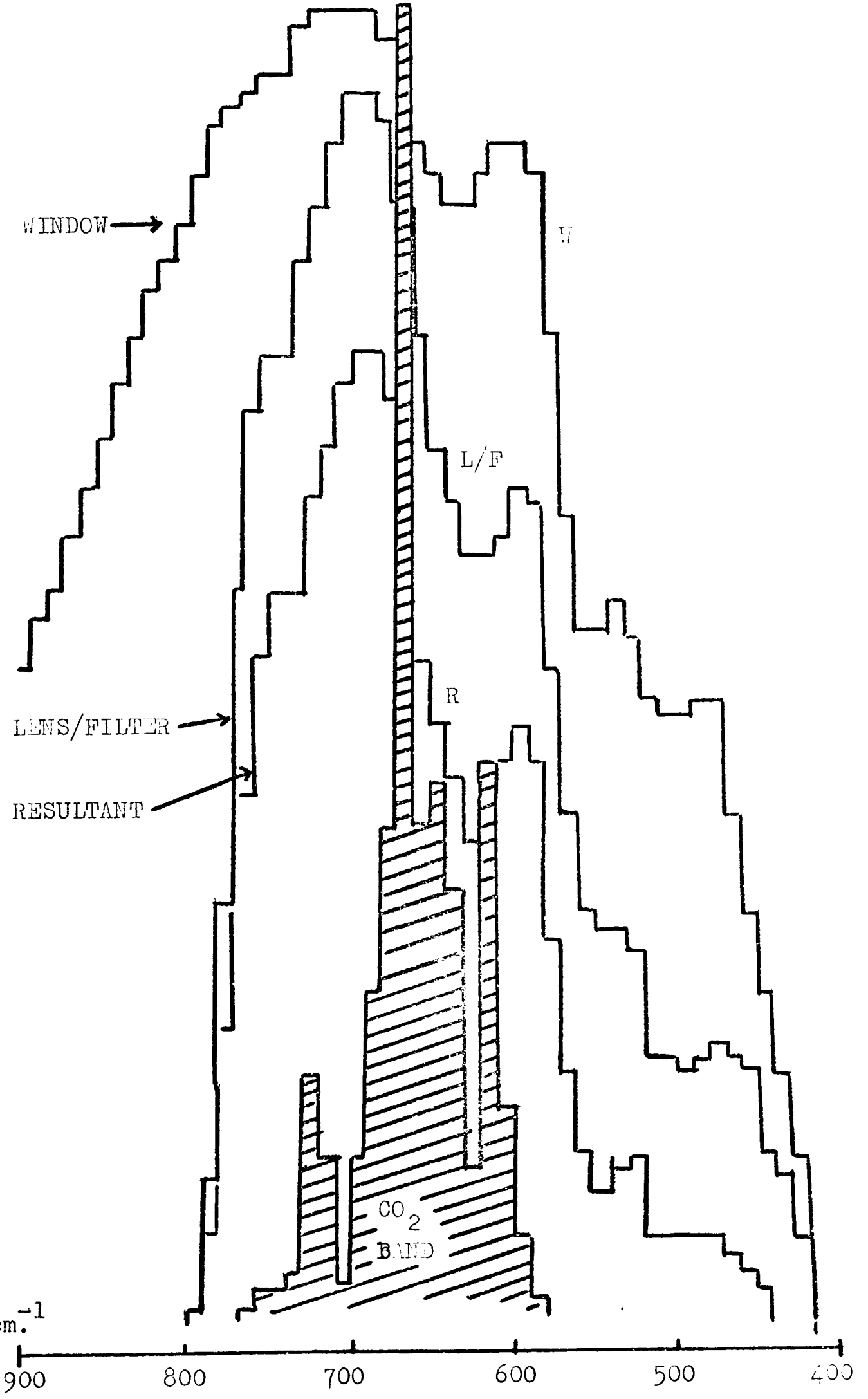


Fig. 7.10. Histograms for the light pipe transmission experiment, with the CO_2 band for comparison (6 cm., 100 mm.Hg.).

where N is the measured detector N.E.P., and $\Delta f = \frac{1}{\pi t'} = \frac{1}{5\pi}$ sec^{-1} is the electronic band width.

N was measured as being in the ratio $\frac{5.9}{2.2}$ with the Johnson noise in 100 K, so

$$N = (4\ kTR\Delta f)^{\frac{1}{2}} \times \frac{5.9}{2.2} = 10.73 \times 10^{-8} \text{ volts r.m.s.}$$

equivalent to $N = 2.68 \times 10^{-9}$ watts r.m.s. with the manufacturer's figure for the responsivity of the detector (40 volts/watt). For $\Delta T_s = 4.5^{\circ}C$, a signal change of 64 divisions and a noise level of 2 divisions were measured, corresponding to the value $T_3 = 0.54\ (\pm 0.05)$ for the transmission of the light pipe. This is an effective transmission, including the effect of the loss introduced by the 0.01 cm. gap between the end of the cone and the bolometer.

The same set-up was used to measure the transmission of the complete optical system as a function of displacement across the entrance aperture in a direction perpendicular to the optical axis, by different positioning of the 2 mm. diameter stop. The results appear in fig. 7.11 in arbitrary units which take the signal at the centre as 100. This experiment was performed as a check on the alignment and efficiency of the optics.

7.4.3. Measurement of Δp_c.

The use of a mechanical chopper enabled a further indirect measurement of the pressure swing Δp_c to be made, in a way which was independent of any consideration of the leakage rate past the piston. With the pressure modulator off, the attenuation of the signal produced by adding various amounts of CO_2 to the cell was plotted against cell pressure p_c (fig. 7.12). The graph is a straight line, as is expected at low pressures where the spectral lines do not overlap much, so that the attenuation is proportional to the equivalent width of the band W, and $W = 2(\sum_i S_i \alpha_i u)^{\frac{1}{2}} = 200\ p_c\ cm^{-1}$ for a cell 6 cm. long. If ΔS is the fractional attenuation of the signal produced by filling the cell to a pressure p_c, then

$$\Delta S \propto p_c \text{ , or } \Delta S = 200 k p_c \qquad (7.8)$$

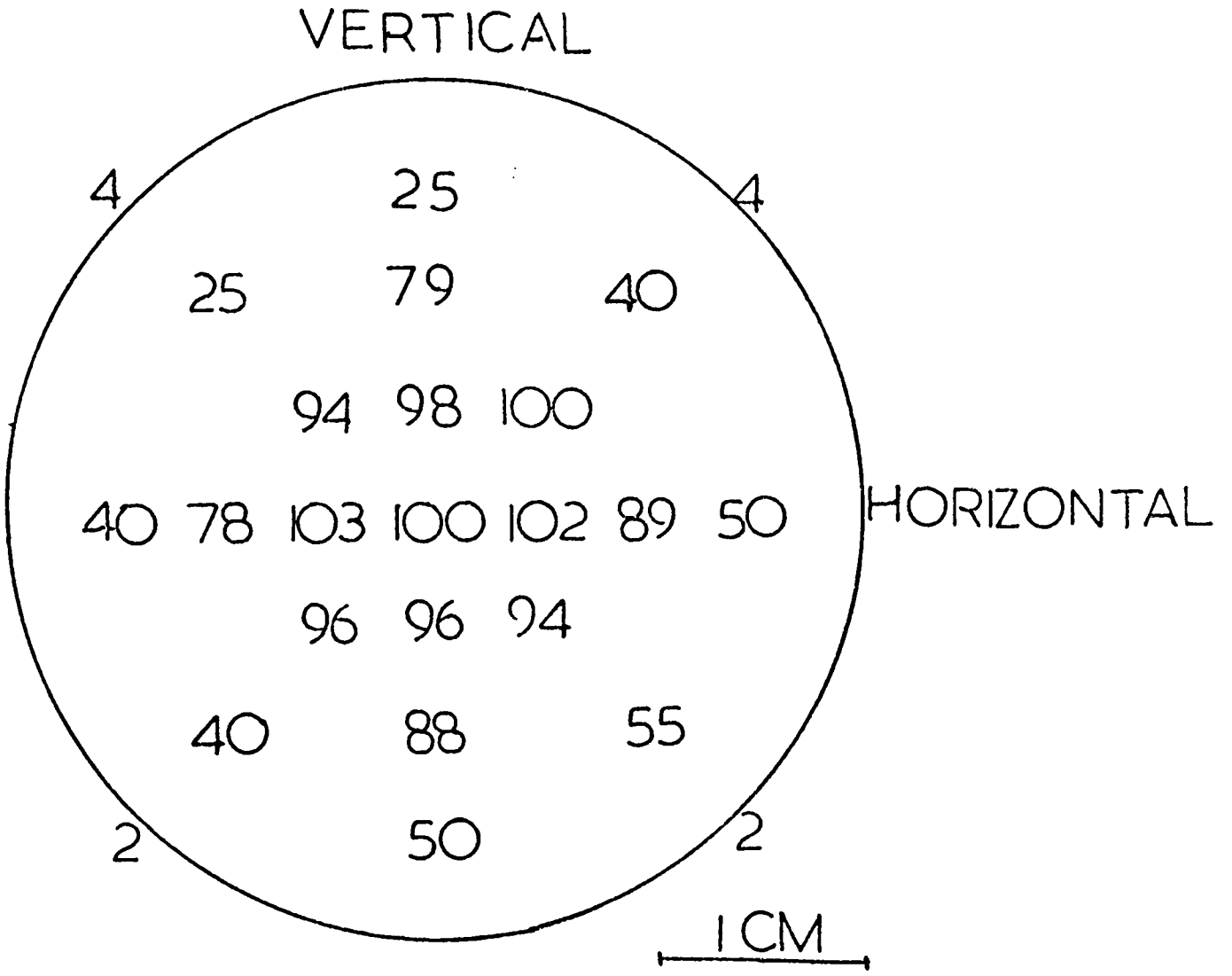


Fig. 7.11. The variation in signal strength with position of the 2mm. diameter stop across the entrance window of the radiometer, in arbitrary units . The [redacted] circle is the physical size of the window.

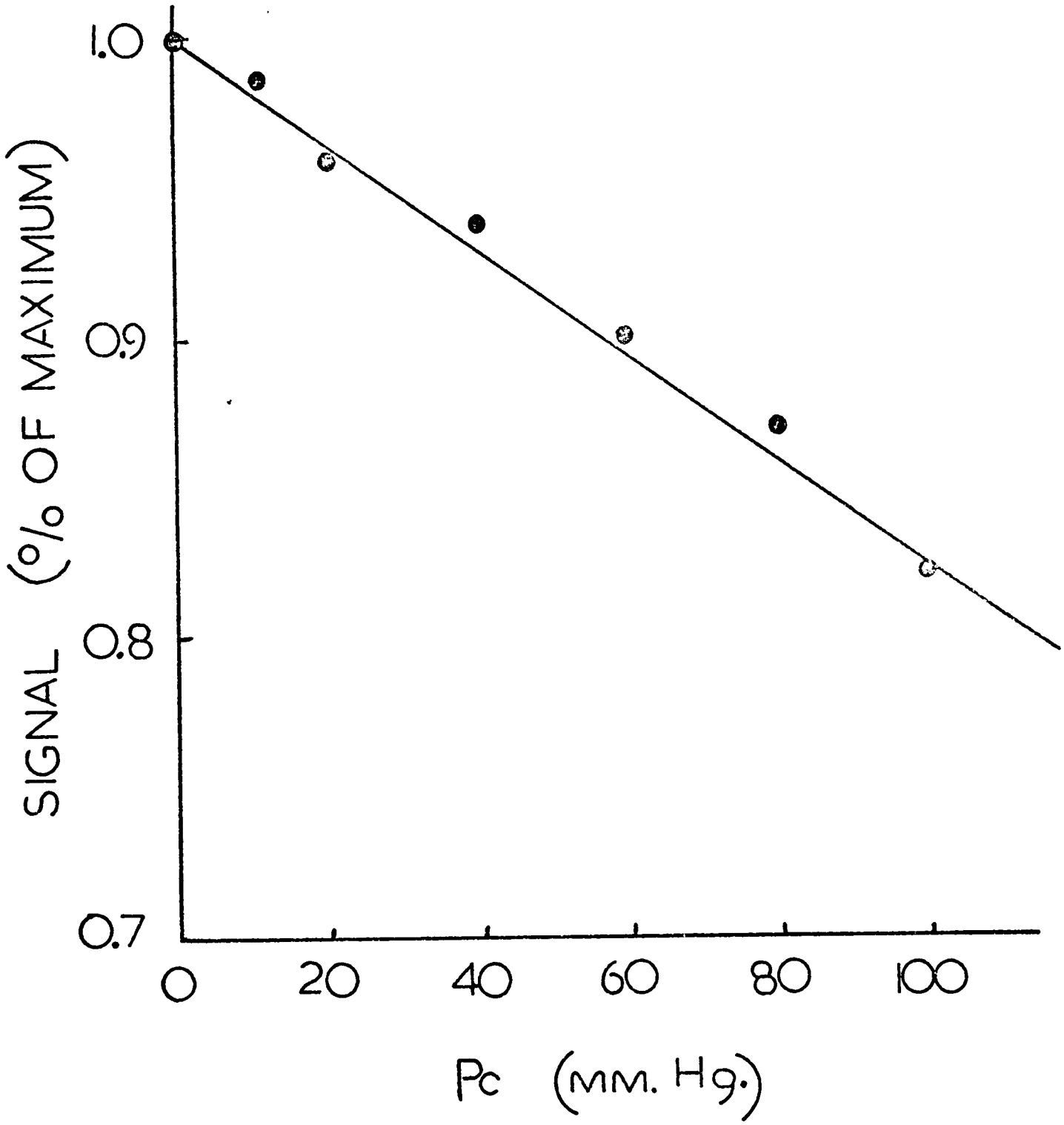


Fig. 7.12. Signal attenuation vs. pressure of CO_2 in 6 cm. absorbing path.

for some constant K. The mechanical chopper was then switched off and the pressure modulator switched on, with p_c = 1 mb. The signal is now

$$S = 200\, K\, \Delta p_c\, \beta \qquad (7.9)$$

where Δp_c is the pressure swing and β is the ratio of the stop apertures in each case (these have to be different to keep the detector electronics on scale, since the mechanically chopped signal is so much larger than the pressure-chopped one), weighted by the mean transmission measured in the preceding section. β was about 100. Now from 7.8, the slope of the graph in fig. 7.12 is $\Delta S/p_c = 200\ K = 1.6 \times 10^{-2}$ (mb.)$^{-1}$, substituting in 7.9 gives Δp_c = 0.2 mb. or 20% of the mean pressure. A simple Boyle's Law calculation using the volume of the cell and the volume swept out by the piston gives nearly the same answer (22%) showing that the leakage is indeed quite small, in support of the calculation of sect. 7.1.

7.5. Conclusion.

In its final form the instrument appeared to be capable of temperature soundings at levels up to about 70 km. with very high accuracy, and to be of relatively simple and rugged design, suitable for operational use. The next step was to construct a flight model for tests under real conditions in the atmosphere.

Chapter 8. The Balloon Radiometer.

8.1. Introduction.

The flight model radiometer described in this chapter was intended to be raised to around 40 km. by a large balloon, so that a temperature sounding from high in the upper stratosphere could be made for comparison with the profile measured by routine Meteorological Office sondes. A successful flight would establish the effectiveness of the new instrument and lend weight to a proposal for its inclusion on a forthcoming

meteorological satellite, Nimbus F, made in mid-1968.

To generate satellite-like weighting functions from 30-40 km. the radiometer must work either with a much higher mean cell pressure than would be used in a satellite model, or must use a scarcer atmosphere component. The isotope $C^{13}O^{16}_2$ is present in the atmosphere as 1% of the total CO_2 concentration, but the highest purities at present obtainable in the laboratory are only 60%. The contaminant is the common isotope $C^{12}O^{16}_2$, and this would generate a large unwanted signal. Although this could be filtered out by including an extra cell of pure $C^{12}O^{16}_2$, the uncertainties generated by the overlapping of the spectral lines of the two species are confusing and it would be difficult to be sure of obtaining unambiguous results, particularly since there is no easy way of checking the ratio of gases in the cell. It is much more straightforward to simply increase the cell pressure, although this did necessitate the redesign of the pressure modulator, as described below (sect. 8.3.1). The general structure of the package is described first, with specific information on the various systems following.

8.2. General layout.

Fig. 8.1 is a block diagram of the units making up the package. The layout is shown schematically in figs. 8.2, 8.3 and 8.4, and the real thing in plates 5, 6 and 7.

The various units were all bolted to a strong central spine, from which the package was suspended; the pressure modulator and light-pipe housings were held rigidly by tufnel clamps and dural struts to inhibit the vibrations which tended to be excited by the piston. The optical axis of the radiometer was fixed at 30° to the vertical to minimise the spherical distortion produced by the mirror used for in-flight calibration (sect. 8.4); with the mirror set in the signal position the view was vertically downwards. Before flight the whole assembly was encased in a tailored box of polystyrene foam, designed to afford mechanical protection and, more important, to insulate the vulnerable systems (especially the motor, the electronics and the battery) from the very low temperatures

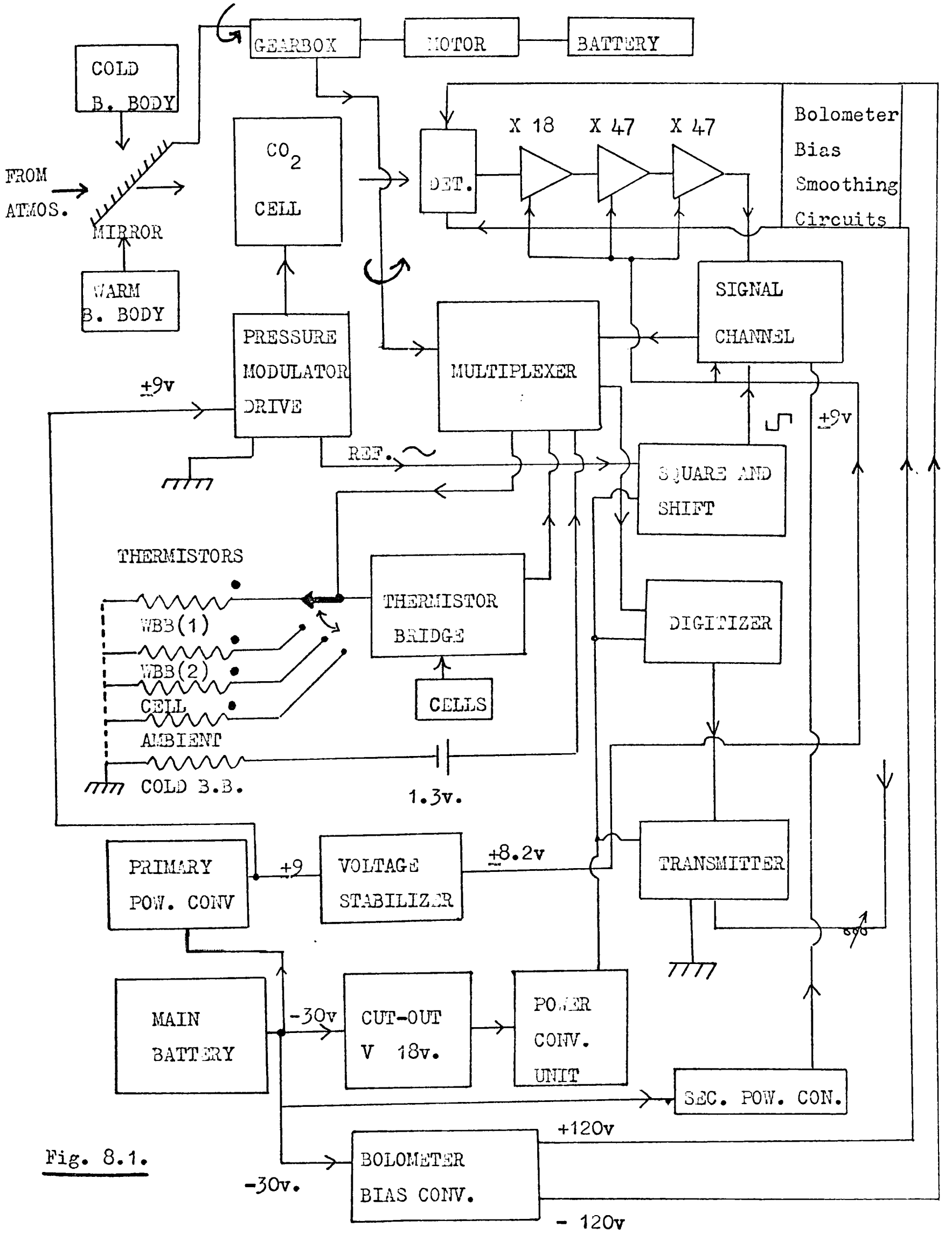

GEARBOX
MOTOR
BATTERY
COLD B. BODY
FROM ATMOS.
MIRROR
WARM B. BODY
CO_2 CELL
DET.
X 18
X 47
X 47
Bolometer Bias Smoothing Circuits
SIGNAL CHANNEL
PRESSURE MODULATOR DRIVE
±9v
MULTIPLEXER
REF.
SQUARE AND SHIFT
±9v
THERMISTORS
WBB(1)
WBB(2)
CELL
AMBIENT
COLD B.B.
THERMISTOR BRIDGE
CELLS
DIGITIZER
1.3v.
PRIMARY POW. CONV
+9
VOLTAGE STABILIZER
±8.2v
TRANSMITTER
MAIN BATTERY
-30v
CUT-OUT V 18v.
POWER CONV. UNIT
SEC. POW. CON.
+120v
BOLOMETER BIAS CONV.
-30v.
- 120v

Fig. 8.1.

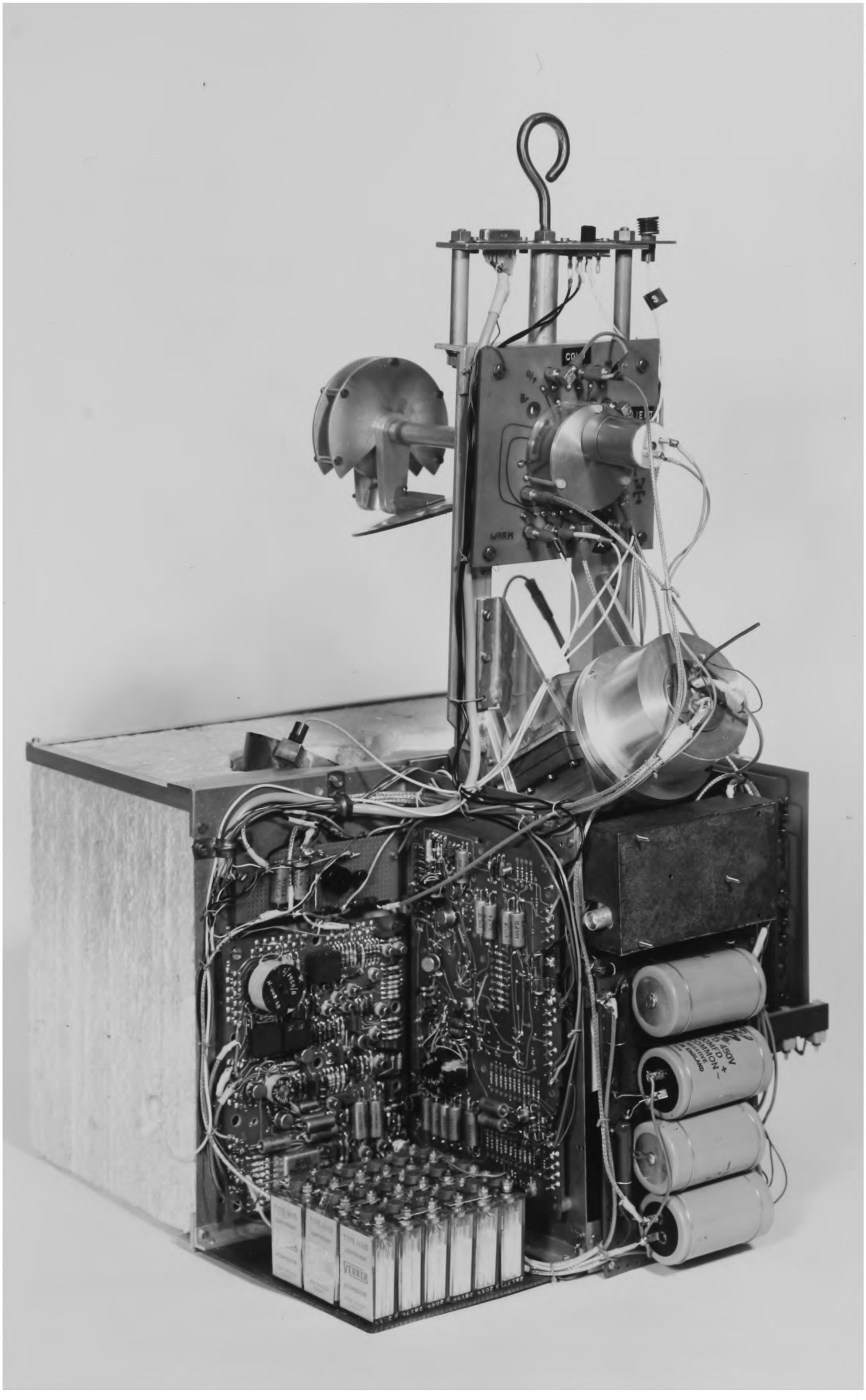


Plate 5. Balloon Radiometer - View 1.

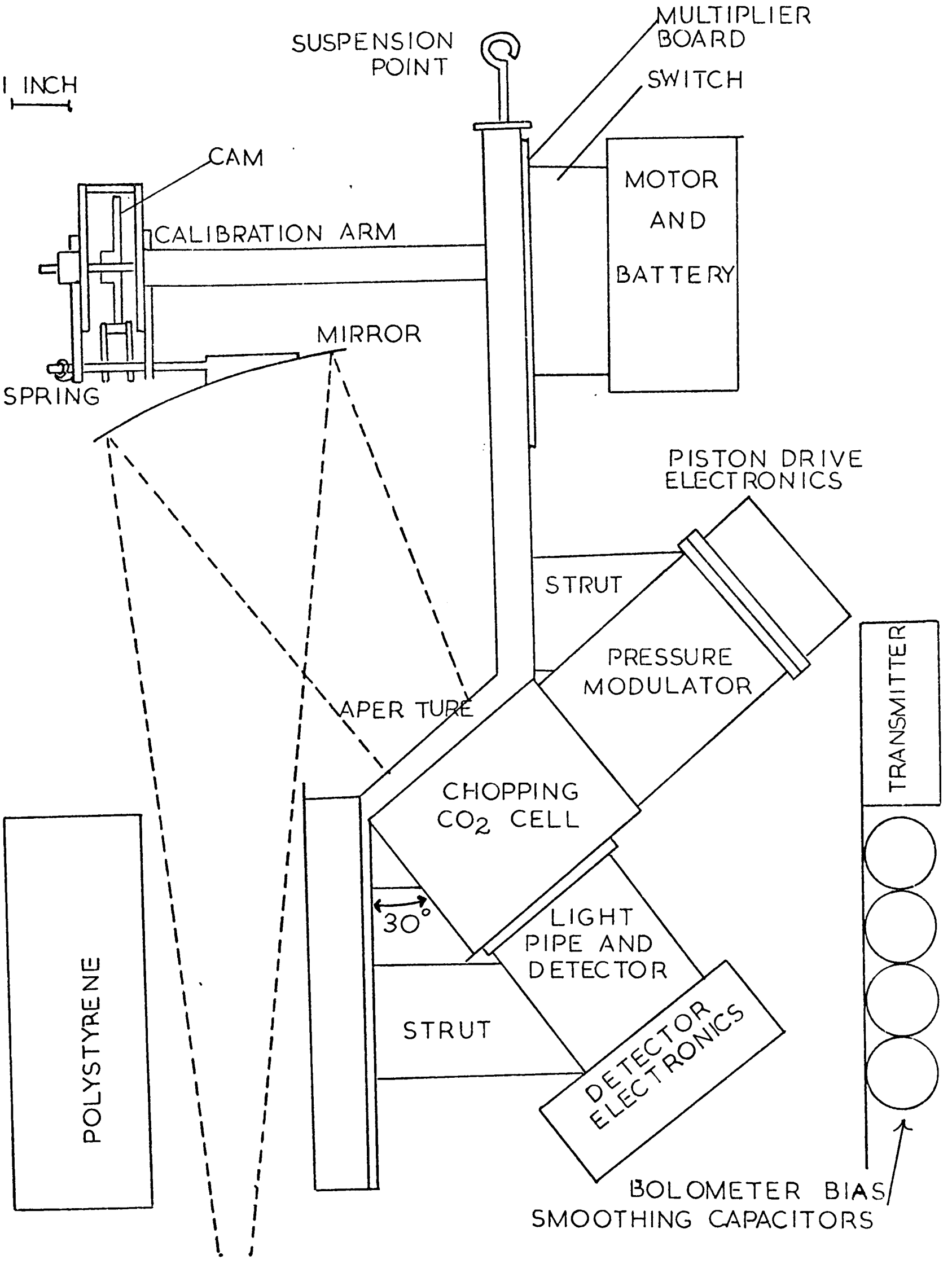


Fig.8.2. Balloon Radiometer - side view of layout.

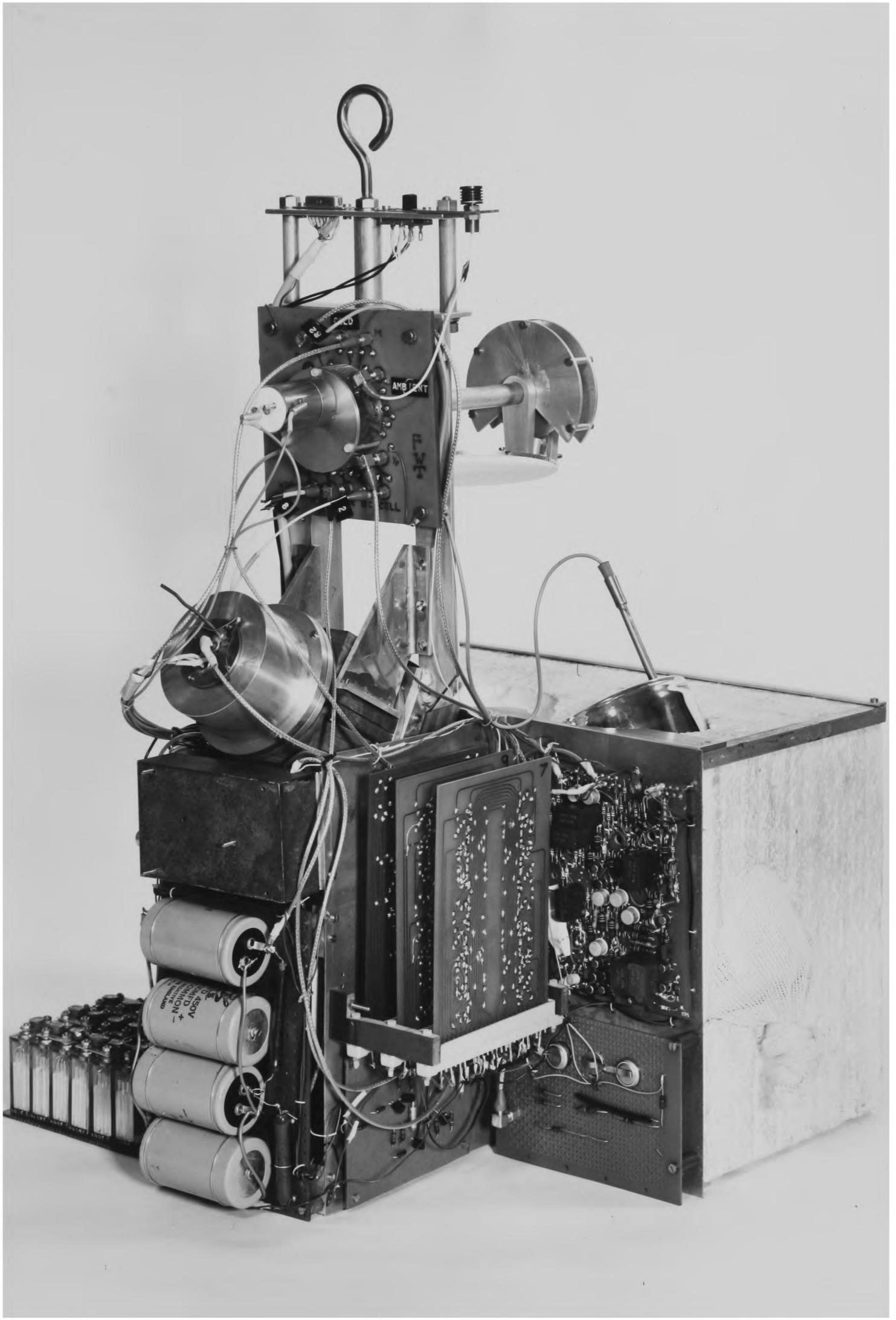


Plate 6. Balloon Radiometer - View 2.

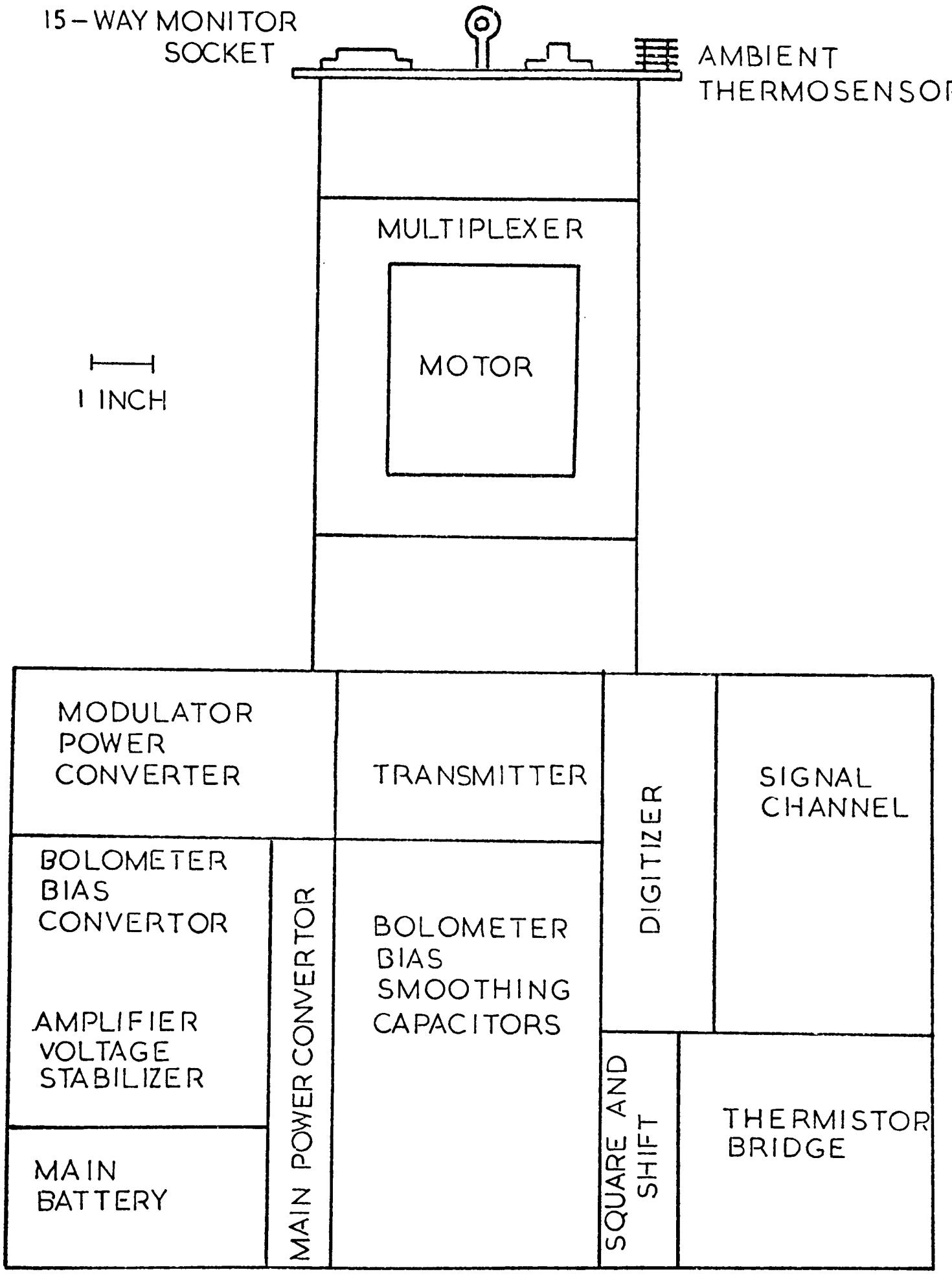


Fig. 8.3. Balloon Radiometer - rear view of layout.

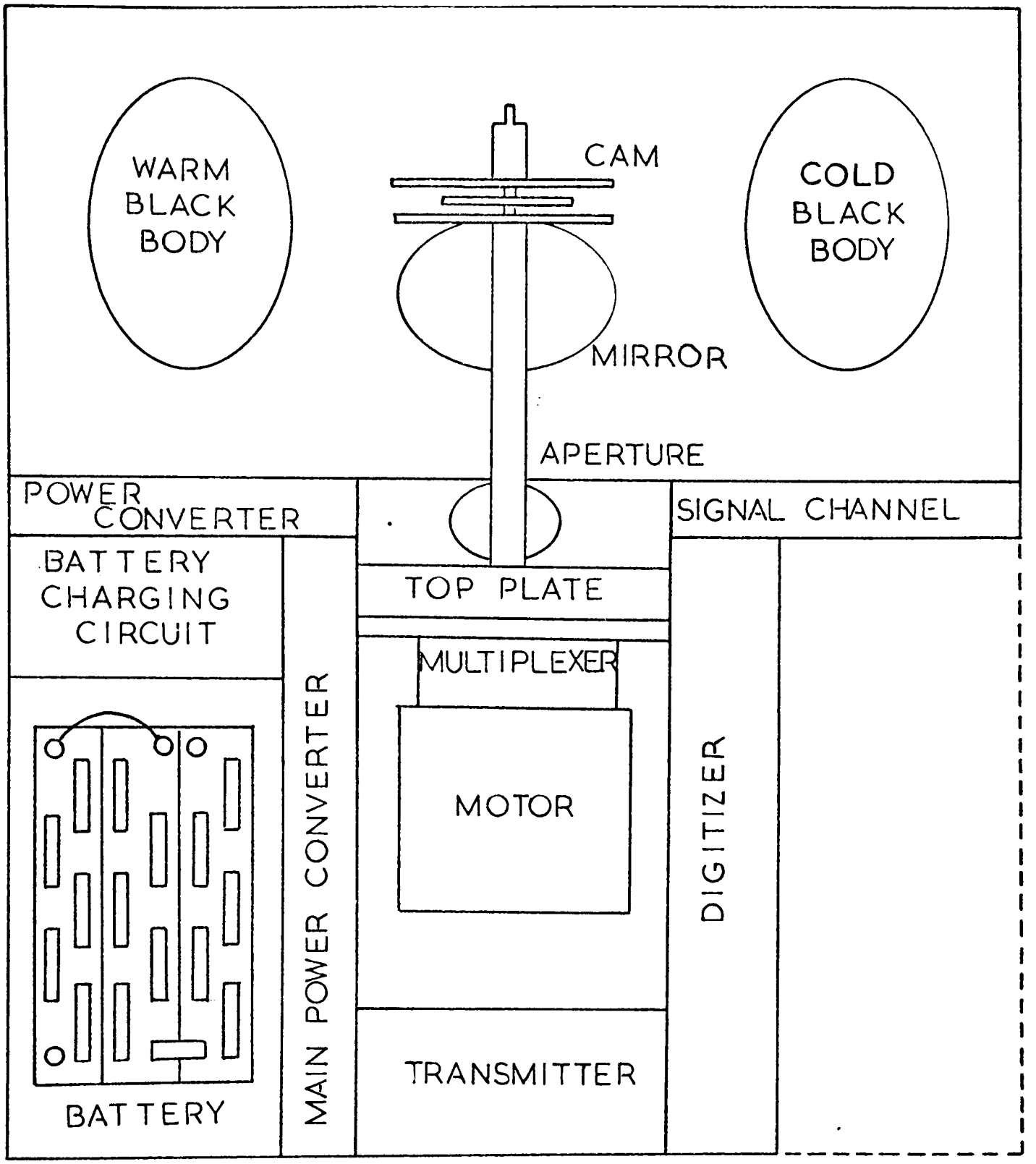


Fig. 8.4. Balloon Radiometer - plan view of layout.

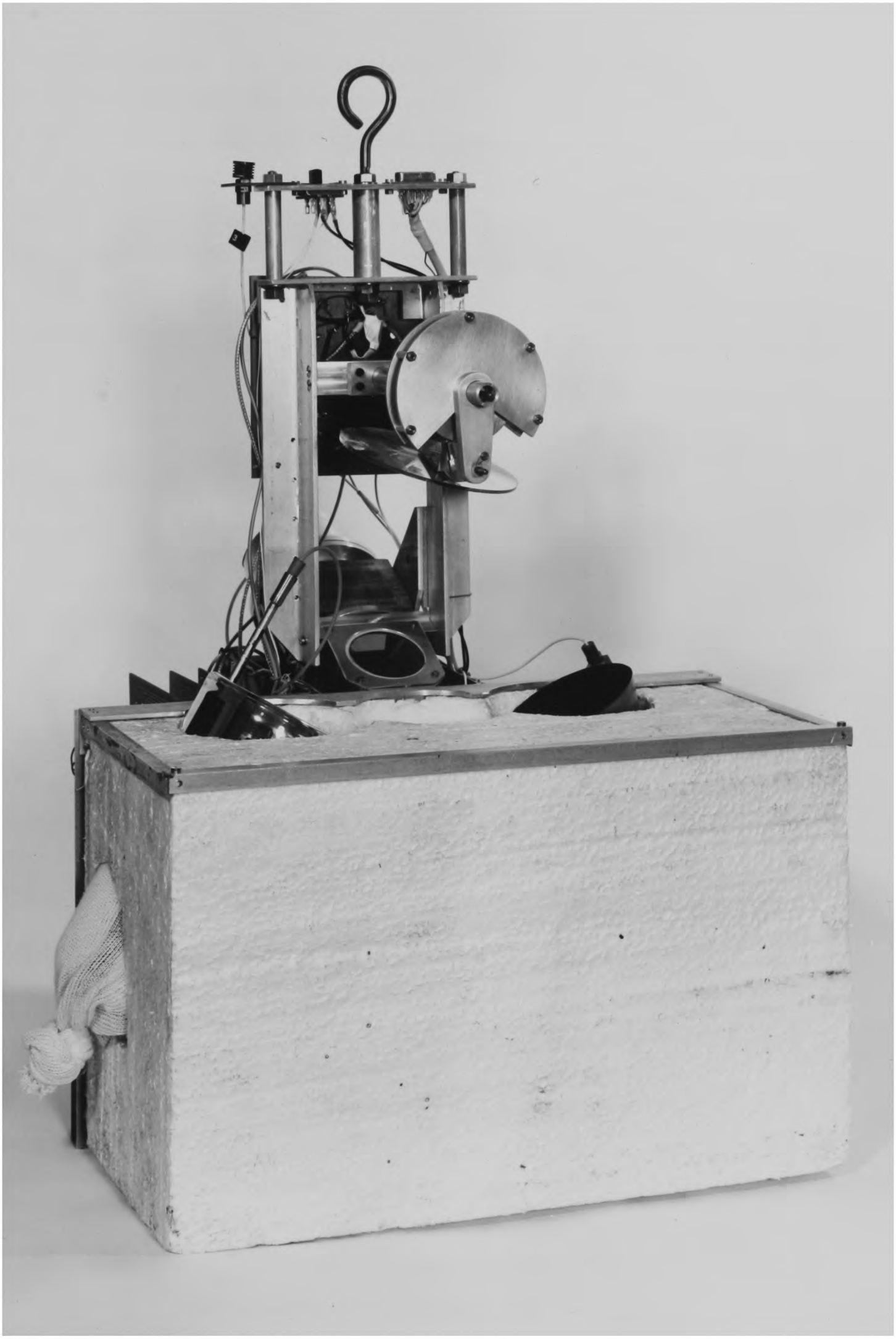


Plate 7. Balloon Radiometer - View 3.

to be encountered in the stratosphere. An on-off switch for the telemetry was provided on the outside of the styrofoam shield, as was a 15-way socket which allowed the most important voltage levels and waveforms to be monitored immediately before launch. Connections made via this socket also allowed the radiometer to be run from an external $\pm$ 20 volt supply, thus conserving the batteries. A board of simple diode logic (fig. 8.5) was included, to automatically switch the instrument over to the battery supply when the 'umbilical' socket was withdrawn.

The complete package was a cube of side 22"; it weighed a little over 20 lb.

8.3. Radiometer Systems.

8.3.1. Design of the Pressure Modulator.

A computer program was used to plot out the weighting functions for a large selection of mean cell pressures. That for p_c = 250 mb. was chosen as having the best shape, on the assumption that the instrument would reach its highest point somewhere between 25 and 35 km. The pressure modulator of the prototype radiometer, which was used successfully at p_c = 1 mb., needed some basic design changes to work at the higher pressure. Firstly, at 250 mb. the viscous drag on the piston is so large that the lightweight assembly of section 7.1 was overdamped, resulting in a very small amplitude at any reasonable power consumption.

Secondly, at this pressure the gas itself has an effective spring constant which is more than an order of magnitude greater than that of the actual springs. This results in a high natural frequency, which again corresponds to a small amplitude. Thirdly, even for fairly small piston amplitudes, leakage past the bore of the piston is again a problem. To offset these problems, one has the significant advantage that a small piston amplitude is sufficient to give a large signal, since the relevant parameter is the pressure swing Δp_c, proportional to the product of piston amplitude and p_c. There is therefore no longer any objection to a fairly high chopping frequency, indeed the 1/f noise should then be smaller, provided the other problems can be overcome. Critical damping

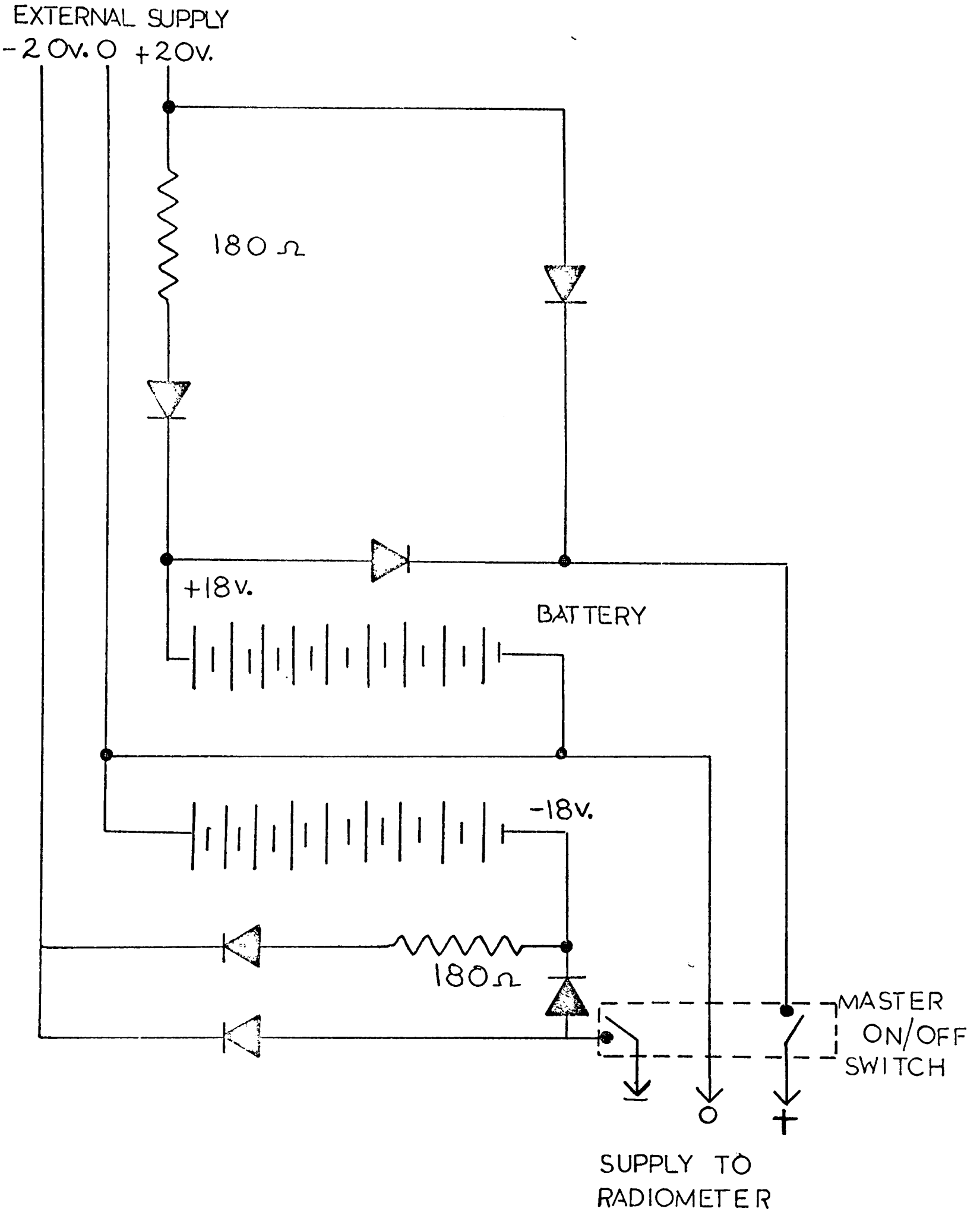


Fig. 8.5. This circuit allows the radiometer to be run from an external supply, and also supplies a 10 mA charge to the battery.

occurs when

$$\left(\frac{k}{m}\right)^{\frac{1}{2}} = \frac{f^*}{2m} \quad \text{(in the notation of sect. 7.1)}$$

and resonance occurs only when

$$\left(\frac{k}{m}\right)^{\frac{1}{2}} > \frac{f^*}{2m} \quad \text{or} \quad m > \frac{(f^*)^2}{4k}.$$

f* and k are fixed, but m may be increased. The best way of doing this is to use a larger and stronger alcomax magnet, which offers as a bonus a much stronger permanent field to give an enhanced driving force for the same power consumption. The total moving mass was thus increased from 15 gm. to 70 gm., which restored the resonant condition but tended to distort the spider springs. To prevent this the thickness of the springs was doubled, and the magnet moved to a position midway between the springs, so that it no longer exerted a torque about the mounting points. The improved lateral stability of this arrangement allowed the gap around the piston to be reduced to 0.001", and the length of the skirt to be increased by a factor of 3 to 1 cm. This solved the leakage problem. At higher pressures the question of contamination of the CO_2 is not important, provided reasonable care is taken in the choice and cleanliness of components inside the cell. This meant that the coils could be placed inside the piston cylinder, between the springs (fig. 8.6). The magnetic circuit was further improved by fitting a soft iron tube around the coils and adding mu-metal end plates to reduce the reluctance to a minimum. These doubled as shielding to prevent the field due to the coils from being picked up by the detector electronics.

The amplitude sensing element was again a small (2 x 1 x 0.1 mm.) flake of the piezo-electric material PZT, supplied by the Brush Clevite Co. This comes nickel-plated on both faces; it was attached to the spring by tinning the arm as thinly as possible (any surplus of solder results in shorting of the two sides of the flake) and applying the chip with tweezers, while providing strong local heating from the back of the spring with a large iron. A very fine wire was then attached to the centre of the exposed face by means of a magnifying glass and a special needle-like soldering iron bit. The wire was wound into a delicate

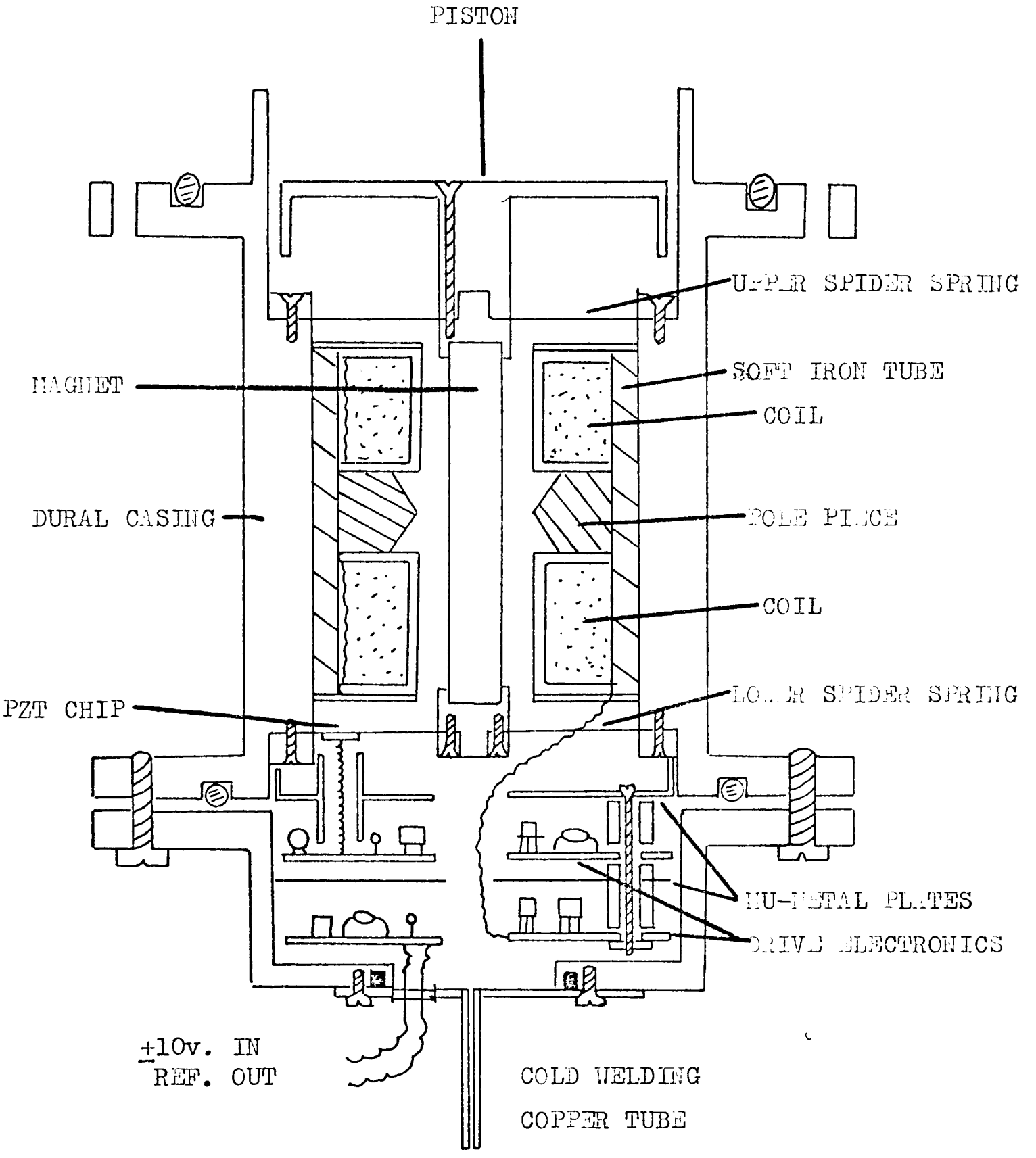


Fig. 8.6. The Pressure Modulator.

helical spring, so that there was no tendency for it to pull off the flake when the latter was moving. This lead, carrying the very small voltage from the sensor to the high impedance input of the drive electronics (sect. 8.5.1) was also very sensitive to pick-up; it was protected by a mu-metal tube and by mounting the circuitry on circular boards which could be slid inside the piston housing, thus making the lead as short as possible.

8.3.2. Chopping frequency.

The resonance frequency of the piston is now given by

$$\omega = \left(\frac{k + k'}{m}\right)^{\frac{1}{2}} \qquad (8.1)$$

where k' is the effective spring constant of the gas and $k = 1.28 \times 10^6$ gm. sec^{-2}. is the constant for the new springs. k' may be determined from the expression for the restoring force on the piston, under a small displacement x:

$$F = k'x = p_c.10^3.A\left(1 - \frac{V_2}{V_1}\right) \doteq \frac{p_c.10^3.A^2.x}{V} \qquad (8.2)$$

where A is the area of the piston and V the volume of the gas cell. Then 8.1 and 8.2 together give f = 33 c/s for V = 120 ccs., m = 70 gm. and p_c = 250 mb. The experimentally measured value for f under these conditions was 31.5 c/s.

8.3.3. Cell Emission.

At 250 mb. and 33 c/s the expansion and compression of the gas in the chopping cell results in temperature changes which occur too quickly to be equalized by the addition or removal of heat by conduction through the cell walls. The process is thus partially adiabatic, and the energy stored in the gas as heat at the end of the compression stroke is returned to the piston during the expansion stroke. The effect of this continuous heating and cooling of the gas is to generate a strong emission signal

which is 180° out of phase with the true signal. The emission signal is strong because the whole of the equivalent width of the 15μ band is involved, whereas the true signal is proportional only to the change in equivalent width produced by the pressure swing. The magnitude of the temperature swing in the cell can be calculated from a measurement of the emission signal. It was found that a source at 95°C above ambient produced a signal which just cancelled the emission. The temperature swing is then

$$\Delta T = \frac{\Delta W}{W} \times 95 = \frac{\Delta p_c}{p_c} \times 95 \doteq \gamma \frac{\Delta V}{V} \times 95 = 3.1^{\circ}C$$

If the cycle in the gas was purely adiabatic, a temperature swing of

$$\Delta T = T\left[1 - \left[\left(1 - \frac{\Delta V}{V}\right)\right]^{\gamma - 1}\right] = 4.5^{\circ}C$$

is predicted.

The effect of the cell emission is to introduce a large zero shift in the signal measured by the radiometer. The size of this shift is approximately equal to the largest true signal to be measured, and so the dynamic range of the instrument is halved unless an electronic zero shift is introduced to compensate. The signal channel board was modified so that this could be done (sect. 8.5.2), but the effects of changes in the cell emission signal due to variations in the temperature of the CO_2 are less easy to allow for since a small change in the temperature of the gas produces the same change in output as a much larger change in the source temperature, these being in the ratio $\Delta W/W$. This effect means that regular in-flight calibration is essential (sect.8.4), plus heavy thermal insulation of the CO_2 cell to prevent the possibility of the signals drifting right off scale.

8.3.4. Optical Design.

This was essentially the same as the prototype described in chapter 7. To save weight, the solid brass light tunnel was replaced by a thin copper cone 0.01" thick made by electrodeposition onto a polished stainless steel former. The result was gold-plated and fitted with flanges on either

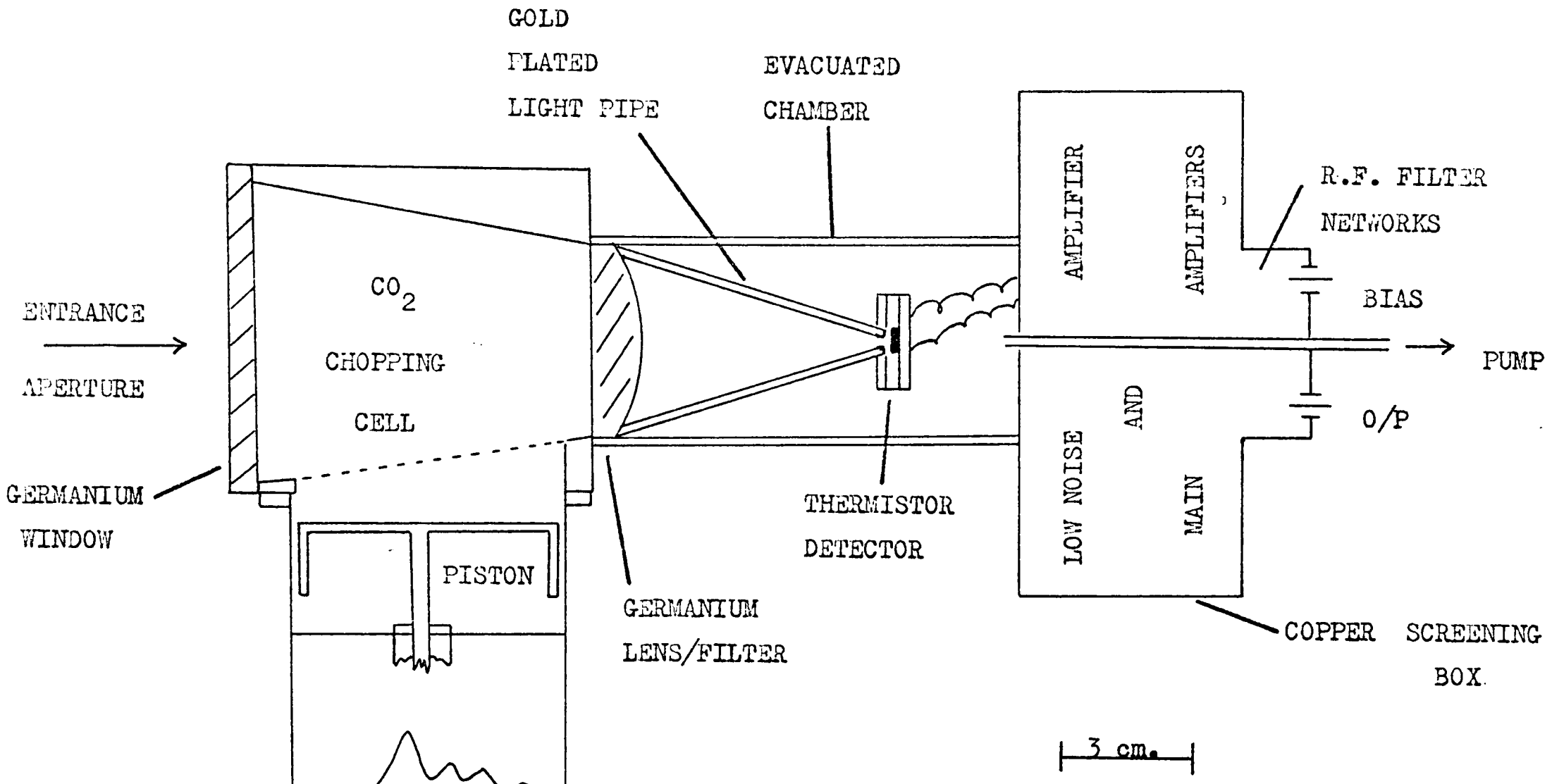


Fig. 8.7. Simplified diagram of the optical system.

end to take the lens-filter and the detector. This assembly was mounted with epoxy resin inside a thin dural cylinder, and evacuated; the detector head amplifier was mounted directly behind the detector and enclosed in a thin copper screening box. The chopping cell itself was conical in shape to minimise the dead volume, machined out of a $3\frac{1}{2}$" cube of aluminium alloy. This offered easy mounting of the pressure modulator and light pipe assemblies by bolting them to adjacent faces of the cube,with O-ring seals, and easy mounting of the whole radiometer to the framework. The same lenses and windows as before were used, held in place by thin plates of hard magnesium alloy and sealed by epoxy resin.

8.3.5. Epoxy Resin.

As well as the germanium window, the magnet and light pipe were fixed with epoxy resin and all were in contact with the CO_2 in the cell. Commercial resins such as Epicote or Araldite use hardeners which are based on aldehydes, and cannot be used because of the strong affinity of the latter for CO_2. Ellis (1968) has successfully used the resin Epicote 828 in the presence of CO_2 by replacing the aldehyde hardener by the substance dodecenyl succinic anhydride (d.d.s.a.). If a trace of the original hardener is added as an accelerator, the setting time is reduced from days to hours at 95°C.

In the case of the window, which has to be glued to the duralumin cell, the expansion coefficients are so dissimilar (11 and 24 x 10^{-6} $^{o}C^{-1}$ respectively) that there is a risk of the seal being broken under temperature changes, due to the low flexibility of the resin once set. To overcome this, a large proportion of dibutyl phthalate was added as a plasticizing agent, resulting in a strong, flexible joint. Unfortunately, with the phthalate added the resin becomes so thin at the curing temperature that it tends to flow out of the joint and obscure the window. This can be avoided by the use of a thixotroping agent, or by partially curing the resin before application. The final composition of the adhesive was:

Shell Epicote 828 (resin)		100 parts
dodecenyl succinic anhydride (hardener)		130 parts
Shell K54 (accelerator)		0.5 parts
dibutyl phthalate (plasticiser)		100 parts
Aerosil 2491	(thixotroping agent)	4 parts
Triethylanolamine acetate	(thixotroping agent)	1 part

8.4. In-flight calibration.

Regular calibration of the instrument during flights was considered necessary to enable the measurements to be interpreted correctly in the face of possible drifts in the electronic gain, loss of CO_2 from the chopping cell, or changes in the piston amplitude caused by ageing or temperature effects in the mechanical or electrical components. Two systems were considered. Firstly, it is possible in theory to predict the magnitude of the second harmonic of the emission signal from the pressure-modulated gas, so that if this is measured the overall gain of the system is specified. However, the theory indicates that the harmonic intensity will be much smaller than that of the fundamental, and in fact an attempt to detect the signal at twice the chopping frequency was unsuccessful. A less elegant but more reliable method is to provide a cold and a warm black body within the package, representing full scale and calibration signals respectively, and to arrange for the radiometer to view each between every measurement of the signal from the atmosphere. Both sources were deep blackened copper cones, the cold one being part of a copper can containing liquid air and enclosed in a dewar flask. The 15μ radiation from a black body at 77°K is negligible compared with that at any temperature found in the atmosphere, so this measurement gives the pure emission signal from the cell. The cold black body was arranged so that the gas boiling off escaped from the apex of the cone, thus keeping the blackened surface free from frost. A carbon resistor was fitted through the filling hole as a temperature sensor, whose purpose was to indicate when the coolant ran out. The temperature of the warm black body had to be measured to within 1°C. Two STC thermistors, type M52, were used, one at each end. Thermistors

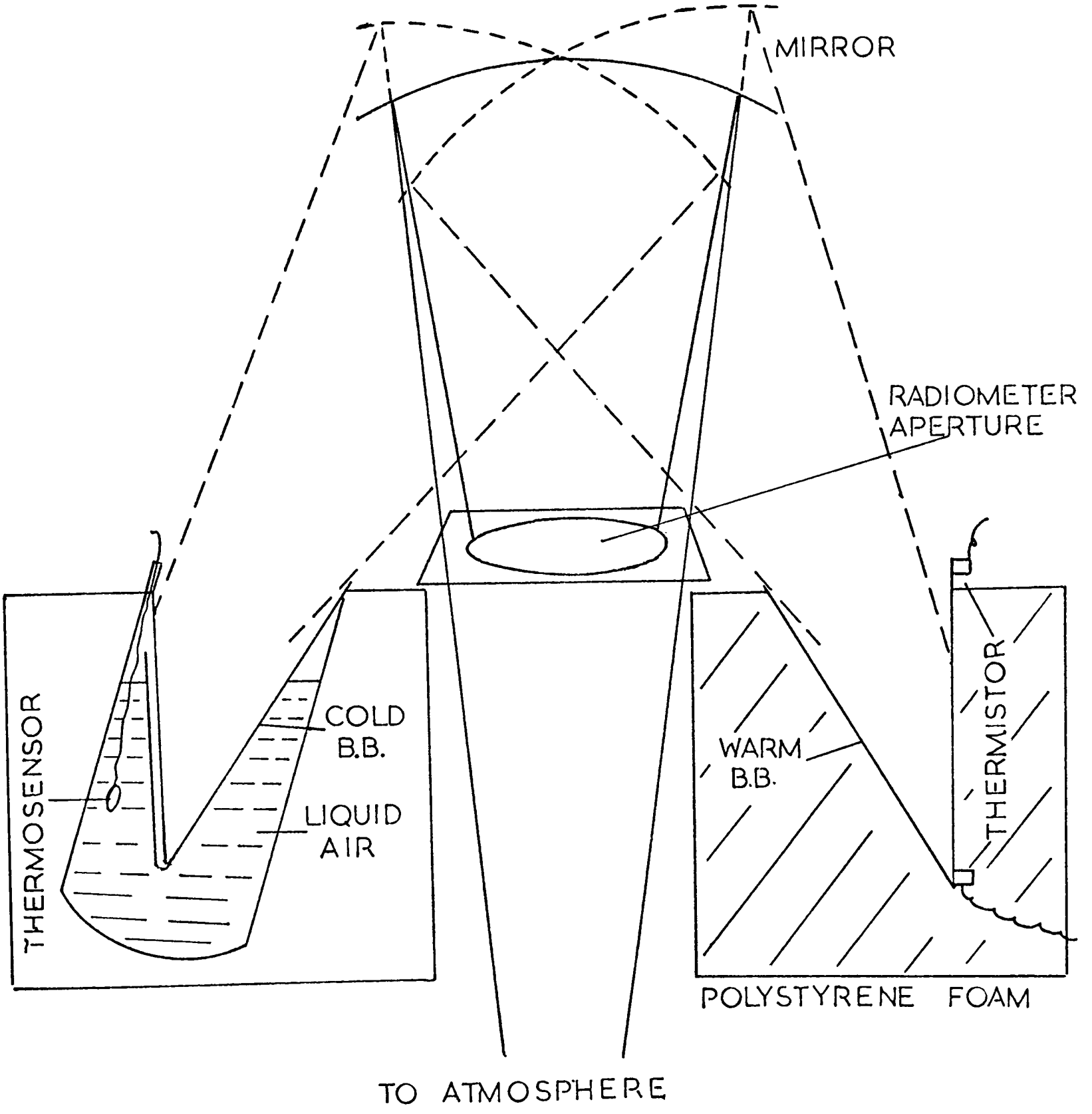


Fig. 8.8. The Calibration System.

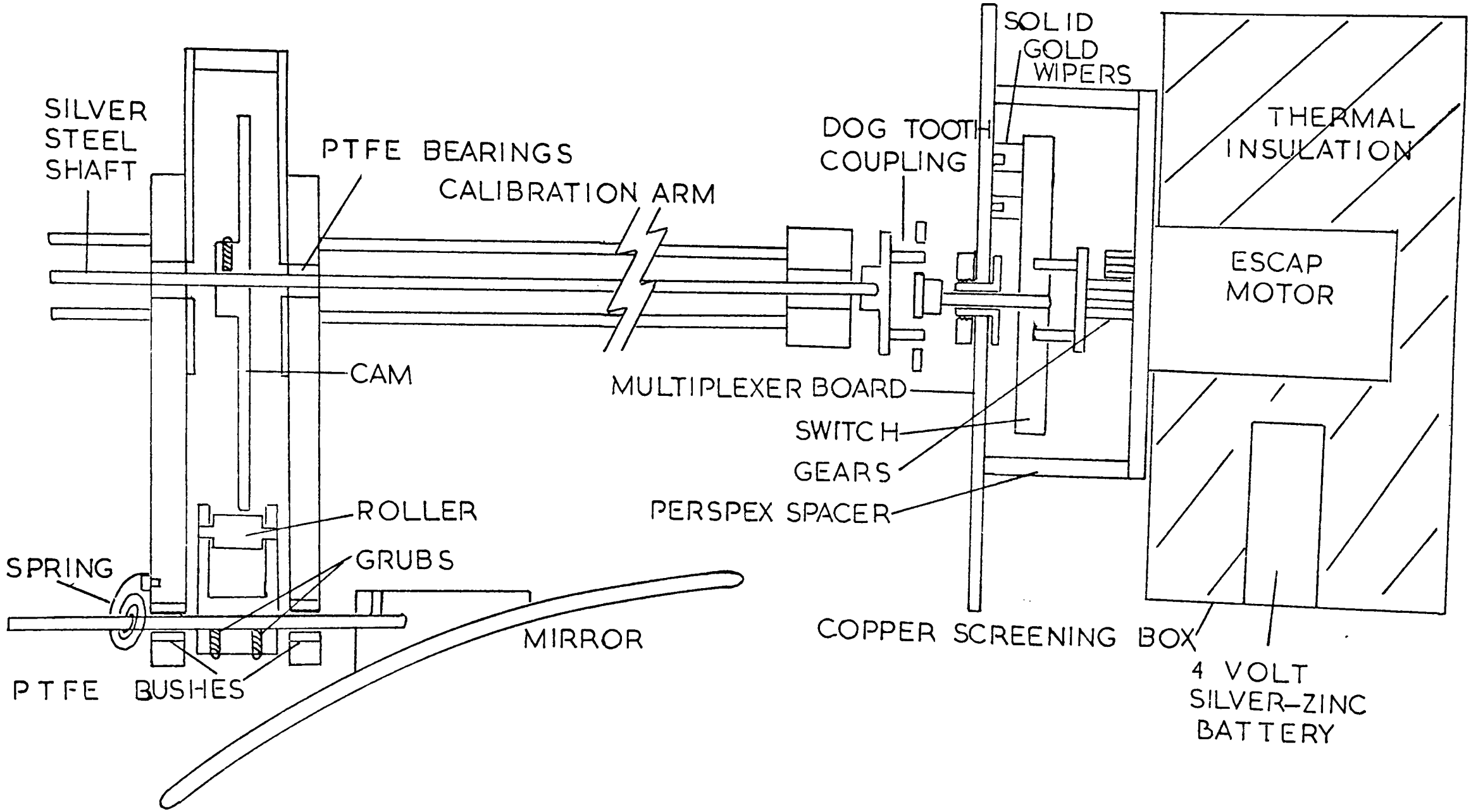


Fig. 8.9. Details of the Calibration Arm and Multiplexer Assembly.

were also used to measure the temperatures of the gas cell and the ambient.

The field of view of the radiometer was switched between the downward view and the reference black bodies by means of a spring loaded mirror tilted by a motor-driven cam (fig. 8.9). A concave mirror of focal length 20 cm. was used to converge the radiation from the black body and viewing apertures; these would otherwise have been excessively large due to the 5° divergence of the field of view. The radiometer itself was mounted with its optical axis at 30° to the vertical to minimise the angle of incidence with the mirror so that the spherical distortion was small.

8.5. Electronics.

Some of the electronics shown in fig. 8.1 (the signal amplifiers, the bolometer bias converter, and the $\pm$ 8.2 volt stabilizer) were unmodified versions of those designed by B. J. Matley and constructed by Elliot Automation Ltd. for the selective chopper radiometer on Nimbus D. These will not be described in detail here; fuller accounts may be found in the reference Elliot Bros. (1969).

8.5.1. Piston drive electronics.

This circuit was designed by G. D. Peskett, and is shown in fig.8.10. The output stage provides pulses to the driving coils which occur when the magnet is in its rest position, and are of a duration which is inversely proportional to the amplitude of the piston as measured by the output from the piezoelectric flake on one arm of the lower spider spring. This has the effect of maintaining the piston amplitude constant under changing mechanical conditions and also of keeping the oscillations of the resonance frequency of the piston assembly, even if this changes during the flight.

The pzt flake behaves like a capacitance of approximately 1000 pF; the voltage across it varies as it is flexed and, provided the springs

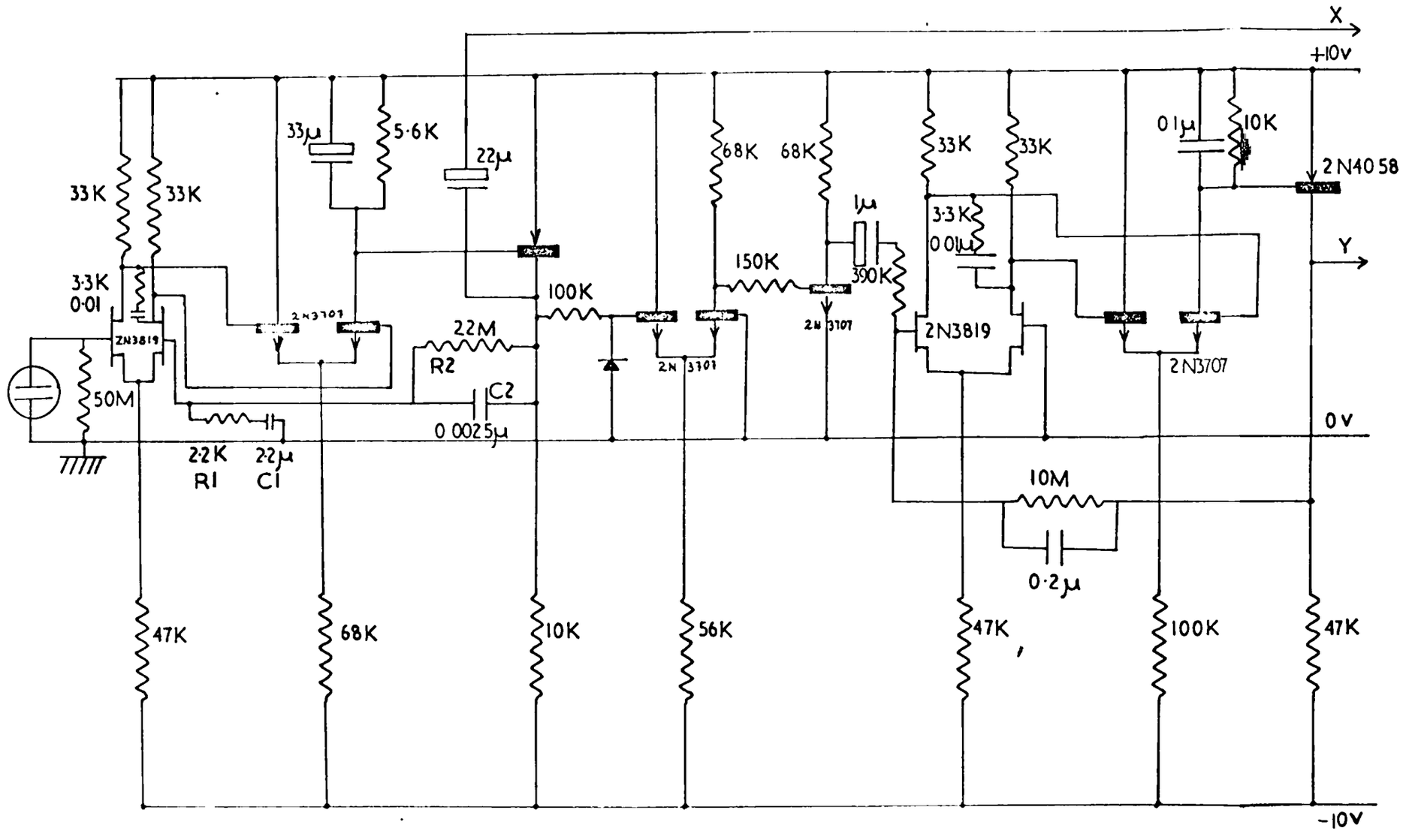


Fig. 8.10(A). Piston Drive Electronics - Board 1.

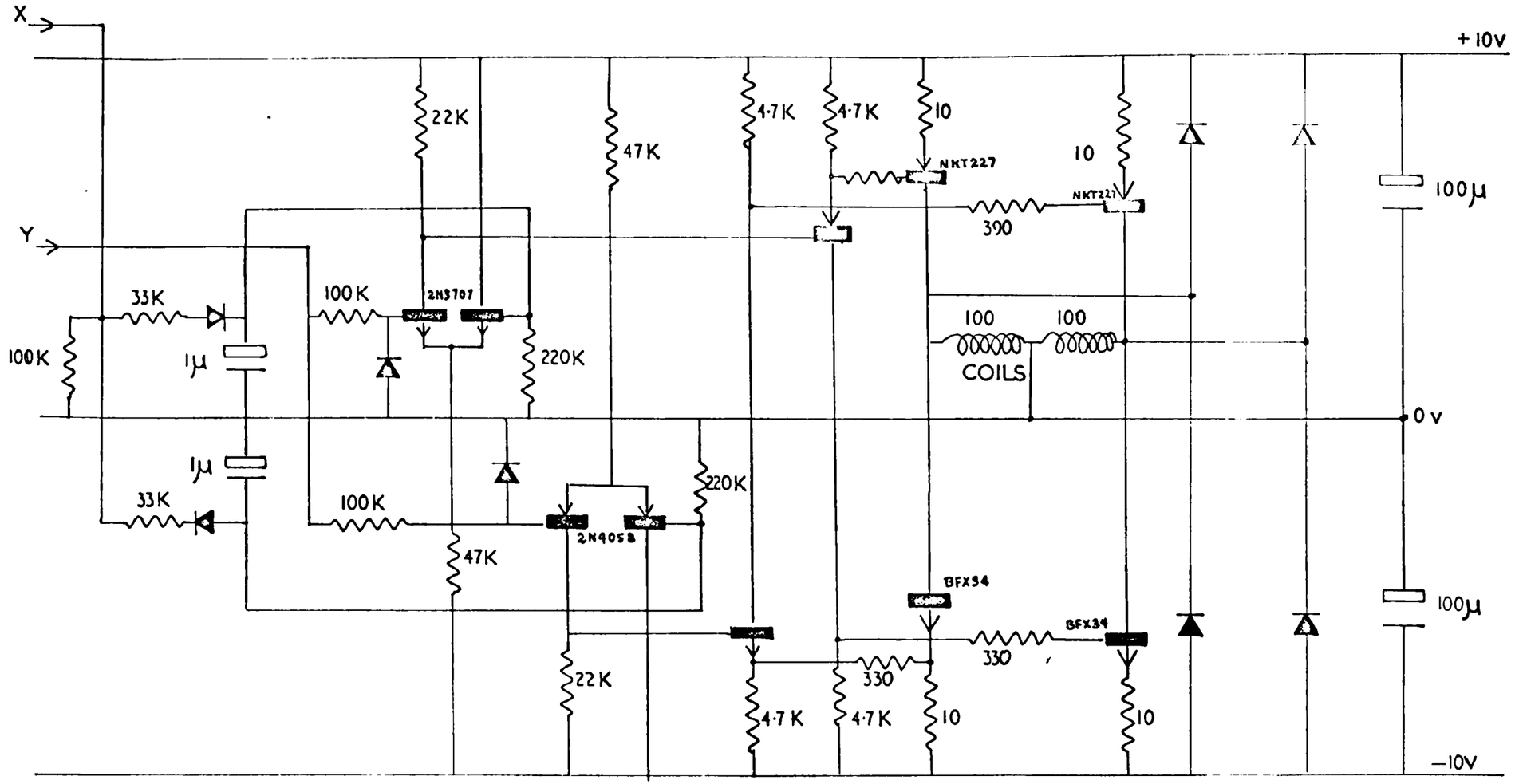


Fig. 8.10(B). Piston Drive Electronics - Board 2.

are not overdriven, constitutes a sine wave of a few mV amplitude. This signal is amplified by about x 1000 by an amplifier of high input impedance and appears at the point X. The voltage at X is used to switch an integrator of long time constant, so that a triangular waveform of constant amplitude 2 volts p-p (independent of the piston amplitude) appears at Y. The amplitudes of the waveforms at X and Y are compared by the next stage, and the output transistors switched on whenever the absolute value of the sine wave is less than that of the triangular wave. This means that the drive current is supplied to the coils for a longer part of each cycle if the spring amplitude is small, and vice versa. The 100 μF capacitors and diode pairs were added to the output stage to reduce the imductive spikes which are otherwise produced by the coils at the end of each pulse of current.

The amplitude of the piston is controlled by adjusting the feedback network in the first network, i.e. the values of R1, C1, R2 and C2. The arrangement has $R1 \ll R2$, so that the negative feedback is unity at very high frequencies, when the impedance of pair R2C2 is small, and unity again at very low frequencies, when that of R1C1 is very large. The feedback is a minimum at some frequency in between, and if the values are chosen so that this peak in gain coincides with the natural frequency, fairly effective rejection of overtones and 50 c/s pick-up is achieved. It is also important to adjust the first amplifier for the correct phase shift, otherwise the driving pulses are out of phase with the motion of the piston and the modulator will not run. This additional constraint determines the values of R1, C1, R2 and C2 uniquely for a chosen piston amplitude. In practice these were determined by breaking the loop at the point X and connecting in a signal generator. The outputs of the generator and the first amplifier are then compared on a double beam oscilloscope, and the former adjusted until the required piston amplitude results. Different values of R1, C1, R2 and C2 are then tried until the two waveforms are identical in amplitude and phase. The oscillator can then be discarded and the loop closed.

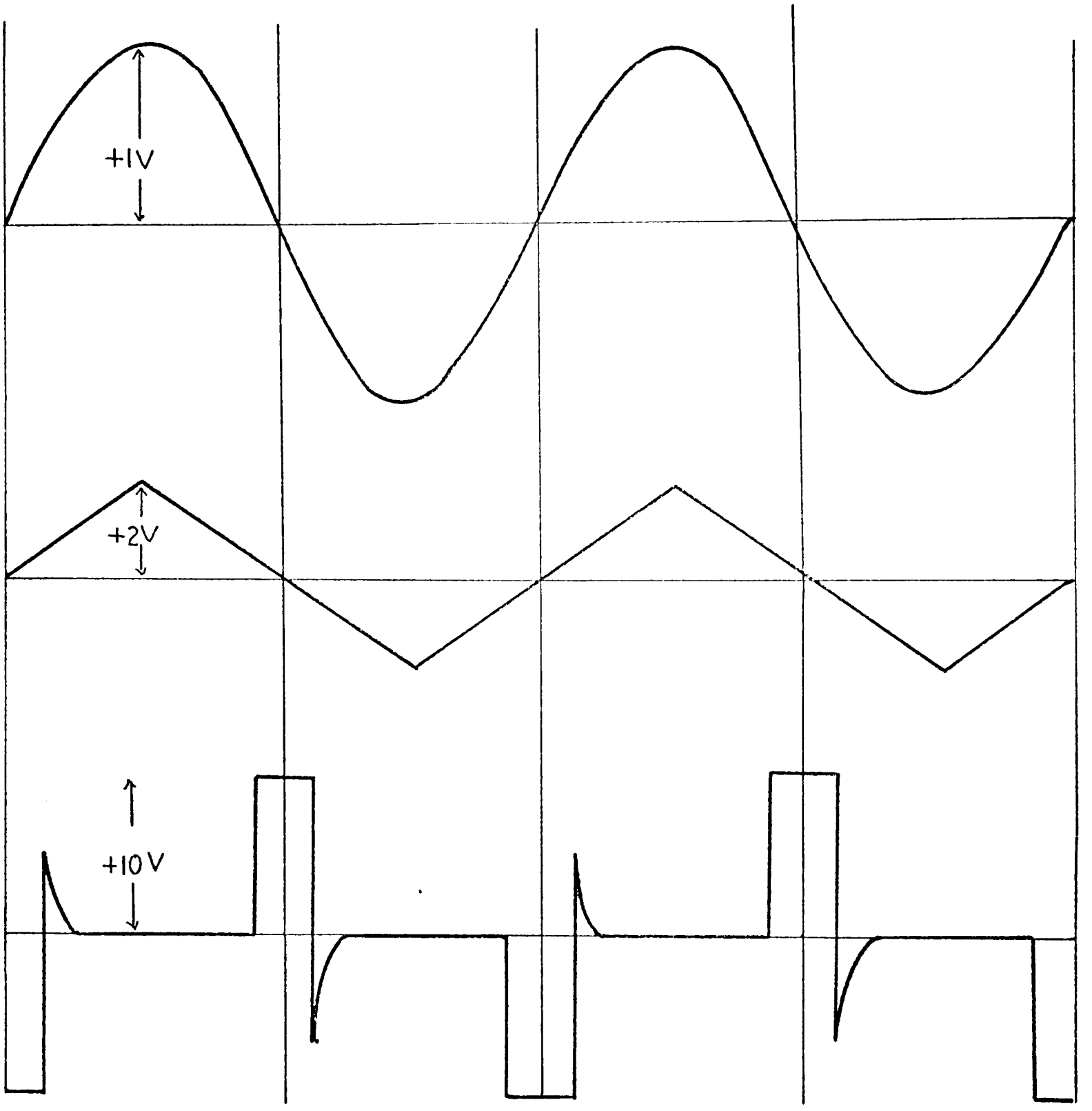


Fig. 8.11. Waveforms associated with the piston drive circuit.
Top, at X; Centre, at Y: Bottom, at the drive coils.
The vertical scale is different for each curve, as shown.

8.5.2. Signal Electronics.

The circuits of the X18 low noise amplifier and the X47 main amplifiers are the same as those described in the previous chapter. On the flight package these made up a detector head amplifier with a gain of about 40,000 and a bandpass of 400 c/s; this was extremely sensitive to both low frequency oscillations, which could be induced by any transients entering the system, and to saturation by radio-frequency fields. The latter problem was so serious, due to the high intensity of the r.f. field generated by the carefully tuned $\lambda/4$ aerial, that special precautions were required before the head amplifier would operate normally with the transmitter on. Firstly, all leads into the copper screening box surrounding the circuit boards were taken through Erie filtercon lead-throughs; these have an attenuation of 20 dB at 27 Mc/s. Inside the screen, r.f. filters consisting of 4700 pF/6.5 μH/4700 pF π networks were added to the $\pm$ 8.2 and 0v. lines to the amplifiers and to the $\pm$ 120v. supply to the bolometer. Finally, the top of the outside of the package was covered with 0.002" copper foil.

The amplified signal was led into a signal channel board (fig. 8.12) consisting of a synchronous integrator, further amplifiers of adjustable gain and a phase-sensitive detector with a 5-second time constant. The synchronous integrator consists of a switched low-pass RC filter, tuned to the frequency of the pressure modulator, and acts as a narrow band filter of about 1 c/s band width. The signal to noise ratio is therefore improved by a factor of 20 at this stage. The reference voltage for the synchronous filter and p.s.d. was a square wave derived from the piston drive network via the squaring circuit of fig. 8.13, which also provided an adjustable phase shift. This board consisted of a 'concertina-type' phase splitter, an FET amplifier with a gain of 2.5 and a long-tailed pair acting as a clipper. The intermediate FET stage was found to be necessary to prevent a distorted square wave from being generated when the output from the pzt was not a perfect sine wave.

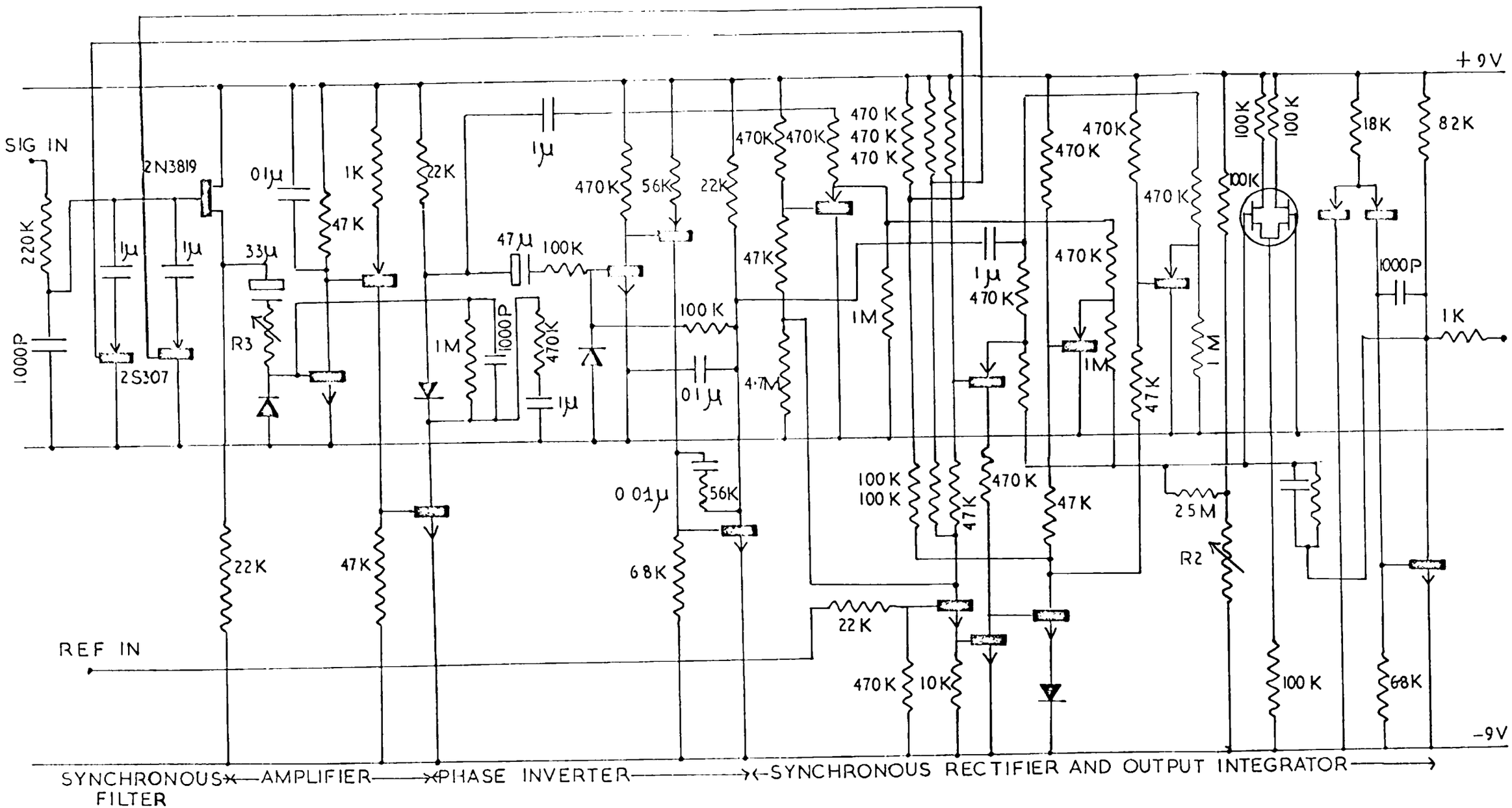


Fig. 3.12. The Signal Channel. All transistors are type BFX 37 (PNP) and 2N 2484 (NPN) unless otherwise shown.

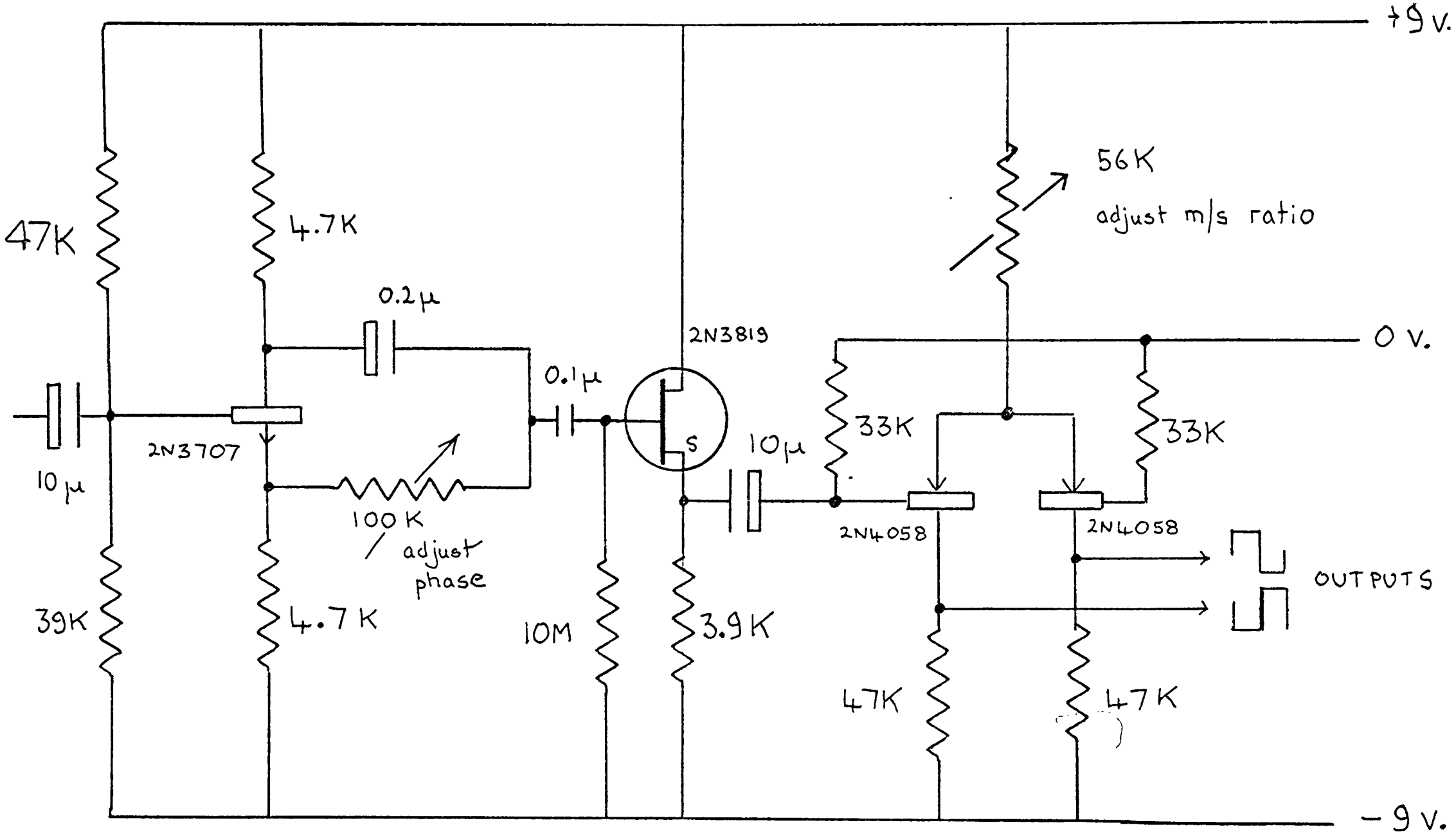


Fig. 8.13. Reference Squaring and Phase Shifting Circuit.

The output of the signal channel was a d.c. level of 0 to +8 volts. As the telemetry (sect. 8.6) required a current input in the range 0 to 330μA, the signal channel output was led via a 22K series resistor and the multiplexer switch to the digitizer input.

8.5.3. Power supplies.

Power for the radiometer was provided by a battery of 18 Venner silver-zinc accumulators, type H105. They were chosen for their light weight (1.125 oz.), high capacity (1.5 amp. hours) and small dimensions (1" x 2" x $\frac{5}{8}$"). The total voltage varied from 36 volts when full charged, through a plateau of 28 volts, to less than 18 volts near discharge. This supply had to be converted to $\pm$ 120 volts for the bolometer bias, $\pm$ 10 volts for the pressure modulator, $\pm$ 9 volts for the telemetry and $\pm$ 8.2 volts for the head amplifier. To prevent harmful interactions down the power lines, three separate power converters and a stabilizer were employed (fig. 8.1). The bolometer bias converter is a DC-AC-DC converter with an intermediate frequency of 20 kc/s, providing a stable $\pm$ 120 volts for any direct battery input greater than 18 volts.

The power converter unit supplying the signal channel (fig. 8.14) featured double smoothing to keep out the voltage spikes generated at the signal frequency by the large current pulses needed to drive the pressure modulator. Another circuit of the same design but without the first stage, was used to supply the piston drive because of the very low output impedance offered ($<0.1\Omega$). This feature is important since unless it is fed from a low impedance source, the piston will not restart should it stop for any reason during a flight. The same $\pm$ 10v. were used by the head amplifier after heavy smoothing and dropping to $\pm$ 8.2v. by the stabilizer. A sufficiently smooth $\pm$ 9v. for the digitizer and the transmitter were provided by the simple zener-diode controlled emitter follower of fig. 8.15.

The d.c. motor driving the multiplex required a 4-volt supply; this was provided by a separate battery enclosed with the motor in a closed copper box. In this way the very persistent spikes generated by the

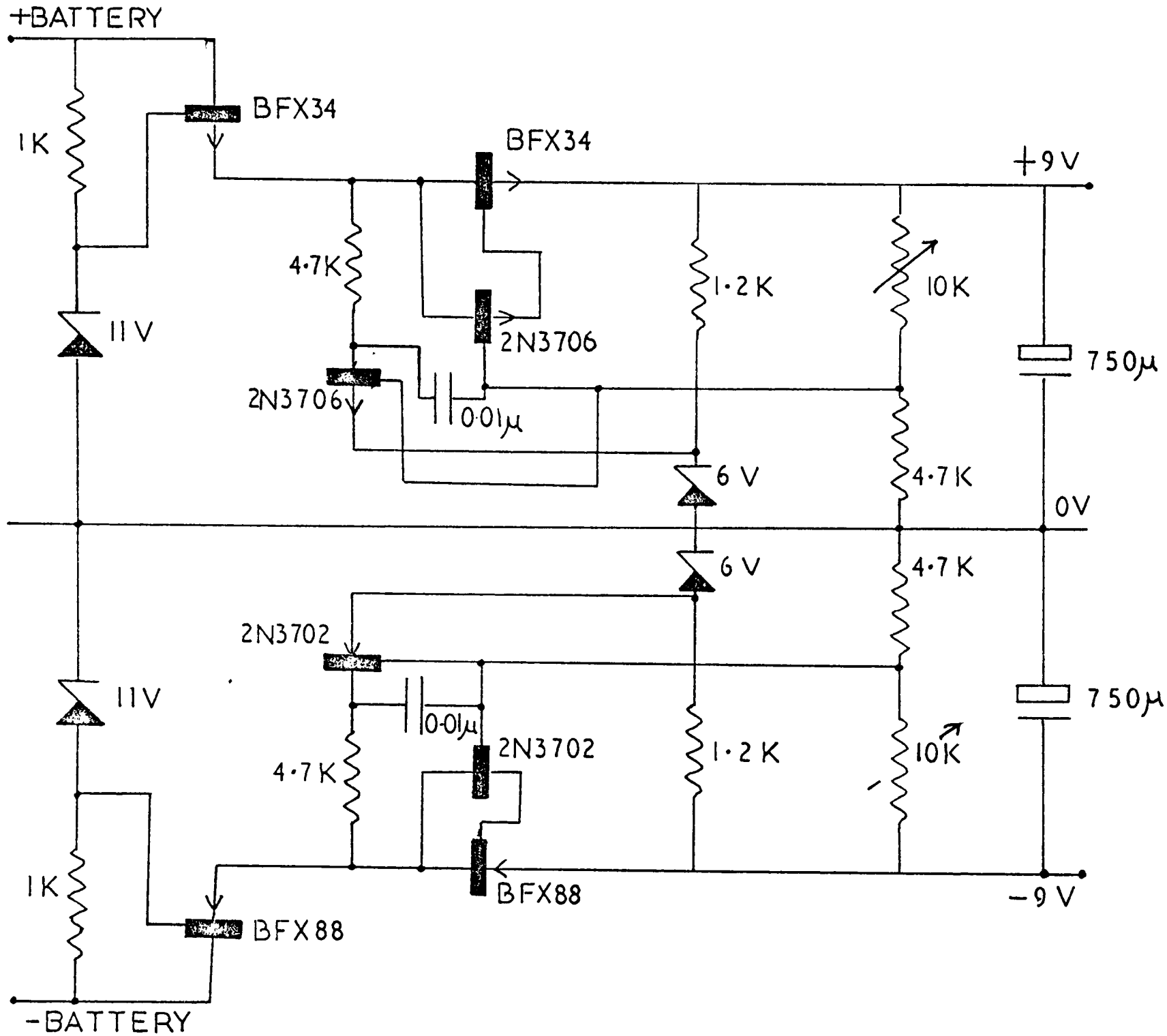


Fig. 8.14. Power Converter Unit supplying signal channel.

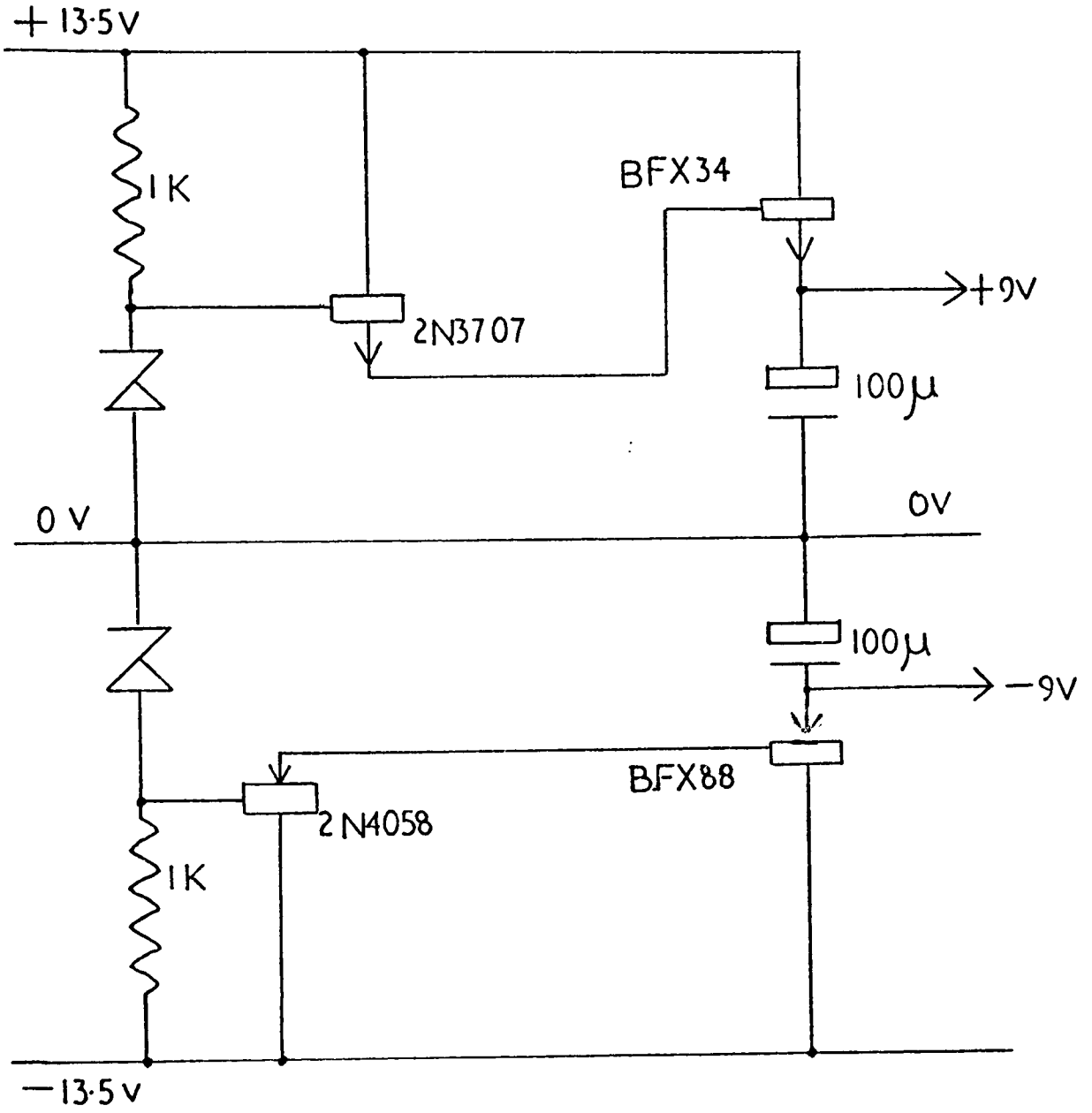


Fig. 8.15. The Secondary Power Converter, used to supply the transmitter and the digitizer.

regulator of the motor were prevented from interfering with the signal electronics.

8.5.4. Multiplexing.

A motor-driven mechanical switch was used to connect the eleven different signal, calibration and housekeeping channels to the telemetry input in turn, so that single channel telemetry could be used. The sequence and timing is shown in table 1. The switch consisted of gold-plated copper contacts forming segments of four concentric circles over which golden wipers are swept by an ESCAP AR601 constant-speed d.c. motor geared down to make one revolution every two minutes. This motor also drives the camshaft which controls the position of the calibration mirror, ensuring convenient and reliable co-ordination between the field of view of the radiometer and the item being transmitted.

8.5.5. Thermistor Bridge.

The various thermistors were switched into the bridge circuit of fig. 8.16 at the appropriate moment by the multiplexer. All thermistors were type M52, which have the characteristic

$$R_T = R_o e^{-B/T} \tag{8.3}$$

where R_T is the resistance at temperature T and R_o and B are typically 0.02 and 3×10^3 respectively, corresponding to R_{300} = about 500 Ω. The output of the bridge can be shown to be

$$i_{out} = V \frac{\begin{vmatrix} R_1 + R_2 & R_3 + R_T \\ R_1 & R_3 \end{vmatrix}}{\begin{vmatrix} (R_1 + R_2)(R_3 + R_T)(R_1 + R_3) \\ (R_1) \quad (R_3) \quad (R_1 + R_3 + R_2) \\ (R_1 + R_2 + R_4)(-R_4)(R_1) \end{vmatrix}} \tag{8.4}$$

The voltage V = 4 volts was provided by Mallory mercury cells; these offer a very stable output under conditions of low load, provided they

Electronic Input	Duration (sec.)	Optical Input
Signal	36	atmosphere
		↓
Electronic zero	3	↑
Spare Connection	5	|
Cell Temperature	5	Warm black body
		↓
Warm Calibration Signal	20	↑
Ambient Temperature	3	|
Battery Voltage	3	Cold black body
		|
Cold Black Body temp.	5	|
Cold Calibration Signal	20	|
Warm Black Body temp. (1)	10	atmosphere
		↓
Warm Black Body temp. (2)	10	
	120	

Table 8.1. Multiplexer sequence and timings.

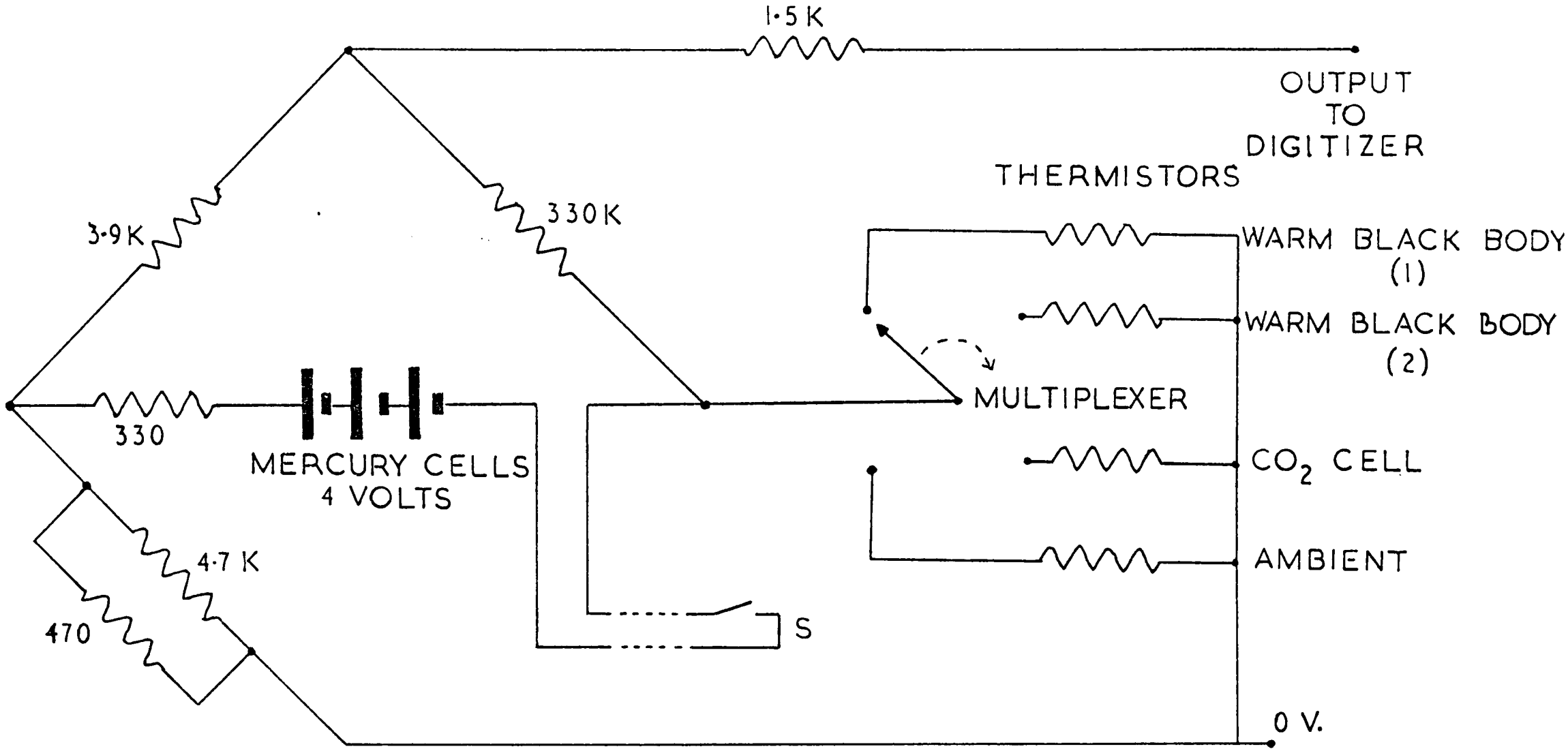


FIG 8.16. The Thermistor Bridge. The switch S was part of the master switch on the outside of the package.

do not get cold. The best values for the resistors R1, R2, R3, R4 and RL were found by substituting for RT in 8.4 using 8.3, and then eliminating R1 and R2 by putting $i_{out} = 0$ when $T = 200^{\circ}K$ and $i_{out} = 300\,\mu A$ when $T = 300^{\circ}K$. This establishes the correct range. A computer program was then written which plotted i_{out} against T for a wide range of practical values for R3, R4 and RL; the one which was most nearly linear was chosen and appears in fig. 8.17. It was then necessary to calibrate the bridge with each thermistor in turn; this can be done by measuring i_{out} at the ice point ($273.2^{\circ}K$) and the sublimation point of CO_2 ($194.7^{\circ}K$), and extrapolating the rest of the curve using 8.4. Each radiometer carried four thermistors; two measuring the temperature of the warm black body, one measuring the temperature of the gas cell, and one on the inside of the package measuring the air temperature.

An encapsulated 3.9 KΩ carbon resistor was fitted into the liquid air reservoir of the cold black body, to give notice when the coolant ran out. It was connected to the telemetry via a single 1.33 volt mercury cell and the multiplexer; this arrangement gives a current of about 300 μA (full scale) when the resistor is cool, and about 15 μA (half scale) when it warms to $300^{\circ}K$.

8.6. Telemetry.

The digitizer, the transmitter (fig. 8.18) and the decoder unit were designed and built by E. J. Williamson. The circuitry is too complicated to be described here, but the important features are as follows. The digitizer is an ideal current measuring device, having zero input impedance and a full scale of 330 μamps. The output is in the form of 8-bit serial binary numbers, produced at a rate of 20/second. The 27 Mc/s frequency-modulated transmitter (fig. 8.18) used a $\lambda/4$ aerial attached to the cord connecting the radiometer to the balloon, and a grounded plane was provided by covering the top of the package with thin copper foil connected to the framework. Such an arrangement is far from ideal, and in the absence of a true infinite ground plane

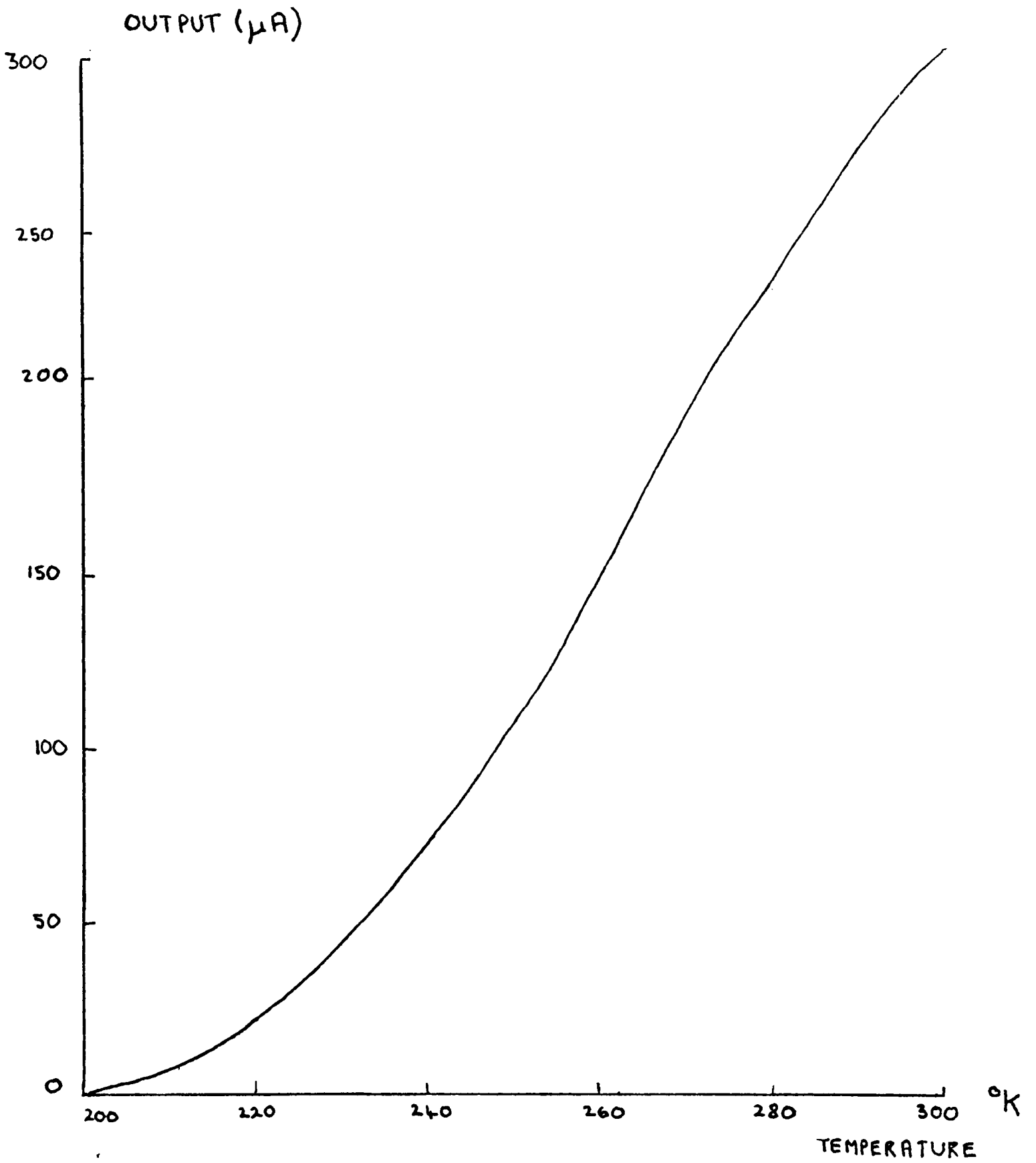


Fig. 8.17. Calibration curve for the thermistor bridge.

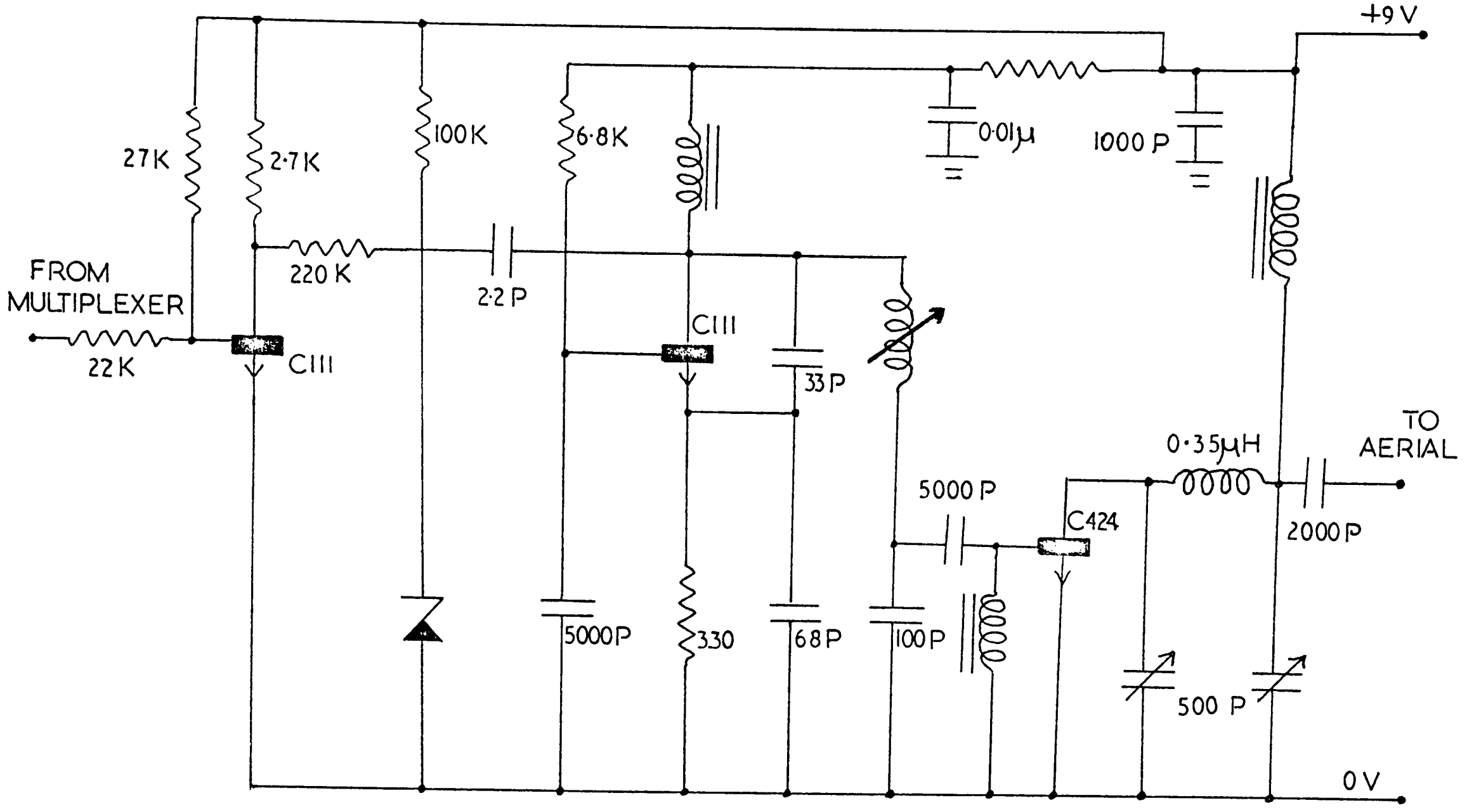


Fig.8.18. The Frequency-Modulated Transmitter, adjustable within the range 26-30 Mc/s.

the aerial behaves as if it has a capacitance C,
equal to the capacity of the radiometer framework in series with it (fig. 8.20). The aerial then no longer appears as an impedance of 37Ω (i.e. half a dipole), and maximum power is no longer transferred to the aerial from the transmitter, unless the capacitance C is cancelled by the appropriate inductance, calculated so that $\frac{1}{\omega C} = \omega L$ at 27 Mc/s. C was measured by suspending the package froma line between two tall buildings and trailing a lead from the framework to a Q-meter, the capacitance of the lead being measured separately and deducted. The appropriate inductance (1.5μH) which cancels the reactance of the measured C (20 pF) at 27 Mc/s could then be included in series with the aerial. An adjustable choke was used, so that fine adjustments were possible. These were made by placing the package on the line again, and tuning the choke for maximum signal in a tuned diode detector (fig. 8.20) on the ground below. There was also the means provided for tuning the transmitter for maximum output into the resistive load. This was set by replacing the aerial with a miniature bulb of the same resistance (37Ω) and tuning for maximum brightness.

The ground installation consisted of a $\frac{\lambda}{4}$ dural aerial with a ground plane, raised 10 metres above the ground; a receiver with automatic frequency control which locked on to the carrier frequency and coped with effects caused by the swinging of the balloon, and a decoding unit which sampled the signal once a second and provided outputs to a visual display in octal units, a chart recorder, and a paper tape punch. The unprocessed signal was also recorded on magnetic tape as a precaution.

8.7. Environmental tests.

Those with experience of test-flying new and previously untried apparatus testify to the fact that satisfactory performance on the laboratory bench is no guarantee of a successful flight. In order to maximise the probability of gratification in this respect, a number of environmental tests were undertaken so that the performance of the apparatus could be studied under simulated flight conditions.

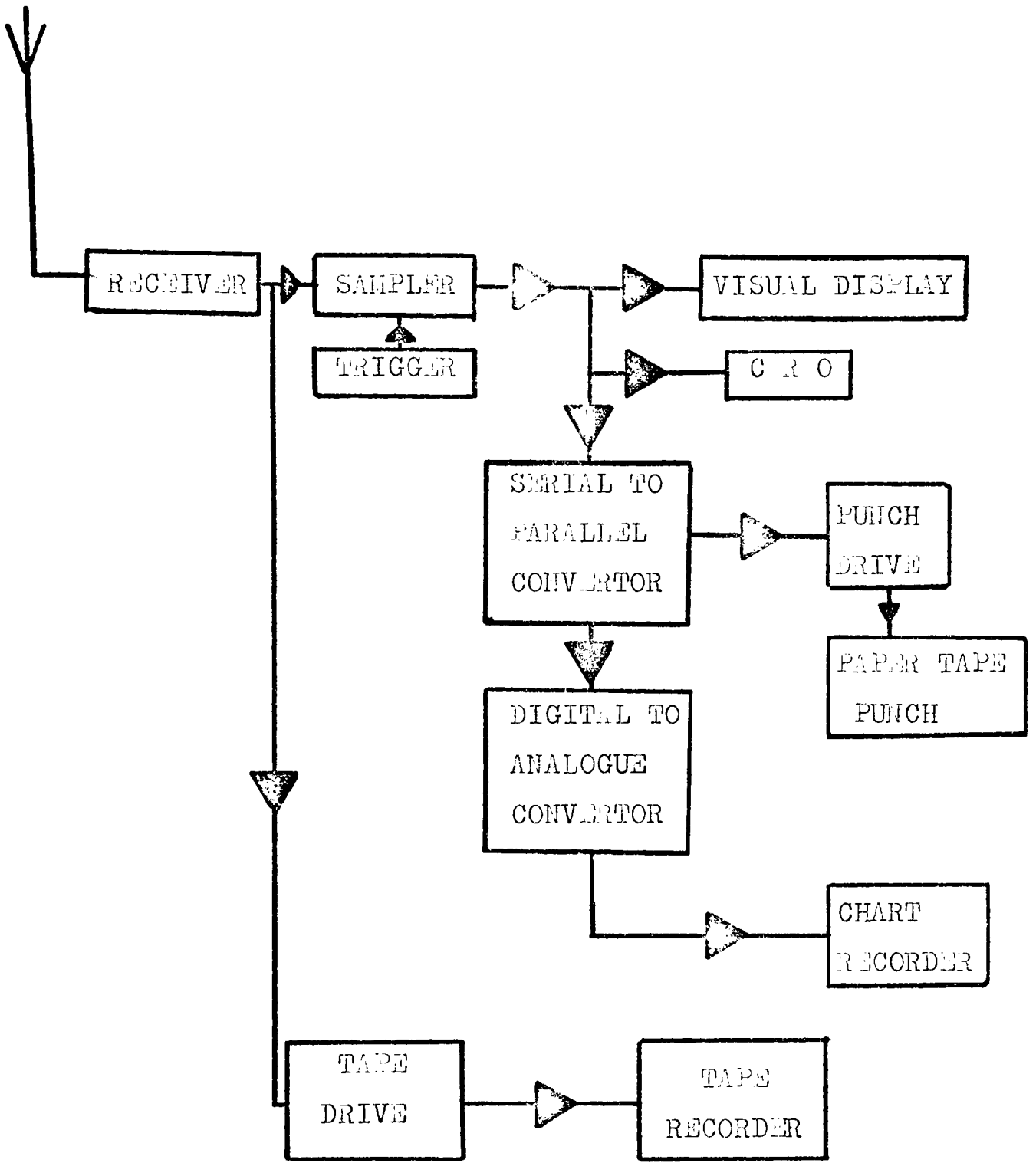


Fig. 8.19. The Ground Installation.

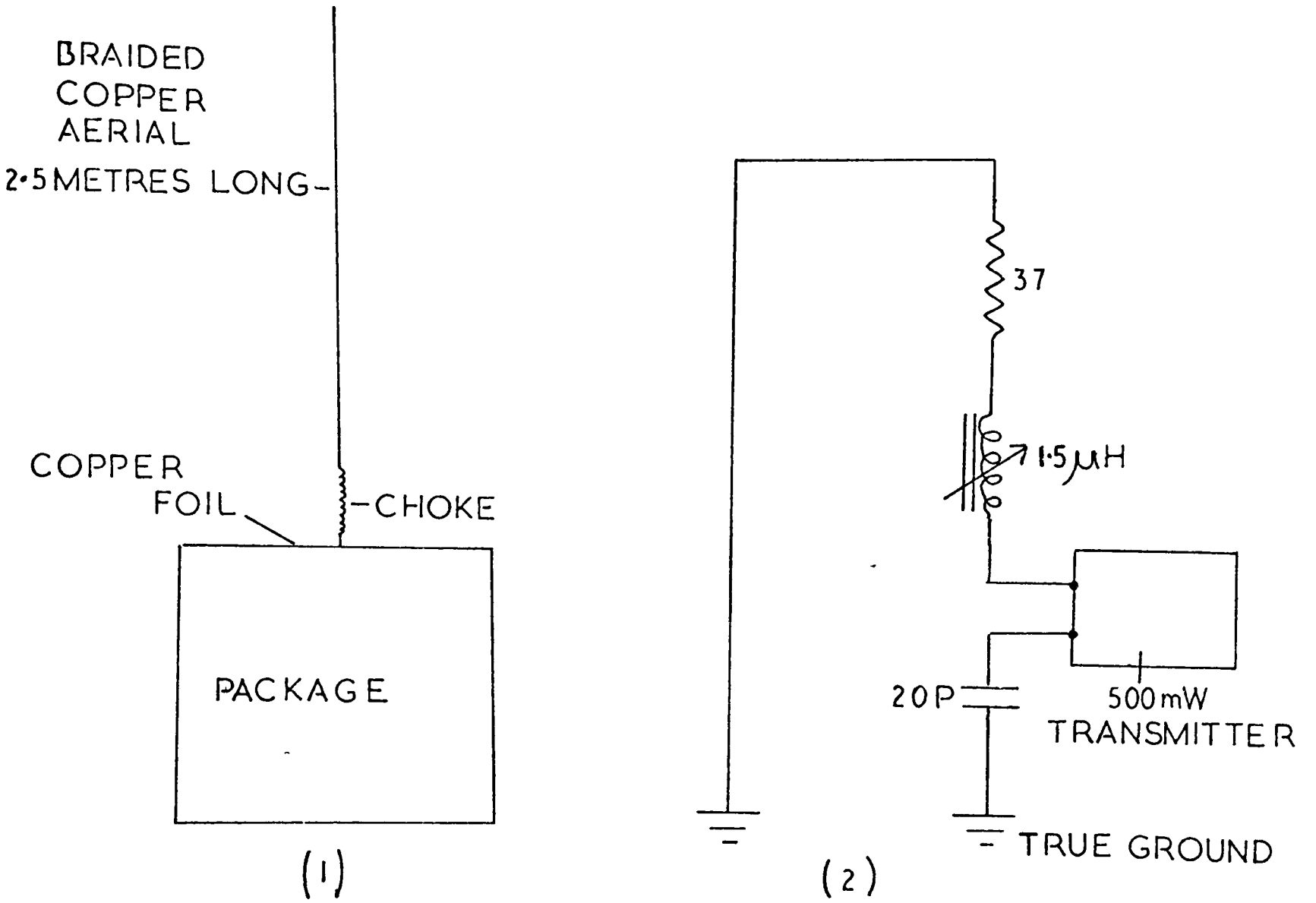


Fig. 8.20. Aerial Tuning. (1) The experimental configuration (2) The equivalent circuit (3) The tuned diode detector.

(i) Vibration. Before the pressure modulator could be proposed for use in a satellite, it had to be demonstrated that it could survive the rigours of launching into orbit. For this the facilities of A.W.R.E. Aldermaston were used to put the modulator through the spectrum of vibrational tests laid down in the Nimbus Handbook for Experimenters (1966).

(ii) Temperature and Pressure. The thermal vacuum tank at the Meterological Office was used to cool the whole apparatus to -40°C following a typical atmospheric profile, and the pressure was reduced at the same time. Both were reduced in steps which corresponded roughly to the variations to be experienced during a flight, and the whole test lasted 90 minutes. The first run was terminated early after the mercury cells which were used to supply the d.c. motor failed at about -10°C. They were replaced by silver-zinc accumulators and no further trouble was experienced. The second test was completely successful.

(iii) Other factors. As a test for the telemetry, and for overall reliability, the complete apparatus was hoisted to various heights up to 2000 ft. by a large tethered balloon operated by the Ministry of Defence. I am grateful to Dr. Reddings and Ken Sillett of the Meteorological Research Unit at Cardington for the use of this facility. More than twelve flights were made in this way, some in fairly high winds (25 knots). High winds tended to spin the package rapidly, and it was found that the piston stopped, presumably due to the centrifugal action, at spin rates over an estimated 10 r.p.s. Such high rates of spin are not normally found in packages on free-flying balloons, and it was not thought necessary to introduce any modifications. In other respects the apparatus eventually functioned well, with a dynamic range of about 150 telemetry bits for a noise level of 1 bit, corresponding to a resolution of better than 1°C ($\pm \frac{1}{2}$°C).

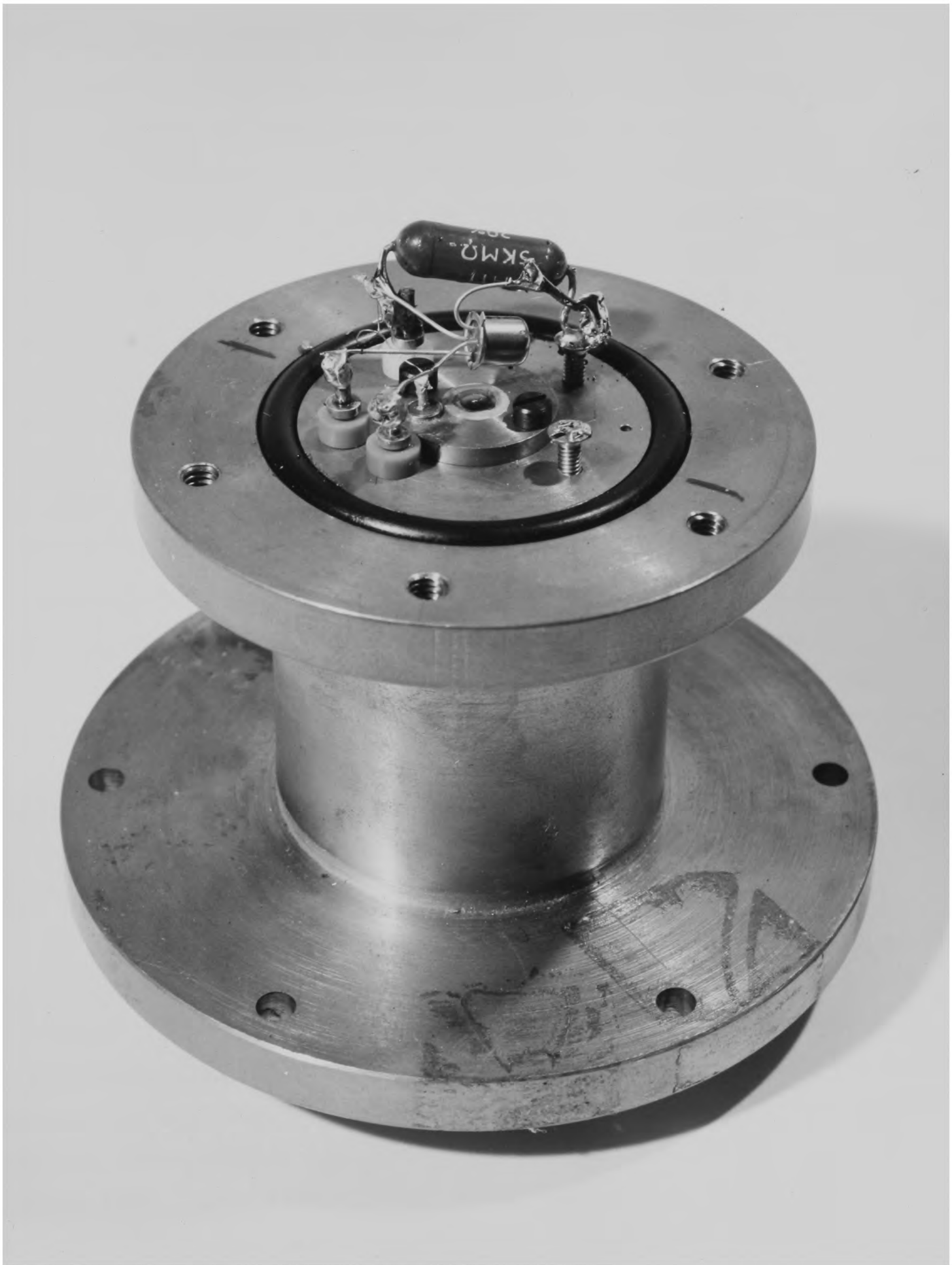


Plate 8. TGS Pyroelectric Detector and Preamplifier.

Chapter 9. The pyroelectric detector.

Certain so-called ferroelectric crystals, having no centre of symmetry, exhibit a spontaneous electric polarization which is strongly temperature dependent. Cooper (1962) showed theoretically than an infra-red detector of very high responsivity could operate on this principle (the pyroelectric effect), having the advantages of requiring neither bias nor cooling and featuring a very low noise level since both Johnson and $\frac{1}{f}$ noise are absent. Research carried out by the Barnes Engineering Co. in the U.S.A. and at the Royal Radar Establishment at Malvern indicated that a detectivity of at least five times that of the thermistor bolometer would be available (Putley, 1968). For the PMSCR, this means that the highest sounding altitude could be raised even higher and the bulky and complicated bolometer bias circuits discarded.

Mullard Ltd. of Southampton agreed to supply a small number of their first experimental pyroelectric detectors for testing and evaluation in the prototype PMSCR. The pyroelectric element was a flake of TGS (triglycine sulphate, $(NH_2CH_2COOH)_3.H_2SO_4$) which was mounted directly on the end of the light-pipe with adhesive (fig. 9.1). The chamber containing the flake was evacuated, as TGS is hygroscopic, and also contained the detector pre-amplifier. The main amplifier, designed by G. D. Peskett, is shown in fig. 9.2.

The earliest tests with the new detector showed powerful mechanical pick-up, even though the flake had been mounted firmly and parallel to the motion of the piston to prevent this. The pick-up originated in the piezoelectric properties of the TGS crystal, which always accompany pyroelectric activity. The problem was solved by including a rubber gasket $\frac{1}{2}$" thick between the light-pipe housing and the gas cell, and clamping both firmly (fig. 9.1). The measured signal to noise was about three times that obtained from a thermistor bolometer under the same conditions.

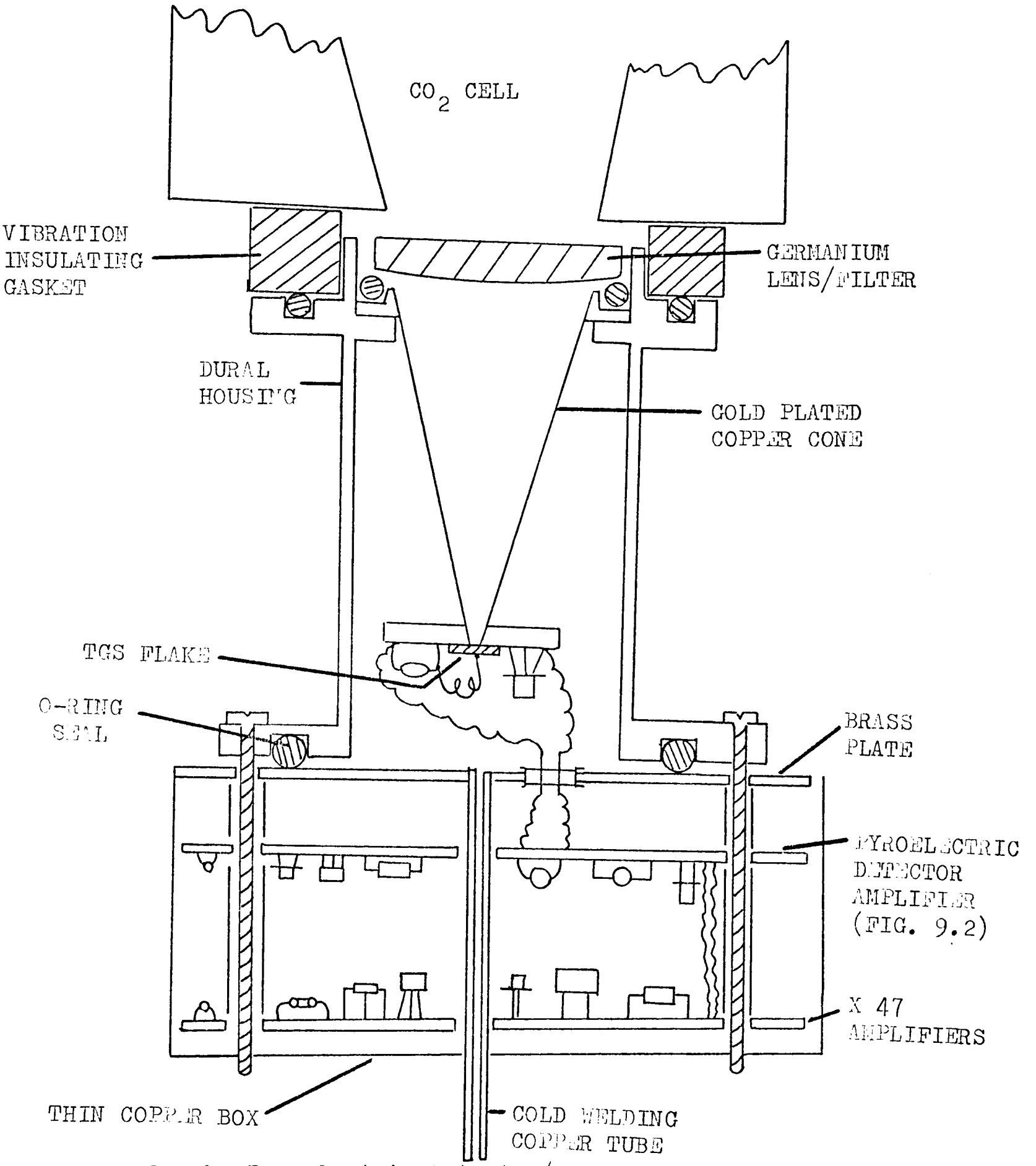


Fig. 9.1. The Pyroelectric Detector/Light pipe Assembly.

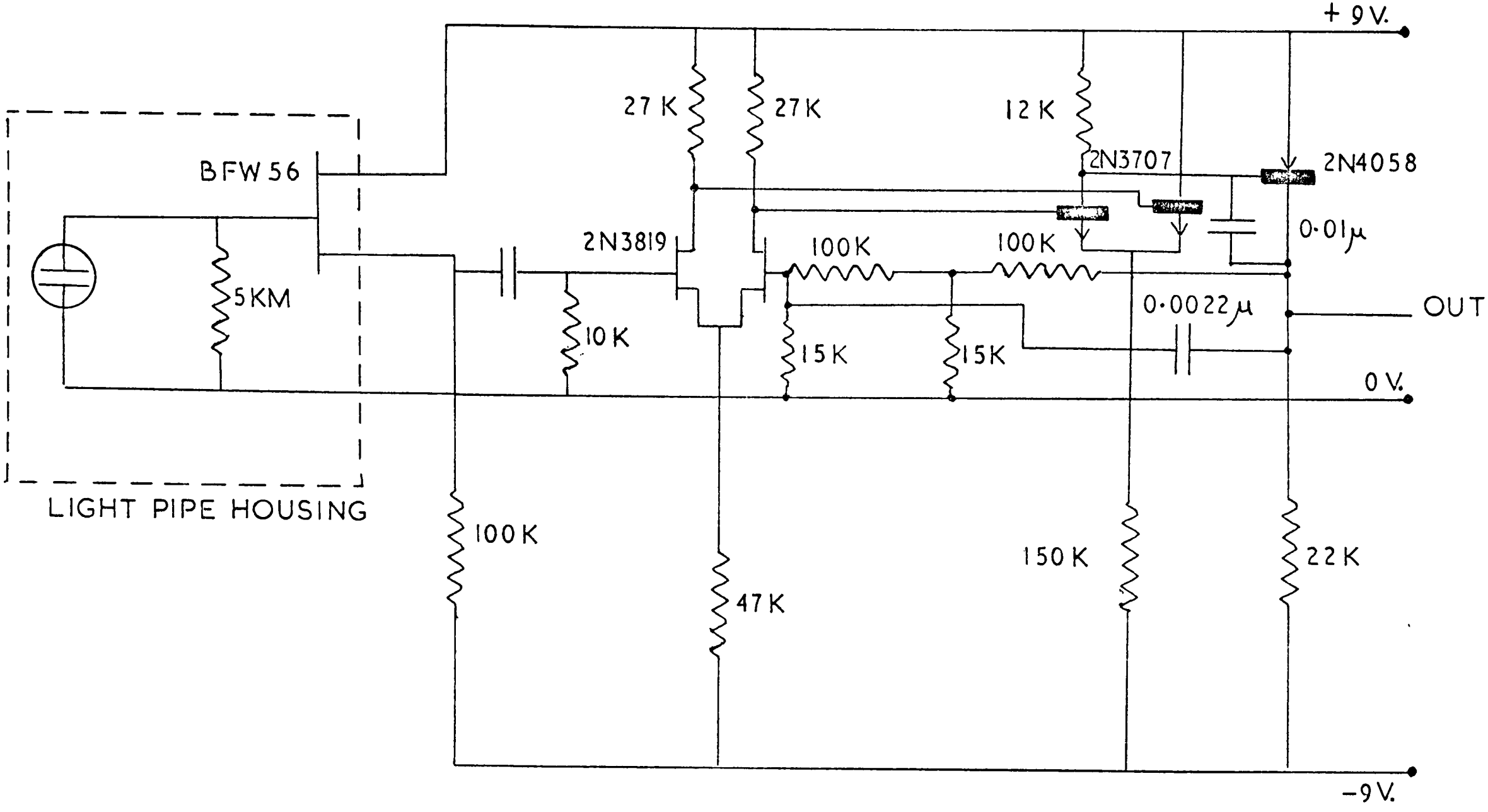


Fig. 9.2. Pyroelectric Detector Electronics. The FET pair 2N 3819 are matched.

Following this successful test, a second balloon radiometer similar to that described in the preceding chapter, which was being constructed as a back-up, was modified to use a TGS pyroelectric detector in place of the bolometer.

Chapter 10. Experimental Weighting Functions.

The theoretically derived weighting functions of chapter 3 are based on a number of approximations and while they are good enough to predict the performance of the instrument, more precise weighting functions are needed if the flight measurements of intensity are to be converted into temperature profiles with a sufficient accuracy. The alternatives are either to use better theory and so reduce or eliminate the approximations, or to use an experimental method to actually measure the weighting functions. The latter is much more attractive because it does not require a detailed knowledge of the line strengths and positions in the band, which is not available anyway, and because the use of the actual instrument in the measurement of the curves enables much more confidence to be attached to the results.

10.1. Method.

The method involves the use of a laboratory path length of CO_2 mixed with nitrogen to simulate the atmospheric path. By using a larger proportion of CO_2 than is found in the atmosphere, it is possible to use a much shorter physical path length l. The conditions for the two path lengths to be equivalent are (1) the absorber amounts must be equal, and (2) the equivalent line widths must be the same (Curtis, 1952; Godson, 1953). These conditions are met if

$$\phi = \frac{p}{2(1+\beta c)} \quad \text{atmospheres} \qquad (10.1)$$

is the pressure in the tank and

$$l = \frac{2a(1+\beta c)}{c} \qquad (10.2)$$

is the constant-pressure path length equivalent to the atmospheric path. Rodgers (1965) has shown that the transmission of the two paths is the same to within 1% provided that the effect of the different temperature structures is taken into account.

The apparatus (fig. 10.1) is a modified version of that devised by Abel (1966). It uses a large vacuum tank containing three mirrors as shown so that the incident radiation from the electrically heated source makes 10 traversals of the tank before entering the balloon radiometer, which is mounted next to the source (but shielded from it by a water-cooled jacket and a screen) just outside the tank. The path length in the tank was measured to be 998 $\pm$ 2 cm., so that from (1) and (2) when filled with 13.75 cm.Hg. of CO_2 and 41.25 cm.Hg. of nitrogen the transmission was the same as that of a ~~horizontal~~ vertical path from the top of the atmosphere to the ground. By reducing the pressure in 150 exponential steps and measuring the transmission each time, a plot of atmospheric transmission (measured from the top down to the level at which the pressure is p) against p is obtained, in which the exponential steps in p correspond to equal height intervals. This curve is differentiated to give the weighting function

The radiometer was calibrated automatically between each measurement of transmission by first inserting a mirror in front of the source, which directed the radiation directly into the radiometer without its passing through the tank, and then by moving a vane in front of the source, cutting off the radiation entirely. These correspond to full scale and zero measurements respectively. The pressure stepping was also accomplished automatically, by periodically connecting a standard volume to the tank via a magnetic valve. A second magnetic valve connected the standard volume to a pump so it could be evacuated between each sharing operation. The pressure in the tsnk was read manually, by mercury and oil manometers. Each radiometer signal, including the calibrations, was sampled eight times, digitized by the flight model telemetry and punched on paper tape. This could then be used as input

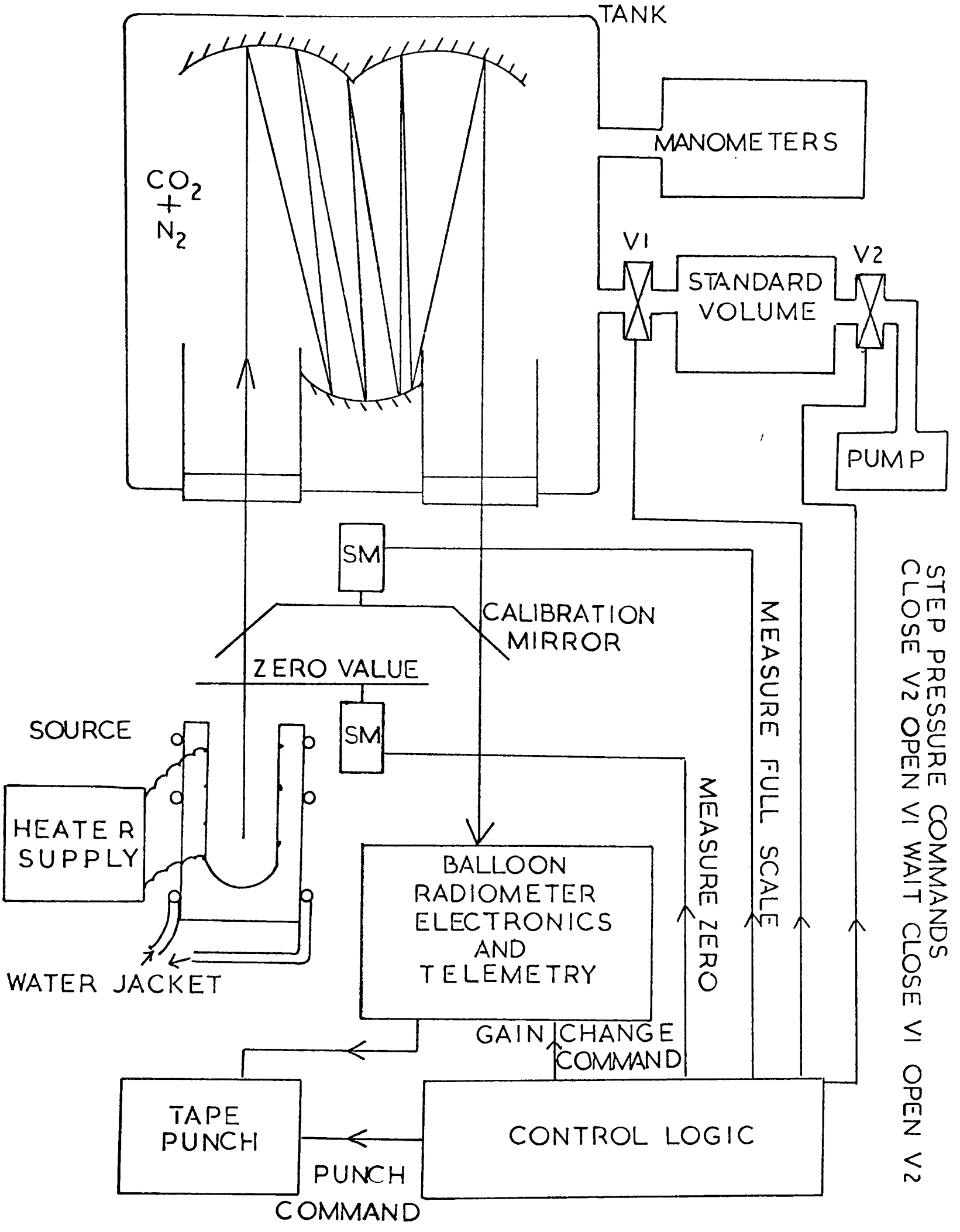


Fig 10.1. Apparatus for measuring weighting functions.

data for a series of library computer programs (Abel 1967, 1968) which fits the data to the best smooth transmission curve, differentiates the result, and plots out the weighting function.

10.2. Results.

The transmission curve for a mean chopping cell pressure of 280 mb. is shown in fig. 10.2, and the corresponding weighting function in fig. 10.3, with the theoretical curve for comparison. They are very similar except at low altitudes, where the measured curve cuts off more rapidly. This effect is due to the overlapping of spectral lines, which is neglected in the theory and which becomes important at high pressures. The actual weighting function is therefore narrower than would be expected from the simple theory, which is advantageous.

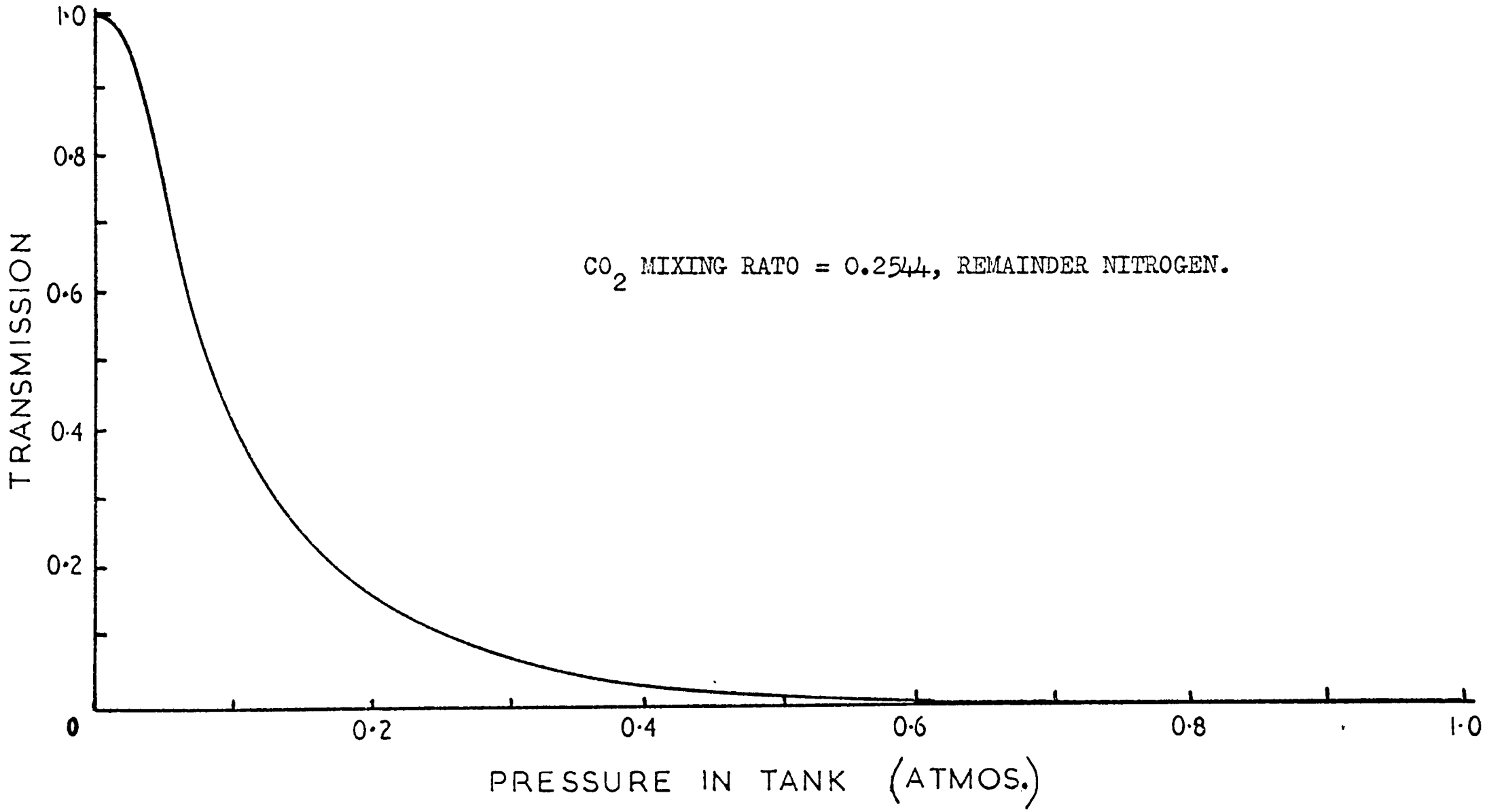
10.3. Effect of Temperature structure.

The use of the Curtis-Godson approximation implicit in 10.1 and 10.2 above is strictly valid only if the temperature structure along the path in the tank is the same as that of the atmospheric path which it represents, because of the influence of temperature on the strength and shape of the spectral lines. If the measured transmission curve is not corrected to allow for this effect, a small but not negligible error in the weighting function results. The method used to apply a correction was as follows:

A transmission curve for the gas in the tank was computed using the strong line approximation, and a fitting function $f(\bar{z})$ determined so that

$$Km\ (\bar{z}) \quad = \quad f(\bar{z}).K_t(\bar{z}) \qquad (10.3)$$

where $K_t(\bar{z})$ is the theoretical weighting function and $Km\ (\bar{z})$ is that actually measured. $f(\bar{z})$ is shown in fig. 10.4. The weighting functions for the case of the real atmosphere were then calculated, using the same model, with the temperature effects taken into account. This was effectively the same procedure as that described in chapter 4,



CO_2 MIXING RATO = 0.2544, REMAINDER NITROGEN.

Fig. 10.2. Transmission of the tank vs. pressure as seen by the PMSCR with p_c = 280 mb.

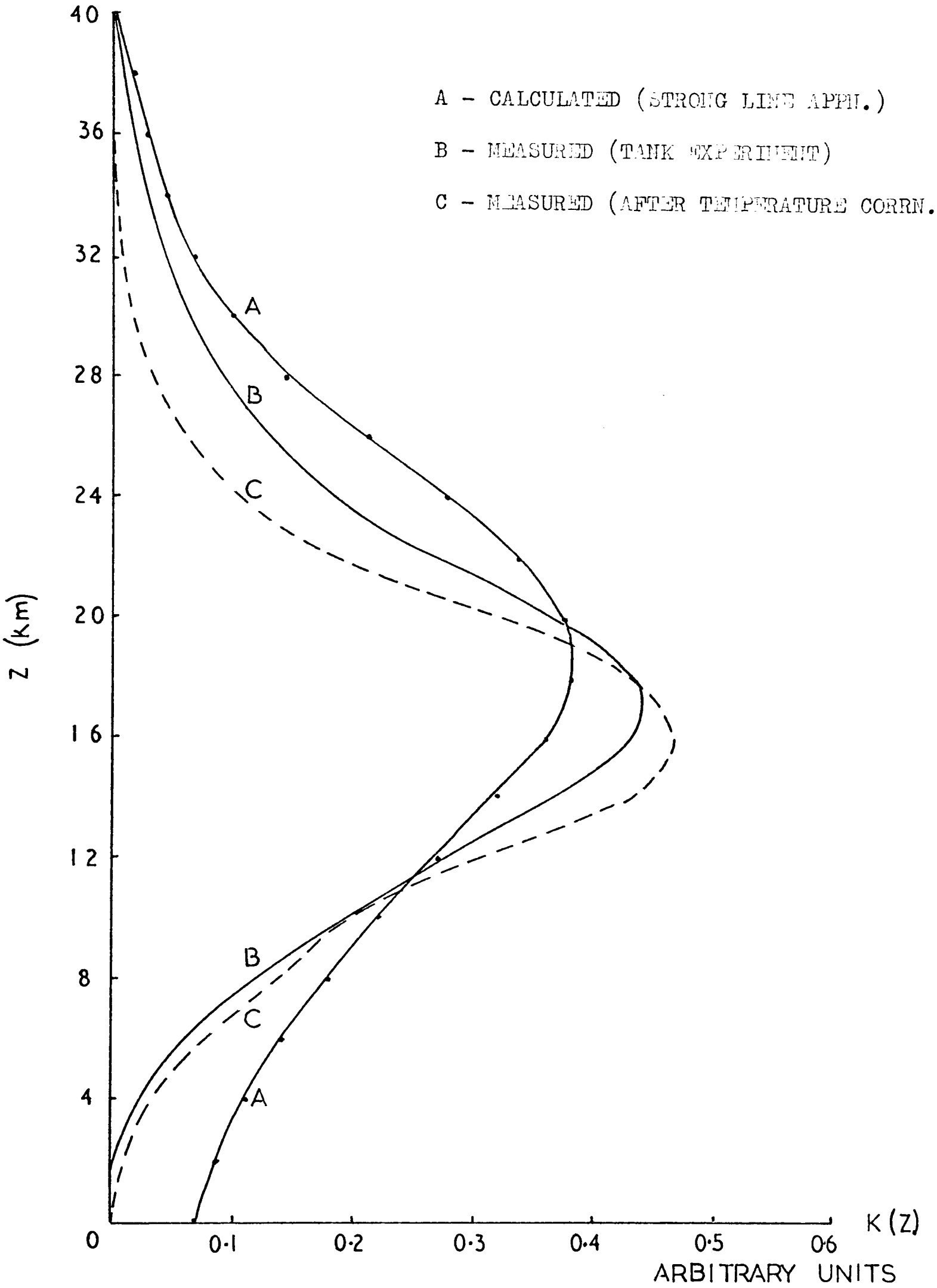


Fig. 10.3. Weighting functions for p_c = 280 mb.

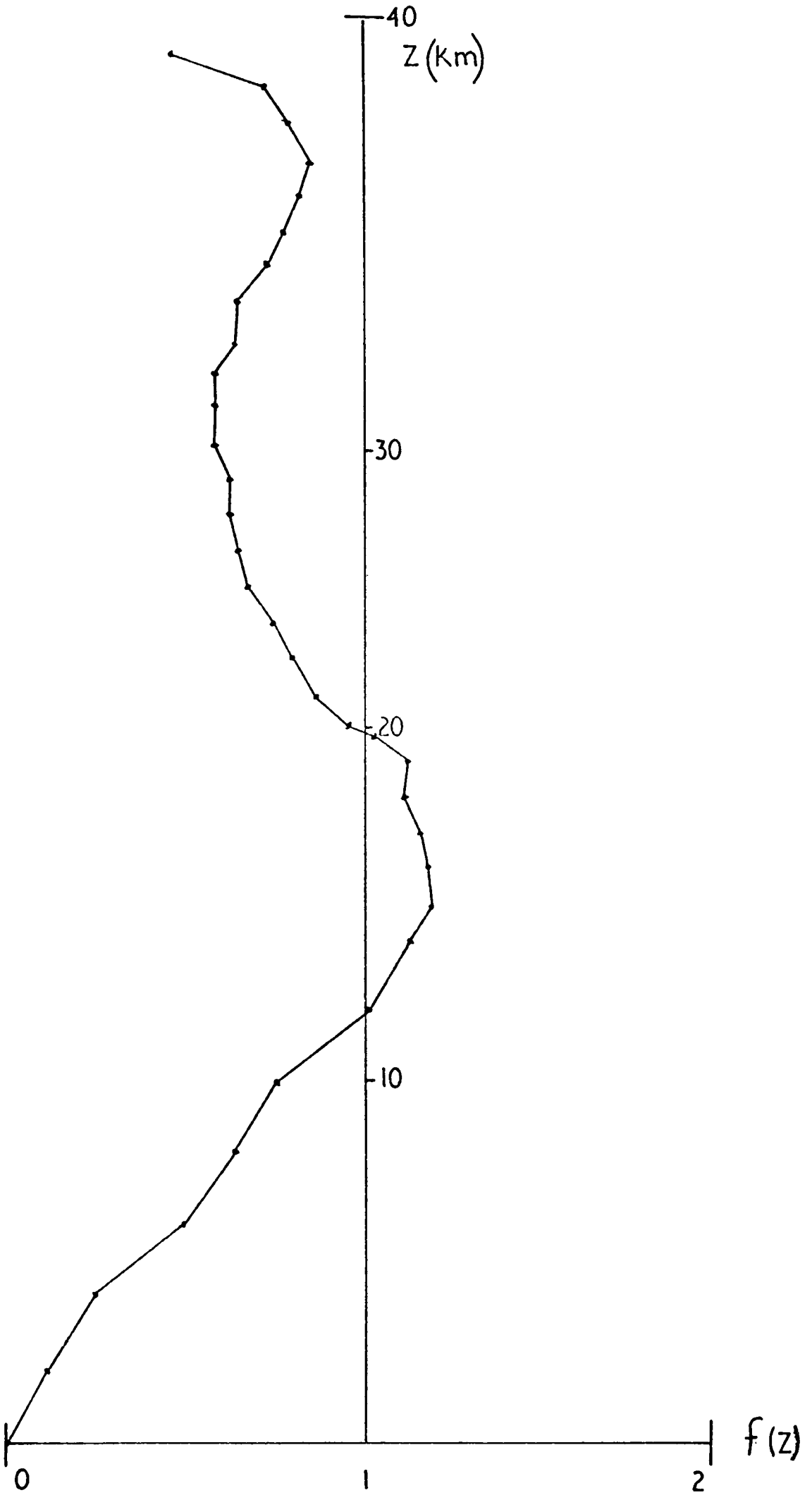


Fig.10.4. The fitting function f(z).

but with S and α replaced by S(T) and $\alpha(T)$ so that both quantities are now functions of height because of the dependence of temperature on height within the atmosphere. The variation of T with z was taken from the U.S. Standard Atmosphere (1962), and data on the temperature dependence of ΣS and $\Sigma(S\alpha)^{1/2}$ was supplied by C. D. Rodgers. This procedure gives a function $K_t(z,T)$ and the final best estimate of the balloon radiometer weighting function is

$$K_m(z,T) = f(z).\ K_t(z,T) \qquad (10.4)$$

This is the weighting function which was used to analyse the flight results. It is shown in fig. 10.3 beside $K_m(z)$ and $K_t(z)$

Chapter 11. Balloon Ascents.

11.1. Introduction.

It was originally planned that the balloon payloads would be launched from Cardington in Bedfordshire, where there is a large disused airfield built for the transatlantic airships which flew before the Second World War. This site offered many advantages: the enormous airship hangars could be used for balloon filling; plentiful supplies of hydrogen and liquid air were available, as was a well-equipped hut for housing the ground station; and the tethered balloon facility could be used for testing. Supplies of two types of balloon were obtained: the Darex 7000 gm., type Jii-42-7000, which had a diameter at burst of 17·4 metres and a ceiling of around 35 km., and the Kaysam 150 GF, the burst diameter of which was 22 metres and the ceiling about 40 km. The latter was a double balloon, with the advantages of compact dimensions at launch and a fast rate of rise. In each case a train consisting of a mesh radar target, a lightweight silk parachute and 100m. of nylon cord was attached between the balloon and the instrument package. Allowing $2\frac{1}{2}$ kgm. of free lift, the total lift on the balloon was about 15 kgm. Of this about 10 kgm. was due to the instrument, including 3 kgm. of thermal insulation and $\frac{1}{2}$ kgm. of liquid air. Launches were

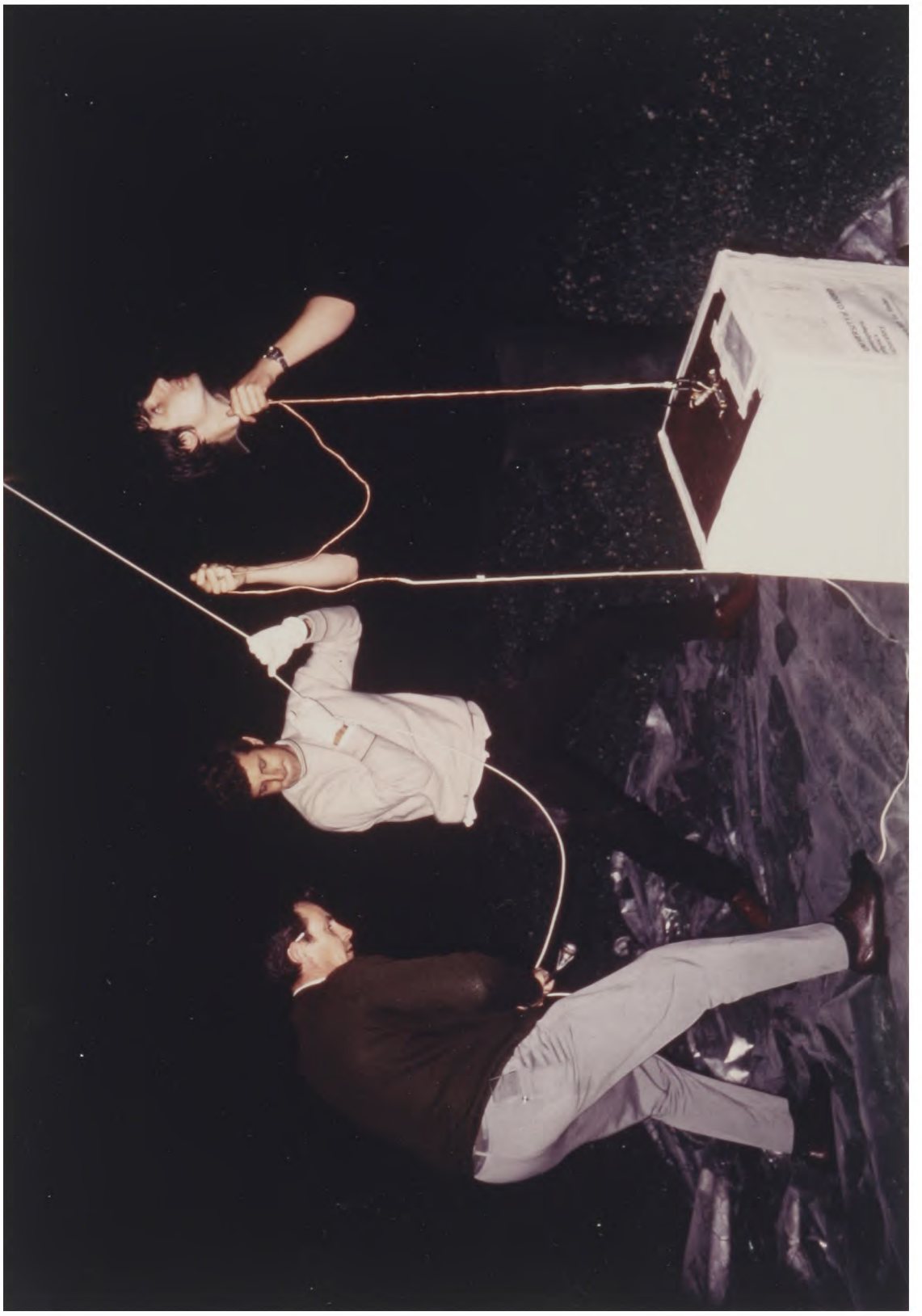


PLATE 9.

not attempted when surface winds of more than 5 knots prevailed. The train could then be released hand-over-hand, and a short run made with the package to prevent it from penduluming into the ground.

After launch, the package was tracked by radar to facilitate recovery, and to provide time vs. height data for the analysis of the results. At Cardington this tracking was made by the unit at the Met. Office station at Hemsby, on the east coast of Norfolk.

A single flight attempt was made at Cardington, using a Kaysam balloon, on 26th June 1970. This was a failure due to a miscalculation of the payload weight, which resulted in the assembly having insufficient free lift. The package was recovered and the balloon freed; it ascended to only 22 km., when it is thought that both the inner and outer balloons may have burst simultaneously.

On about five other occasions the radiometer was prepared for flight at Cardington, only to have the launch cancelled because the prevailing wind changed from that forecast to one which would have caused the balloon to enter the air lanes which lie to the south and west of the airfield. On other occasions the predicted trajectory passed outside the range of the Hemsby radar. After several months of delays of this kind it became clear that days on which a launch could be made without infringing air traffic control regulations and/or losing radar coverage were rare indeed. Consequently the entire operation was transferred in August 1970 to the meteorological station at Larkhill in Wiltshire. From here, both radiometers were flown within a few days of setting up. The flight of the instrument with the pyroelectric detector failed due to a leaking balloon which ascended only briefly and then started to descend, reaching a maximum height of only 1 km. On that occasion no signals were received anyway, because of a fault in the transmitter.

The thermistor radiometer was launched at 4.00 a.m. on 7th August 1970, using a Darex balloon. It ascended in 117 minutes to a height of over 37.8 km., and strong signals were received throughout. Conditions were almost perfect, the air was very clear and the balloon could be

seen with the naked eye right up until it burst more than 20 miles away, at which time it was almost directly above Larkhill. The package descended by parachute and was later recovered from a point about 18 km. to the north-west, near Newbury.

11.2. The Flight of 7th August 1970.

The data received from the thermistors inside the package showed that the thermal insulation was only partially effective, and that the framework cooled to around -30°C during the course of the flight (fig. 11.1). The CO_2 cell also cooled down, but not so rapidly since it had secondary insulation and the heating effect of the action of the piston. Fig. 11.1 also shows an atmospheric temperature profile obtained from a radiosonde flown shortly after the launch of the large balloon, with the specific purpose of obtaining temperatures for use in the interpretation of the radiometer data. Unfortunately the radiosonde balloon burst at only 18 km., and so the profile from 18 to 40 km. is an extrapolation of the radiosonde measurements, made using the U.S. Standard Atmosphere (1962). The surprisingly fast cooling of the interior of the radiosonde package was later attributed to the wind caused by the rapid ascent of the balloon, which must have penetrated cracks in the polystyrene insulation. This factor had not been taken into account during the environmental tests at the Meteorological Office. The cooling of the instrument produced four undesirable effects:

(i) Zero drift. The signals drifted completely off-scale between 4 and 9 km. altitude, but they drifted back thereafter and stayed on-scale for the rest of the flight. It was, however, necessary to contend with a smaller amount of drifting at all levels, and this was the principal source of experimental uncertainty. The drifting is caused by fluctuations in the temperature of the CO_2 in the chopping cell, aggravated by the proximity of the flask of liquid air and drifting vapour in the field of view. This is a problem peculiar to balloon experiments (as opposed to laboratory or satellite experiments) of this type, and is to a large extent unavoidable. Some reduction in experimental accuracy over that obtained in the laboratory or expected in a satellite is inevitable.

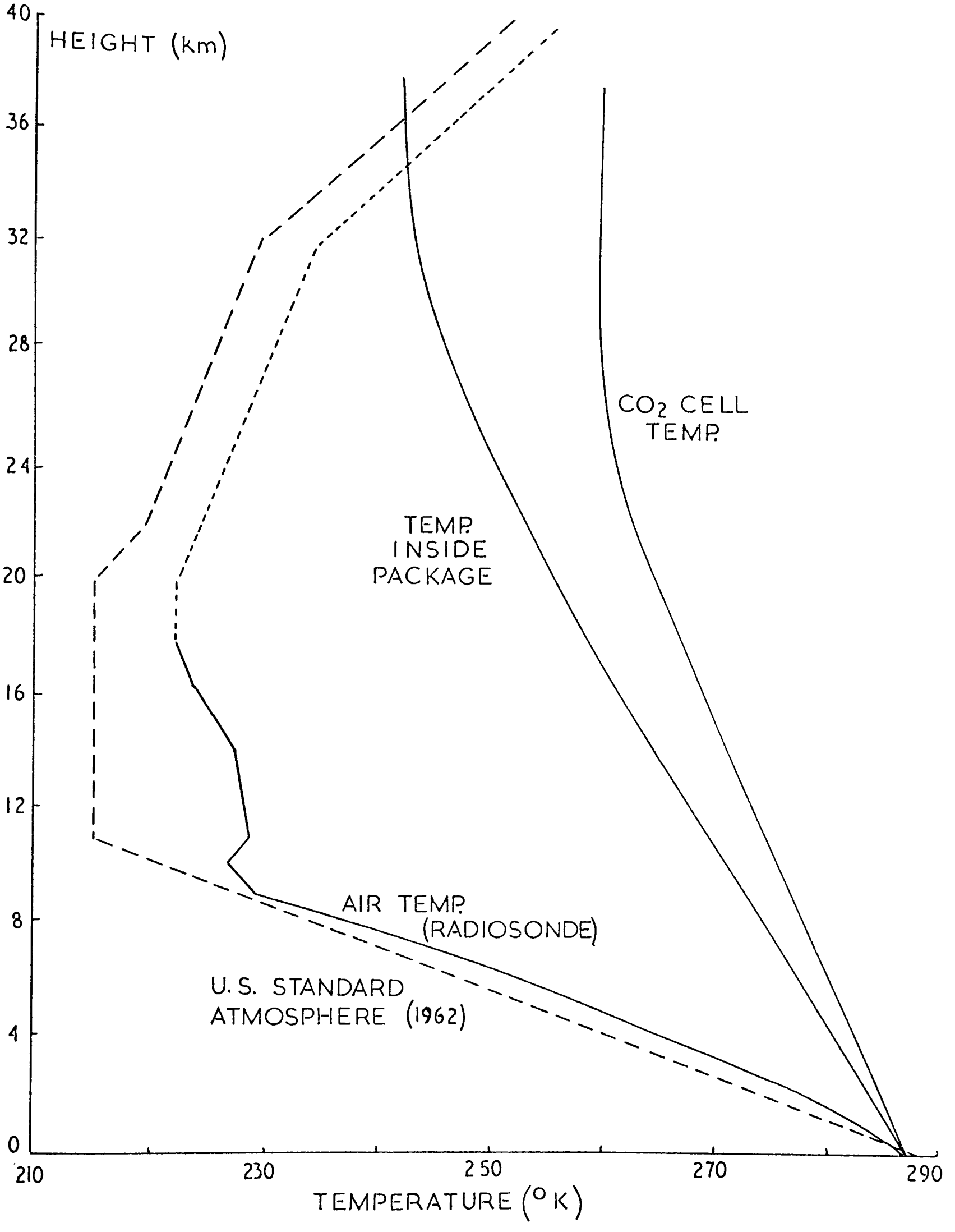


Fig. 11.1. Temperature data for the flight of 7.8.70.

(ii) Gain. The overall gain of the radiometer fell slowly until at maximum altitude it was about 40% of its original value.

(iii) Telemetry noise. About fifteen minutes after launch, spikes appeared on the waveform from the receiver, evidently due to the digitizer power supply having gone noisy. Fortunately the effect was intermittent, and vanished altogether over 20 km. Only a small part of the data was lost.

(iv) Signal Channel noise. When the balloon was at 15 km. altitude, all signals became noisy and erratic, and fell to zero for large parts of each sampling period. This was apparently due to a bad joint in the signal channel circuitry, possibly in the lead to the multiplexer. Above 18 km. the signals returned for short periods, interspersed with severe bursts of noise and periods of zero signal. About three-quarters of the data received between 15 and 38 km. had to be rejected, because in some cases only zero was transmitted and in others there was too much noise; but for eight of the thirty-five or so switch cycles meaningful signals were recovered.

Some increase in the experimental uncertainty in these numbers results from the fact that they were not sampled for the full 36 and 20 second periods allocated, but this is small compared to the increase in uncertainty resulting from the loss of gain and the drifting mentioned above. The effect of the latter was to increase the experimental error from about $\pm$ 2% in the troposphere to around $\pm$ 5% at maximum altitude.

The batteries, which were the components most sensitive to low temperatures (especially the mercury cells biasing the thermistor bridge, which are useless below 0°C) were sealed into thick blocks of polystyrene foam inside the package, and did not deteriorate during the flight.

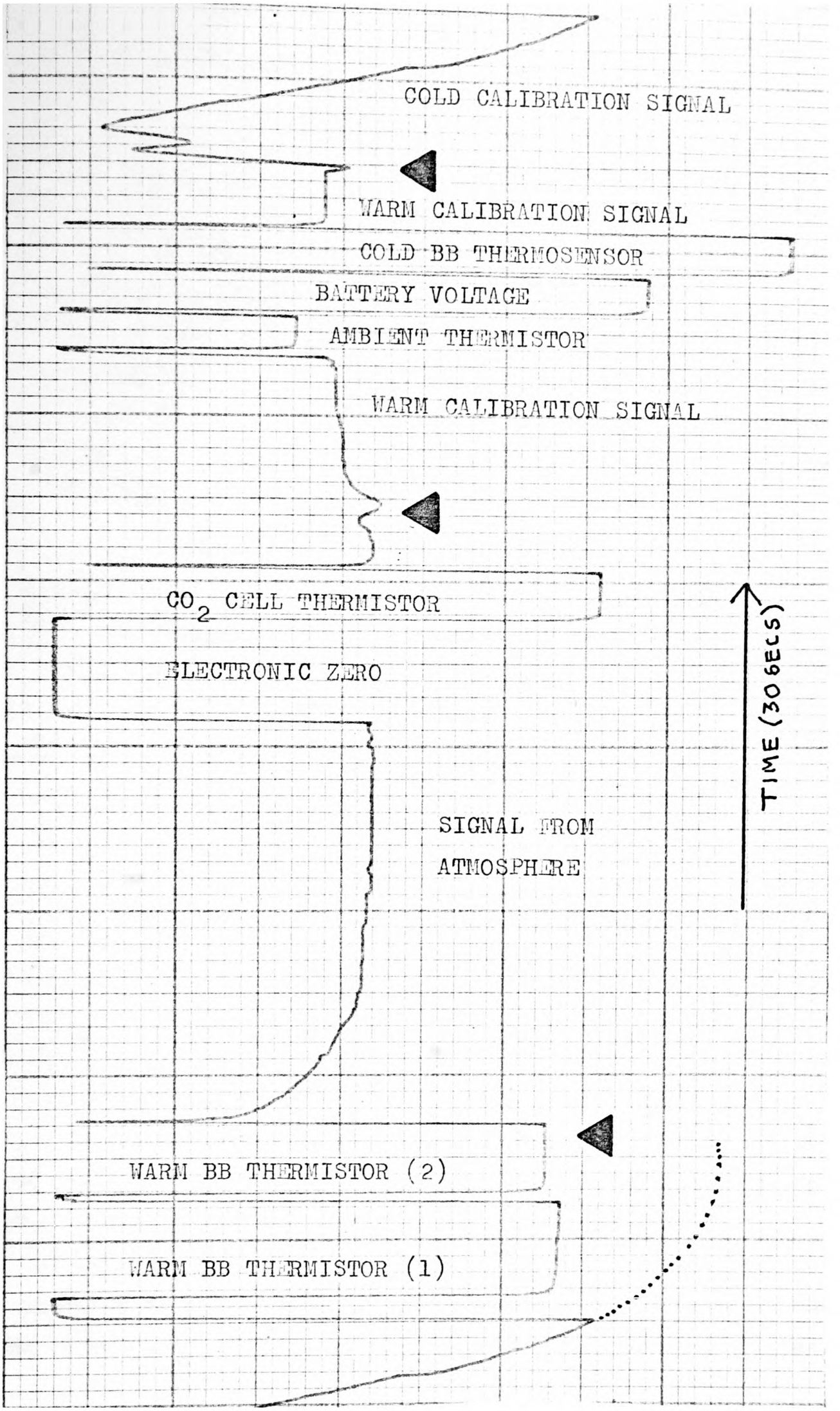


Fig. 11.2. Chart recorder output received when the balloon was 4 km. up. The arrows mark the points at which the mirror stepped.

11.3. Reduction of Flight Data.

It is not possible to obtain a complete temperature profile from a measurement derived from a single weighting function, because a semi-infinite number of profiles would be consistent with a given flux measurement. In other words, a profile with a height resolution of 1 km. measured from the balloon instrument when at $\bar{z}$ = 30 km. represents 30 pieces of information and cannot be recovered from a single measurement, which is only one piece of information. This being so, several approaches remain open.

(i) The flux measurement made when the balloon is at its highest point may be converted to an equivalent temperature. This may then be regarded as the mean temperature of a slab of atmosphere defined by the width of an idealized rectangular weighting function normalized with respect to the true weighting function and centred on its peak. Such a slab turns out to be about 15 km. thick. This is the easiest way to treat the data, but the answer obtained is not very enlightening. It could be useful if the measurement was repeated regularly over a long period of time, to see how the mean temperature varied.

(ii) In the satellite project, profiles would be obtained by using a multi-channel instrument - essentially a number of identical radiometers making measurements simultaneously in the same field of view, but working with different cell pressures and hence different (but overlapping) weighting functions. The number of channels required to produce a profile of given precision is greatly reduced if a statistical approach is employed, using what knowledge there is of the temperatures likely to be found. Rodgers (1965A, 1966) has described such methods in detail. Unrealistic profiles, even though they may be consistent with the flux measurements, are automatically rejected and the solution which is obtained is the most likely profile which could produce the fluxes measured.

(iii) The weighting function seen by the instrument changes as the balloon rises through the atmosphere. Successive measurements therefore

represent separate (but not independent) pieces of information, and there is no reason in theory why a temperature profile may not be derived from them, with a height resolution equal to the distance travelled during one cycle of the multiplexer, or about $\frac{2}{3}$ km. Given the temperature of the ground, that of the 0 - 0.66 km. layer may be determined from the measurement made during the first cycle. This may then be used together with the second cycle measurement to compute the mean temperature of the 0.66 - 1.33 km. layer, and so on.

This method is attractive in principle but unreliable in practice. Because each step depends on the previous ones, errors are accumulated rapidly and the solution tends to oscillate wildly about the true profile. To make it work it would be necessary to introduce a statistical procedure similar to that outlined in the previous section, so that unrealistic solutions do not appear.

(iv) Divergent solutions may be avoided by the simpler approach of using the known temperature profile (from the radiosonde data) to derive the fluxes expected at each level in the atmosphere, and then comparing these with those measured by the instrument. This is the simplest and most reliable approach which is at the same time a rigorous test of the performance.of the instrument, and is the one which was adopted.

The analysis of the flight data was carried out in steps, each step small enough so that the calculations could be handled by the Clarendon Laboratory's small PDP 8/L computer. This has the advantage of very rapid turn-over, because it is operated by the experimenter, who remains on-line to correct programming errors as they occur. It is limited, however, by having a memory of only 8000 12-bit words. The steps are listed below.

(i) The calibration data on the thermistors (ice point and CO_2 point) was used to calculate the constants Ro and b for each (see section 8.5.5.)

(ii) These values were used, together with the thermistor data from the flight, to compute the temperatures of the warm black body (T_w),

the CO_2 cell (T_c) and the air inside the package (T_a) as a function of altitude.

(iii) The temperature of the warm black body (T_w) and the temperature of the atmosphere (T) (radiosonde data) were converted to the corresponding black body functions, using data for the Planck constants from Allen (1965).

(iv) The quantity $\frac{C - S}{C - W} \times B(T_w)$ was computed for each cycle of measurements. S represents the signal measured when the instrument was viewing the atmosphere; C and W represent the signals when viewing the cold and warm black bodies respectively. Taking C as zero flux ($C/W \ll 0.01$) the flux from the atmosphere is given by

$$C - S = G \times \overline{B(T)}$$

where G is the gain, and $\overline{B(T)}$ the flux from the atmosphere, a weighted mean of that from every level below the balloon. The calibration measurements give

$$C - W = G \times B(T_w)$$

so provided the gain remains constant over one two-minute cycle, we have

$$\overline{B(T)} = \frac{C - S}{C - W} \times B(T_w).$$

(v) $\overline{B(T)}$ was also computed from the radiosonde values for $T(z)$ using the temperature-corrected weighting function $K(z)$ measures in the tank experiment. For the balloon at height z_b, it follows from the definition of the weighting function that

$$\overline{B(T)} = \frac{\left[\sum_{z=0}^{z=z_b} K(z).B(T(z))\right]\left(1-\tau(z_b)\right) + B(T_g).\tau(z_b)}{\sum_{0}^{z_t} K(z)}$$

where T_g is the temperature of the ground and $\tau(z_b)$ is the transmission of the atmosphere between the balloon and the ground.

The results are shown in fig. 11.3. The solid curve is the flux $\overline{B(T)}$ as calculated in (v) above; the crosses are the same quantity as measured by the PMSCR. The extent of the arms of each cross is the estimated experimental uncertainty. Excellent agreement is obtained up

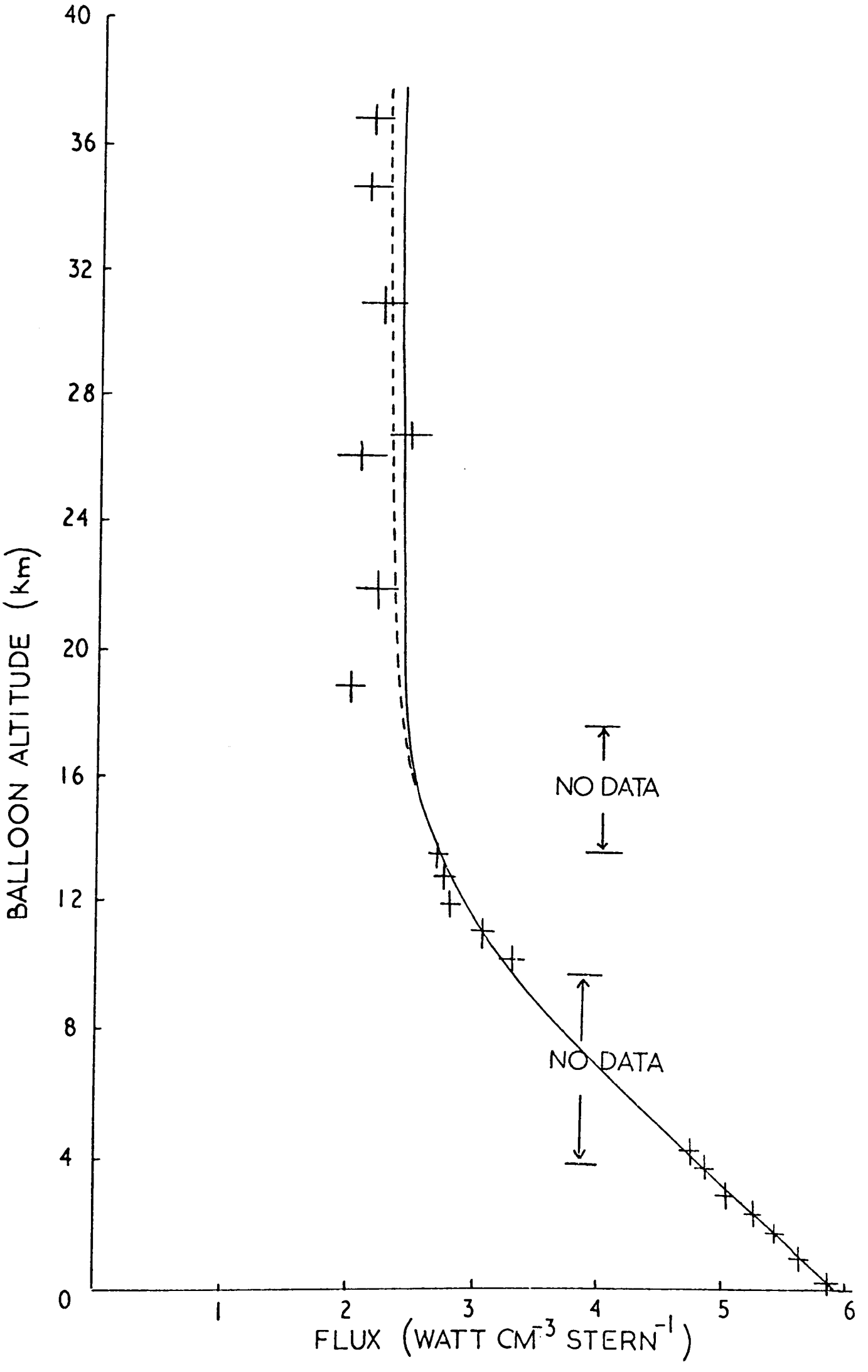


Fig 11.3. Flux measurements made during the flight of 7.8.70.

to about 15 km.; between 18 and 38 km. the results diverge by up to 10%. Three reasons are advanced for this: (i) the loss of gain at higher levels, resulting in a reduced signal-to-noise ratio; (ii) the need to use tabulated data for the air temperature above 18 km., because the radiosonde balloon burst early; (iii) the weighting function used was probably not quite right, because the correction applied for temperature effects was only approximate, and was based on a model atmosphere temperature profile which was actually fairly different from that prevailing (by about $5^{o}K$ above 18 km., fig. 11.1). This has its greatest effect on the weighting function in the region 15-38 km. (fig. 10.3). When the radiosonde temperature profile was used to compute the temperature correction to the weighting function, a slightly different weighting function was obtained, which leads to the dashed curve in fig. 11.2, and rather better agreement overall.

The most important result from the balloon experiment is that the instrument clearly cannot 'see' the ground except when very close to it, in the same way that it could not see the source in the tank experiment except when the amount of gas in the tank was small. Hence the pressure-modulated CO_2 in the radiometer is working properly as a filter passing only radiation at frequencies near the centres of the spectral lines in the band. Even small leaks in this filter would have enabled the radiometer to sense large amounts of flux from the warm ground, and would have produced very different measurements. The effect whereby radiation from very high levels may be selected by a satellite instrument is therefore confirmed.

Chapter 12. Conclusion.

The main conclusions which are drawn from the work described in the preceding chapters are summarized below.

(i) The theoretical performance of a pressure-modulated selective chopper radiometer is such that temperature soundings to a height of around 70 km. are feasible. Up to this height very useful temperature and

spatial resolution are obtainable. Even greater heights may be reached if expected advances in pyroelectric detectors materialise, or perhaps if an oblique angle of view is used.

(ii) The actual performance of a bench prototype verifies the predictions of the theory, where sensitivity is concerned.

(iii) The results of the tank experiment, and of the balloon flight, show that the spectroscopic theory used in the derivation of weighting functions is substantially correct.

(iv) A successful practical instrument can be constructed with realistic standards of size, weight, power consumption, complexity, ruggedness, and cost.

On the basis of these conclusions, a proposal to fly a double-channel PMSCR on the satellite Nimbus F was submitted to the National Aeronautics and Space Administration, and subsequently accepted. Construction of the satellite instrument is expected to begin in early 1971.

12.1, Further Work.

A considerable amount of further work must follow on the computation of satellite weighting functions for mixed line shapes, the correction of laboratory-measured weighting functions for temperature structure, and the analysis by statistical methods of satellite data to reduce them to temperature measurements. All of these require vast amounts of computer time.

For the future, it is very much hoped that a version of the simultaneous $4.3\mu/15\mu$ band PMSCR, described in chapter 6, will be developed for some future satellite to study the interesting problem of radiative relaxation in the upper stratosphere and mesosphere.

References

Alexander, J.A.F., Houghton, J.T., and McKnight, W.B., (1968). J. Phys. B, Series 2, 1, 1, p. 225.

Abel, P.G., (1966). D. Phil. Thesis, University of Oxford.

Abel, P.G., (1967). Clarendon Laboratory Memorandum No. 67.6 (unpublished)

Abel, P.G., (1968). Clarendon Laboratory Memorandum No. 68.3. (unpublished)

Allen, C.W., (1955). "Astrophysical Quantities", London University Press.

B.A.M.S. (1963). Report in Bull. Am. Met. Soc., 44, p. 806.

Barnett, J., (1970). Clarendon Laboratory, Oxford. Unpublished work.

Beyers, N.J., and Meirs, B.T., (1965). J. Atmos. Sci. 22, 3, p. 262.

Bhandari, N., (1970). J. Geophys. Res. 75, 15, p. 2927.

Bischof, W., (1962). Tellus 14, p. 87.

Bossolasco, M., and Elena, A., (1963). Comp. Rend. (Paris) 256, p. 4491.

Burch, D.E., Gryvnak, D., Singleton, E.B., France, W.L., and Williams, D., (1962). Ohio State University Report on contract AF 19(604) - 2633.

Chandrasekhar, S., (1961). "Hydromagnetic and Hydrodynamic Stability", O.U.P.

Conover, W.C., (1961). J. Meteor. 18, p. 410.

Cooper, J., (1962). Rev. Sci. Instr. 33, 1, p. 92.

Craig, R.A., (1965). "The Upper Atmosphere", Academic Press.

Curtis, A.R., and Goody, R.M. (1956). Proc. Roy. Soc. A, 236, p. 193.

Finger, F.G., and Woolf, H.M. (1967). J. Atmos. Sci., 24, 4, p. 387.

Gille, J.C. (1968). Proceeding of Nato Advanced Study Institute "Winds and Turbulence in Stratosphere, Mesosphere, and Ionosphere", North Holland Pub. Co.

Goody, R.M., (1964). Atmospheric Radiation, Vol. I, O.U.P.

Hagemann, F., Gray, J., Machta, L., Turkevitch, A., (1959). Science 130, p. 542.

Haurwitz, B. (1961). J. Geoph. Res. 66, p. 2381.

Hines, C.O., (1960). Canad. Journ. Phys. 38, 8, p. 1441.

Houghton, J.T., (1961). Quart. J. R. Met. Soc. 87, 102.

Houghton, J.T., (1969). Quart. J. R. Met. Soc. 95, 403.

Houghton, J.T., and Smith, S.D., (1966). Nimbus D Proposal (unpublished)

Junge, C.E., (1963). "Air Chemistry and Radioactivity", Academic Press.

James, D.G., (1969). In a paper presented at a Royal Met. Soc. and American Met. Soc. Conference, "The Global Circulation of the Atmosphere", 29th August 1969. Reported in the New Scientist, 43, 666, p. 517.

Kalkstein, M.I., (1962). Science 137, p. 645.

Kalkstein, M.I., (1963). J. Geoph. Res. 68, p. 3835.

Kaplan, L.D., (1959). J. Opt. Sci. Amer. 49, p. 1004.

Kelley, J.J., (1969). J. Geoph. Res. 74, 6, p. 1688.

Knowlton, A.E., (1964). "Standard Handbook for Electrical Engineers", McGraw Hill.

Kondratiev, K..Ya., (1969). "Radiation in the Atmosphere", Academic Press.

List, R.J., Salter, L.P., Telegadas, K., (1966). Tellus 18 (2), p. 345.

Ludlam, F.H., (1957). Tellus 9, p. 341.

McClatchey, R.A., and Shaw, J.H., (1969). J. Atmos. Sci. 26, p. 1350.

Mawdsley, J., (1961). J. Geoph. Res. 66, p. 1298.

Murgatroyd, R.J., and Goody, R.M., (1958). Quart. J. R. Meteor. Soc. 84, p. 225.

Murgatroyd, R.J., and Singleton, F., (1961). Quart. J. R. Meteor. Soc. 87, p. 125.

Nimbus Handbook for Experimenters (1966). National Aeronautics and Space Administration.

Peckham, G., Rodgers, C.D., Houghton, J.T., Smith, S.D., (1966). Clarendon Laboratory, Oxford/J. J. Thompson Physical Laboratory, Reading, Joint Memorandum (unpublished).

Planck, M., (1913). Vorlesungen uber die Theorie der Warmestrahlung. Barth (Leipzig).

Putley, E.H., (1968). Royal Radar Establishment, Malvern. Unpublished memorandum.

Quiroz, T.S., (1969). N.A.S.A. Contractor Report no. CR-1293.

Rawer, K., (1966). Proceedings of the NATO Advanced Study Institute, "Winds and Turbulence in the Stratosphere, Mesosphere, and Ionosphere". North Holland Pub. Co.

Rodgers, C.D., (1965). Clarendon Laboratory Memorandum 65.9 (unpublished).

Rodgers, C.D., (1965)[A]. Clarendon Laboratory Memorandum 66.13 (unpublished).

Rodgers, C.D., (1968). Unpublished work.

Rodgers, C.D., and Williamson, E.J., (1964). Clarendon Laboratory Memorandum 64.9 (unpublished).

Shapley, A.H., (1966). Proceedings of the NATO Advanced Study Institute, "Winds and Turbulence in the Stratosphere, Mesosphere, and Ionosphere". North Holland Pub. Co.

Stroud, W.G., Nordberg, W., Bandeen, W.R., Bartman, F.L., and Titus, R., (1960). J. Geophys. Res. 65, p. 2307.

Tao, L.N., and Donovan, W.F., (1955). Trans. Am. Soc. Mech. Engineers, 77, p. 1291.

Theon, J.S., Nordberg, W., Katchen, L.B., Horvath, J.J., (1967). J. Atmos. Sci. 24, 4, p. 428.

U.S. Standard Atmosphere (1962). National Aeronautics and Space Administration.

Wagner, N.K., (1964). J. Appl. Meteor. 3, 4.

Wark, D.Q., et al., (1966). A series of six papers in the Monthly Weather Review, "Indirect Measurements of Atmospheric Temperature Profiles from Satellites", 94, 6 to 95, 7.

Wark, D.Q., and Fleming, H.E., (1966). Monthly Weather Review 94, 6.

Webb, W.L., (1966). "Structure of the Stratosphere and Mesosphere", Academic Press.

Webb, W.L., (1966a). "Problems of Atmospheric Circulation", Macmillan.

Williamson, D.E., (1952). J. Opt. Soc. Amer. 42, p. 712.